1/48

EVALUATION OF U.S. DEPARTMENT OF ENERGY THERMOHYDROLOGIC DATA AND MODELING STATUS REPORT

Prepared for

U.S. Nuclear Regulatory Commission
Contract NRC–02–97–009

Prepared by

Scott Painter
Chandrika Manepally
Debra L. Hughson

Center for Nuclear Waste Regulatory Analyses
San Antonio, Texas

September 2001

ABSTRACT

Three aspects of the Thermal Effects on Flow Key Technical Issue are covered in this report. The first aspect is a presentation of a new model for in-drift conditions under forced-air ventilation coupled with the mass and energy transport simulator METRA component of MULTIFLO (Lichtner, et al., 2000). This model is used to simulate temperature and relative humidity conditions at the waste package during preclosure operations of the proposed repository for nuclear waste at Yucca Mountain, Nevada. The second aspect is a thermohydrologic model of in-drift and near-field conditions for a postclosure time period of 10,000 years. The postclosure model is also implemented in METRA and utilizes heat reduction factors calculated with the ventilation model to account for heat removed during the preclosure period. Both preclosure and postclosure models were run for high-temperature operating mode and low-temperature operating mode proposed repository designs. The third aspect documented in this report consists of preliminary model simulations of the Cross Drift Thermal Test. The Cross Drift Thermal Test will be the first thermal test at Yucca Mountain conducted in the lower lithophysal unit of the Topopah Spring Tuff, the host rock for most of the proposed repository. Motivations for each of these three modeling studies, including relevant agreements from the U.S. Department of Energy and U.S. Nuclear Regulatory Commission Technical Exchange on Thermal Effects on Flow held in Pleasanton, California, on January 8–9, 2001, are presented. Important results from these modeling studies are summarized at the end of each chapter and in the conclusion.

Reference:

Lichtner, P.C., M.S. Seth, and S. Painter. "MULTIFLO User's Manual." MULTIFLO, Version 1.2. Two-Phase Nonisothermal Coupled Thermal-Hydrologic-Chemical Flow Simulator. Revision 2. Change 1. San Antonio, Texas: CNWRA. 2000.

3/48

CONTENTS

CONTENTS (continued)

FIGURES

Chapter 2

Chapter 3

FIGURES (continued)

Chapter 4

5/48

TABLES

ACKNOWLEDGMENTS

This report was prepared to document work performed by the Center for Nuclear Waste Regulatory Analyses (CNWRA) for the U.S. Nuclear Regulatory Commission (NRC) under Contract No. NRC–02–97–009. The activities reported here were performed on behalf of the NRC Office of Nuclear Material Safety and Safeguards, Division of Waste Management. The report is an independent product of the CNWRA and does not necessarily reflect the views or regulatory position of the NRC.

The authors wish to thank R. Fedors for a thorough technical review and useful insights, A. Woods and C. Cudd for editorial expertise, B. Sagar for programmatic review, and L. Selvey and C. Weaver for format review. The administrative and format support provided by P. Houston is also appreciated. Boundary conditions for the repository-scale model were derived by R. Fedors, whose assistance is greatly appreciated.

QUALITY OF DATA AND CODE DEVELOPMENT

DATA: Original CNWRA data contained in this report were generated in accordance with Quality Assurance Procedures. Data used to support conclusions in this report taken from documents published by U.S. Department of Energy (DOE) contractors and supporting organizations were also generated under the quality assurance program developed by the DOE for the Yucca Mountain Project.

CODE: Modeling of thermohydrological processes was performed using CNWRA-developed MULTIFLO code, Versions 1.2 and 1.5, and performance assessments were conducted using the TPA code Version 4.0. These codes and other routines developed for these analyses were developed following the procedures described in the CNWRA Technical Operating Procedure, TOP–018, which implements the guidance contained in the CNWRA Quality Assurance Manual. The ventilation module is specific to the grid geometry used, and is not currently under TOP-018 control. This module is documented in Scientific Notebook 282E.

1 INTRODUCTION

Technical concerns related to the Thermal Effects on Flow Key Technical Issue were discussed at the U.S. Department of Energy (DOE) and U.S. Nuclear Regulatory Commission (NRC) Technical Exchange on Thermal Effects on Flow held in Pleasanton, California, on January 8–9, 2001. Agreements were made at this technical exchange that will provide sufficient information to make an evaluation of a license application once the commitments stated in the agreements are fulfilled. Modeling studies are presented in this report to provide technical bases for reviewing material presented by DOE in accordance with a subset of the technical exchange agreements. Specifically, a new model for in-drift conditions under forced-air ventilation was developed and is presented in Chapter 2. Mathematical details of the ventilation model are given in Appendix A. An important result of the ventilation model of repository preclosure conditions is removal of 77 percent of heat generated by radioactive decay at the inlet of an emplacement drift, and 89-percent heat removal at the outlet, for a ventilation flow rate of 15 m^3/s [529.67 cfs] for 50 years. The ventilation model also shows a temperature differential of approximately 20 °C [68 °F] developing between the inlet and outlet ends of a drift.

Development of a repository-scale thermohydrologic model for postclosure conditions is presented in Chapter 3. This model uses heat reduction factors derived from the preclosure ventilation model and simulates postclosure conditions over a time period of 10,000 years. Sensitivity analyses are presented showing the effect of assumptions about net infiltration, line-averaged thermal loading, and repository host rock on in-drift and near-field temperature and relative humidity. In-drift conditions are also compared for the alternative high-temperature operating mode and low-temperature operating mode repository designs. Temperature and relative humidity at the waste package for both the high-temperature operating mode and low-temperature operating mode designs for repository preclosure and postclosure are given in Appendix B for use in other in-drift models.

Preliminary simulations of the Cross Drift Thermal Test are presented in Chapter 4 using homogeneous model properties and two realizations of randomly heterogeneous fracture permeability. Heterogeneous fracture permeability was included in these simulations to examine its effects on collection of condensate drainage in boreholes intended for this purpose. A significant result of this modeling study was that condensate drainage could not break the capillary barrier formed by the water collection boreholes, even for heterogeneous fracture permeability with a log-transformed variance of 1.0. Condensation did collect, however, in the water collection boreholes during these simulations. Gas convection cells developed with heating of the test block and air saturated with water vapor entered the collection boreholes where some of the vapor condensed. Under actual test conditions, it would be difficult to distinguish between seepage into water collection boreholes and the formation of condensation inside the boreholes. The formation of condensation inside boreholes could result in misleadingly diluted water samples collected for chemical analyses.

Figures are included at the end of each chapter.

2 MODELING THERMAL RADIATION AND FORCED VENTILATION IN EMPLACEMENT DRIFTS

2.1 DOE Approach and Relevant Technical Exchange Agreements

A model of ventilation in open drifts developed for the DOE and documented in the ventilation model analysis and model report [Civilian Radioactive Waste Management System Management and Operating Contractor (CRWMS M&O), 2000a] shows approximately 70-percent heat removal by ventilation for air flow rates of between 10 and 15 m^3/s [353 and 529 cfs]. A quarter-scale ventilation test is under way at the Engineered Barrier System Test Facility in North Las Vegas, Nevada (CRWMS M&O, 2000b). Phases 1 and 2 of this ventilation test have been completed, and staff have reviewed the plans for Phase 3[1] in accordance with Agreement TEF.2.06 reached at a DOE and NRC technical exchange.[2] Agreement TEF.2.06 states

> "Provide the detailed test plan for Phase III of the ventilation test, and consider NRC comments, if any. The DOE will provide a detailed test plan for the Phase III ventilation test in March 2001. The NRC comments will be provided no later than two weeks after receipt of the test plan, and will be considered by the DOE prior to test initiation."

Comments on Phase 3 of the ventilation test have been provided,[3] and Agreement TEF.2.06 will be satisfied once NRC comments are considered by the DOE prior to test initiation. The related Agreement TEF.2.07 states

> "Provide the Ventilation Model AMR, Rev 01 and the Pre-Test Predictions for Ventilation Test Calculation, Rev. 00. The DOE will provide the *Ventilation Model* AMR (ANL–EBS–MD–000030) Rev 01 to the NRC in March 2001. Note that ventilation test data will not be incorporated in the AMR until FY02. The DOE will provide Pre-test Predictions for Ventilation Tests (CAL–EBS–MD–000013) Rev 00 to the NRC in February 2001. Test results will be provided in an update to the *Ventilation Model* AMR (ANL–EBS–MD–000030) in FY 02."

The document relevant to Agreement TEF.2.07 (CRWMS M&O, 2001a) has been received, but the ventilation model analysis and model report,[4] which was due in March 2001, has not yet been received. Data from the quarter-scale ventilation test will not be incorporated into

---

[1]Chowdhury, A. "Administrative Item 01402.661.019: Comments on the 'Description of Phase 3 of the Ventilation Test Rev. 1,' TWP–EBS–ME–000009 Revision 03." Letter (July 26) to J. Pohle, Division of Waste Management, NRC. Washington, DC: NRC. 2001.

[2]DOE and NRC. "Technical Exchange and Management Meeting on Thermal Effects on Flow, January 8–9, 2001." Pleasanton, California. 2001.

[3]Chowdhury, A. "Administrative Item 01402.661.019: Comments on the 'Description of Phase 3 of the Ventilation Test Rev. 1,' TWP–EBS–ME–000009 Revision 03." Letter (July 26) to J. Pohle, Division of Waste Management, NRC. Washington, DC: NRC. 2001.

[4]CRWMS M&O. "Ventilation Model." ANL–EBS–MD–000030. Revision 01. Las Vegas, Nevada: CRWMS M&O. To be published (2002).

the ventilation model analysis and model report until fiscal year 2002, according to Agreement TEF.2.07.

CNWRA developed a semi-analytical model of forced ventilation in open emplacement drifts, coupled with the two-phase mass and energy transport METRA simulator component of MULTIFLO Version 1.5, for independent evaluation of the DOE approach. This semi-analytical model will provide the technical basis for staff review of the ventilation model analysis and model report.

2.2 In-Drift Conditions During Preclosure

2.2.1 Model Description for In-Drift Preclosure Conditions

A set of three-dimensional METRA [mass and energy transport component of MULTIFLO (Lichtner, et al., 2000)] simulations was used to investigate ventilation effectiveness and the associated thermodynamic environment in the drift during the preclosure period. Because the mass transfer processes inside an open drift cannot be modeled directly with a porous media flow code like METRA, a model for ventilation effectiveness was developed for this study. Details of the model are given in Appendix A. The model accepts temperature and liquid saturation at the drift wall as input, calculates the fraction of the decay heat that is removed by ventilation air, and returns estimates of heat flux at the drift wall. Physical processes include convective heat transport from the waste package and the drift wall to the ventilation air, drying of the drift wall by the ventilation air, and radiative transfer from the waste package to the drift wall. The thermal radiation may occur along the length of the drift and not just radially outward from the drift center. Radiative transfer may also occur from the waste package to the end of the finite length tunnel although this effect is generally small. The ventilation model was called as a subroutine by METRA at each time step to calculate the fraction of the total power that arrives at the drift wall, thereby achieving a self-consistent calculation that couples the in-drift processes with the thermal hydrological processes in the near-drift region.

The modeled region is a slab oriented with a single emplacement drift. The slab extends vertically from the water table to the land surface. In one horizontal direction, 0 the model region extends the 600-m [1,968.5-ft] distance of one-half of an emplacement drift. Only one-half of the drift was modeled because of symmetry conditions; the modeled ventilation configuration has air entering from the two ends of the 1.2-km [.7456-mi] long drift and exiting through a shaft in the middle. In the other (thin) horizontal direction, the slab extends 40.5 m [132.87 ft] from the center of a drift to the center of the pillar region between drifts.

An unstructured grid was used to minimize the required size of the three-dimensional grid. A 20 × 20-m [65 × 65-ft] detail from a vertical slice is shown in Figure 2-1. The grid was designed to provide sufficient detail near the emplacement drifts where large gradients in temperature and liquid saturation are possible while using computationally efficient coarse grid cells away from the heated regions. Although the upper and lower boundaries were placed at the land surface and water table, the grid for heated runs contained no computational cells above and below the Topopah Spring Group. The effects of these units were accounted for indirectly by giving the cells at the top and bottom of the explicitly modeled region large values for the boundary connection distance. This was a good approximation because the thermal hydrological perturbation associated with the emplacement drifts did not have time to propagate

beyond the Topopah Spring Group during the preclosure period. The full stratigraphic column, however, was used to establish ambient conditions that were used as initial conditions on the heated runs. Each vertical slice comprised 440 computational cells, which resulted in a total of 880 cells when both the fracture and matrix continua were accounted for. The final grid was extruded in 20 slices along the length of the drift for a total of 17,600 cells.

Boundary conditions at the base of the model were fixed temperature {32 °C [89.6 °F]}, liquid saturation (100 percent), and barometric pressure. At the top of the model, the temperature and barometric pressure were fixed, and a constant infiltration rate of 10 mm/yr [0.4 in/yr] was applied. No flow conditions (symmetry) were used on three of the remaining faces. The exception was the end of the drift that corresponded to the repository edge and the inlet for ventilation air. A no-flow boundary condition is not an appropriate assumption here. Instead, a distant boundary approximation was used. Specifically, the boundary was placed 250 m [820 ft] away from the end of the drift, and ambient conditions were imposed on the boundary.

Hydrological and thermal properties of the rock were the same as those used in the models described in Chapter 3 and are tabulated in Appendix C.

2.2.2 Model Results for In-Drift Preclosure Conditions

Two sets of preclosure simulations were performed; one set to represent a high-temperature operating mode and a second set to investigate a low-temperature operating mode. Several simulations were performed to check sensitivity to ventilation flow rates, moisture removal coefficients, and other modeling assumptions. The waste package temperature, relative humidity in the ventilation air, and total heat flux arriving at the drift wall were recorded as a function of time and distance along the drift. The total heat flux was then used to define a time-and-position-dependent heat reduction factor. This reduction factor was used to represent the preclosure period in the postclosure simulation as described in Chapter 3.

2.2.2.1 Model Results for the High-Temperature Operating Mode

A line-averaged heat load of 1.2 kW/m, a preclosure period of 50 years, and a ventilation rate of 15 m^3/s [529 cfs] were used in the simulations for the high-temperature operating mode. Heat transfer coefficients, h_c and h_w, were 1.89 W/(m^2 °C), consistent with standard heat transfer correlations (e.g., Duderstadt and Hamilton, 1976) for fully turbulent conditions. Figure 2-2 shows temperature at 4 years in three vertical slices along the drift (inlet side, middle of the drift, and outlet side) for a reference case with no moisture removal. The temperature at the inlet side was much lower than the outlet side because the ventilation air increased in temperature as it traveled through the drift and was less effective at cooling the downstream end of the drift.

Waste package temperature and relative humidity in the ventilation air, neglecting the effect of moisture removal, are shown in Figure 2-3. At early times, the ventilation air was ineffective (Figure 2-4) at removing heat from the drift because the drift wall was relatively cool, and thermal radiation from the waste package was very effective at transferring heat directly to the wall. As the drift wall heated up, the radiative transfer became less effective, the waste package temperature increased in response, and a greater fraction of the heat was removed by

the flowing air. The waste package temperature peaked around 95 °C [209 °F] at 4 years. The relative humidity reached a minimum of aproximately 6 percent during this time period.

Also shown in Figure 2-4 is the power delivered to the drift wall as modeled by DOE using a constant 70-percent reduction factor in the Multiscale Thermohydrologic Model (CRWMS M&O, 2000c). As compared to this model at ventilation, a 70-percent reduction factor led to an underestimate of the heat load on the wall at early times and an overestimate at later times. The heat reduction factors integrated over the first 50 years were 77 percent at the outlet side of the drift and 89 percent at the inlet side.

Sensitivity to the ventilation flow rate is shown in Figure 2-5, which shows the power delivered to the drift wall for air flow rate of 10 m^3/s [353 cfs] compared with 5 and 15 m^3/s [176 and 529 cfs]. An understanding of the sensitivity to flow rate is useful for evaluating possible future changes to repository design and because of possible variation in flow rates between drifts. For this particular set of simulations, a heat transfer coefficient of 1.5 $W/(m^2\ °C)$ was used for the 10 m^3/s [353 cfs] case. Following standard heat transfer correlations (Duderstadt and Hamilton, 1976) applicable for gasses and light fluids under turbulent conditions, the heat transfer coefficient is scaled by velocity to the 0.8 power, yielding 0.86 $W/(m^2\ K)$ for an air flow rate of 5 m^3/s [176 cfs] and 2.07 $W/(m^2\ K)$ for an air flow rate of 15 m^3/s [529 cfs]. The heat transfer coefficient at flow rates of 15 m^3/s [529 cfs] is slightly larger than that used for Figure 2-2, which provides some insights into sensitivity to this parameter. The kinks in the heat load curves near 6 and 9 years are caused by the limited temporal resolution in the decay heat curve.

In DOE ventilation models and in the simulations supporting Figures 2-3 to 2-5, the effects of moisture removal from the drift wall were neglected. In reality, the ventilation air flowing past the drift wall should act to dry the drift wall, thereby reducing the heat load by evaporative cooling. To evaluate this process, two additional simulations were performed at the 15-m^3/s [529-cfs] reference conditions of Figure 2-3. The moisture removal coefficients for these two simulations were 10^{-4} and 10^{-3} $kg/m^2/s$ [2×10^{-5} and 2×10^{-4} $lb/ft^2/s$]. As can be seen in Figure 2-6, the moisture removal had only a modest effect on the heat load to the wall. Although evaporative cooling was effective at early times, the drift wall quickly dried out and shut off the moisture flux and the associated evaporative cooling. The resulting effect on the integrated heat reduction was very minor {77 percent for no moisture removal versus 79 percent for 10^{-3} $kg/m^2/s$ [2×10^{-4} $lb/ft^2/s$]}.

2.2.2.2 Model Results for the Low-Temperature Operating Mode

The drift conditions and performance of the ventilation system during the low-temperature operating mode are summarized in Figure 2-7. In this simulation, the ventilation rate was stepped down from 15 to 3 m^3/s [529 to 106 cfs] at 50 years and then from 3 to 1.5 m^3/s [106 to 53 cfs] at 100 years. The reduced rate after 50 years was meant to simulate the effects of natural ventilation. In reality, natural ventilation should cause a gradual decline in the ventilation rate as the waste package cools off. The ventilation model as currently written did not allow a self-consistent calculation for natural ventilation; the piecewise constant ventilation rate was used until a more complete model becomes available. The heat transfer coefficient was 1.89 $W/(m^2\ °C)$ at 15 m^3/s [529 cfs] and was scaled by flow rate to the 0.8 power for the other ventilation rates. Power output of the waste package was set at a line-averaged load of

1 kW/m. The other parameters were the same as the basecase for the high-temperature operating mode described in Section 2.2.2.1.

In the low-temperature operating mode, the waste package temperature peaked at approximately 85 °C [185 °F] around 4 years. The time of maximum waste package temperature was nearly the same as in the high-temperature operating mode and was controlled mostly by the time constant for heat conductance into the drift wall. There were also sudden increases in the waste package temperature and associated increases in the power delivered to the drift wall as the air flow rate was stepped down at 50 and 100 years. With a sudden decrease in the ventilation rate, the waste package quickly became hotter, but the rock mass around the drift responded slowly to the change. Thus, for a brief period of time, the temperature difference between the drift and the waste package was increased and thermal radiation became more effective at transferring heat to the drift wall.

2.3 Conclusions from Preclosure Ventilation Model

Chapter 2 and Appendix A describe a model for preclosure in-drift conditions fully coupled with a thermohydrologic simulation including thermal radiation from waste package to drift wall, forced air ventilation, convective heat transport from the waste package and the drift wall to the ventilation air, and drying of the drift wall by the ventilation air. The main conclusions of this modeling study are

- Ventilation at a flow rate of 15 m^3/s [529 cfs] removes approximately 89 percent of the heat at the drift inlet and approximately 77 percent of the heat at the drift outlet, integrated over 50 years.
- The effect of moisture loss on heat removal is negligible.
- Temperature differences between the inlet and outlet can reach 20 °C [68 °F]. The percentage of heat removed is larger than the 70 percent assumed by DOE in the Multiscale Thermohydrologic Model.
- Maximum waste package temperature in the preclosure period is 95 °C [203 °F] for the high-temperature operating mode and 85 °C [185 °F] for the low-temperature operating mode.

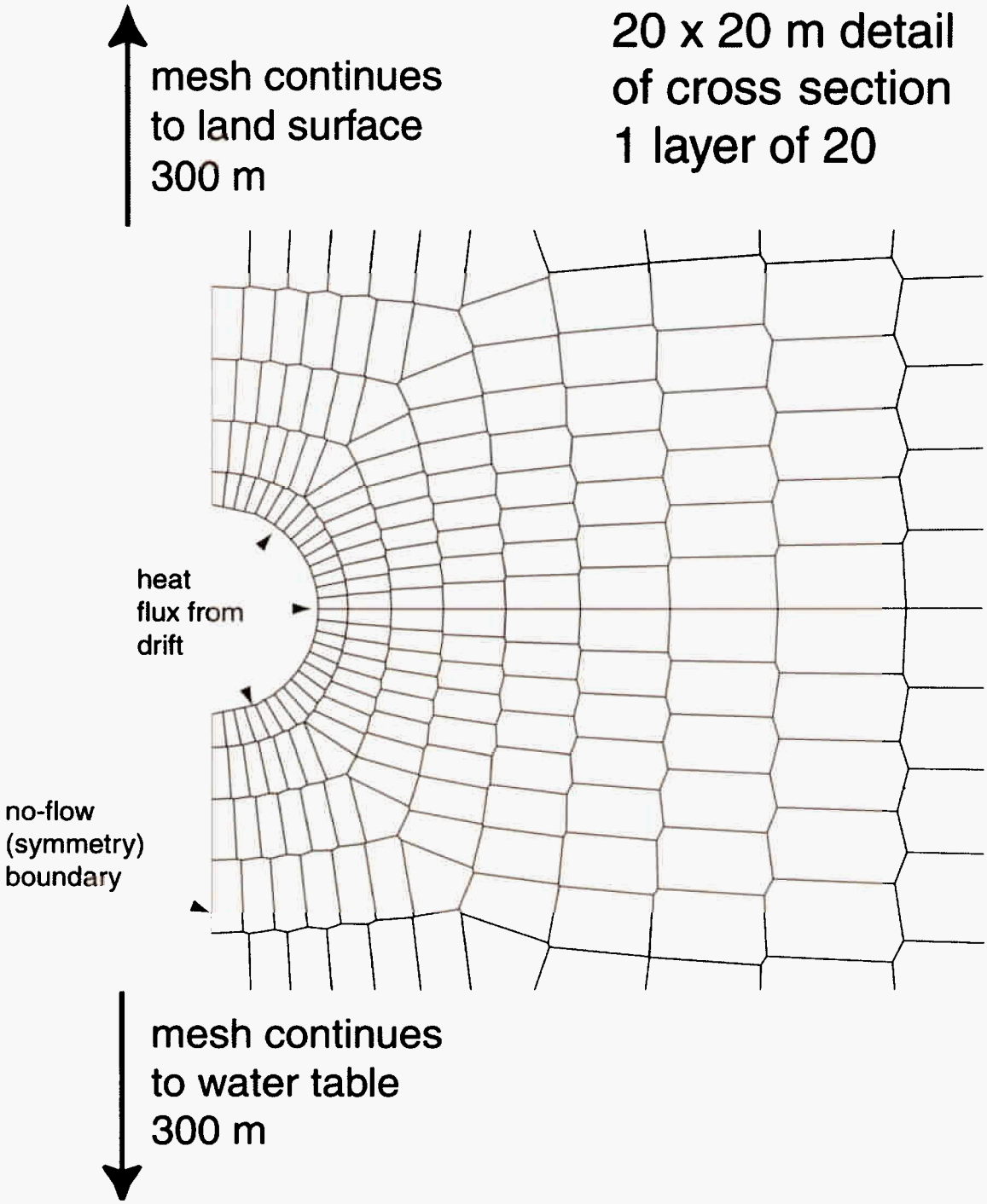

Figure 2-1. Detail of One Vertical Slice Out of Twenty in the Three-Dimensional METRA Ventilation Model [m = 3.28 ft]. An Unstructured Grid Is Used to Provide Detail Near the Drift Wall. The Drift Wall Is Modeled as a No-Flow Boundary with a Specified Heat Flux That Is Calculated from New Ventilation Model.

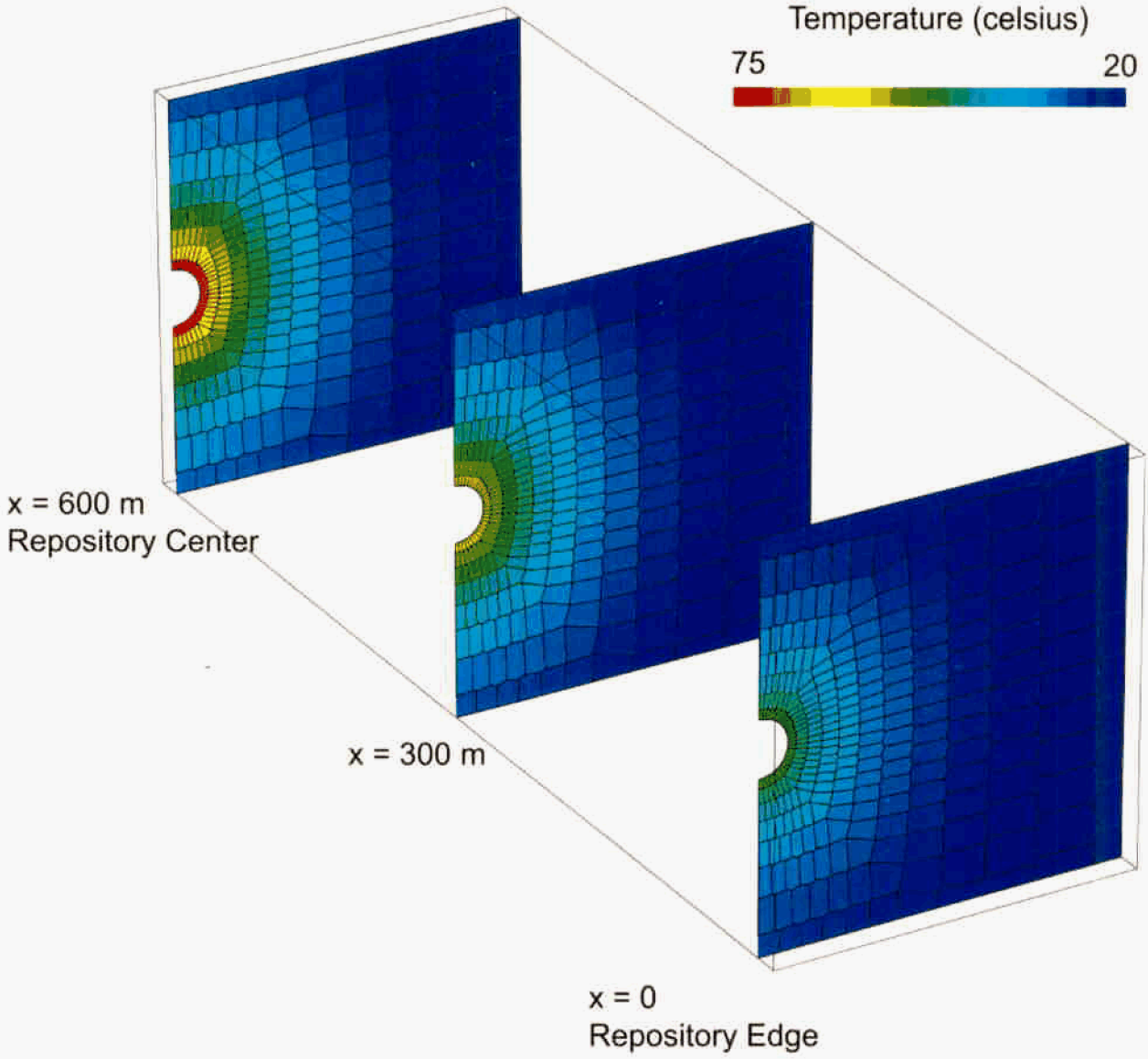

Figure 2-2. Temperature at 4 Years, Neglecting Moisture Removal, Near the Drift at Three Locations Along the Length of the Drift (Inlet, Middle, and Outlet). The Ventilation Rate is 10 m^3/s [353 cfs]. Ventilation Air Enters at the Repository Edge (Inlet at x = 0) and Exits at the Repository Center (Outlet at x = 600 m). [m = 3.28 ft], [The Temperature Scale Runs From 68 °F to 167 °F]

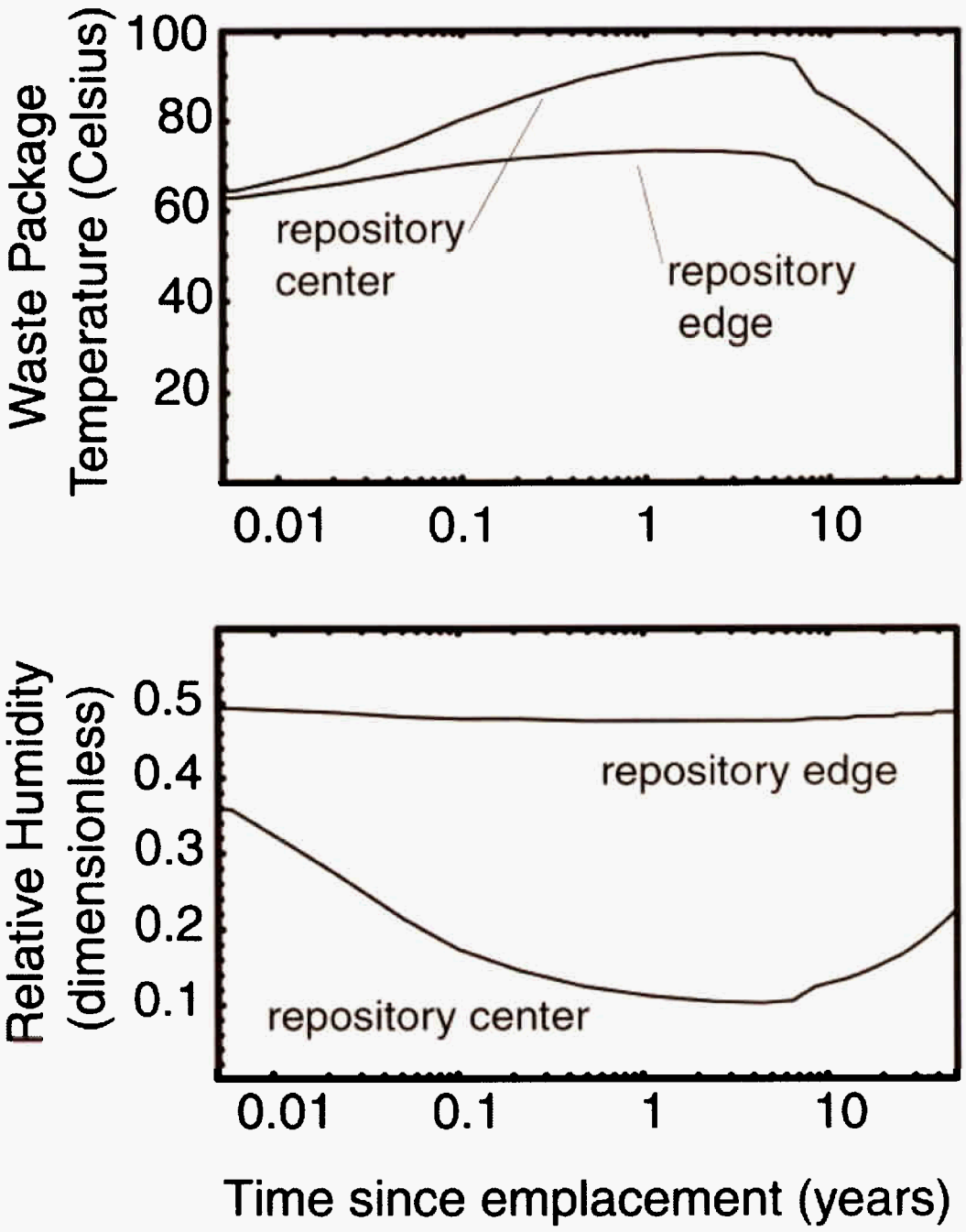

Figure 2-3. Waste Package Temperature and Relative Humidity, Neglecting Moisture Removal, in the Drift During the Preclosure Period for the High-Temperature Operating Mode. Repository Edge Is the Ventilation Inlet and Repository Center Is the Ventilation Outlet.

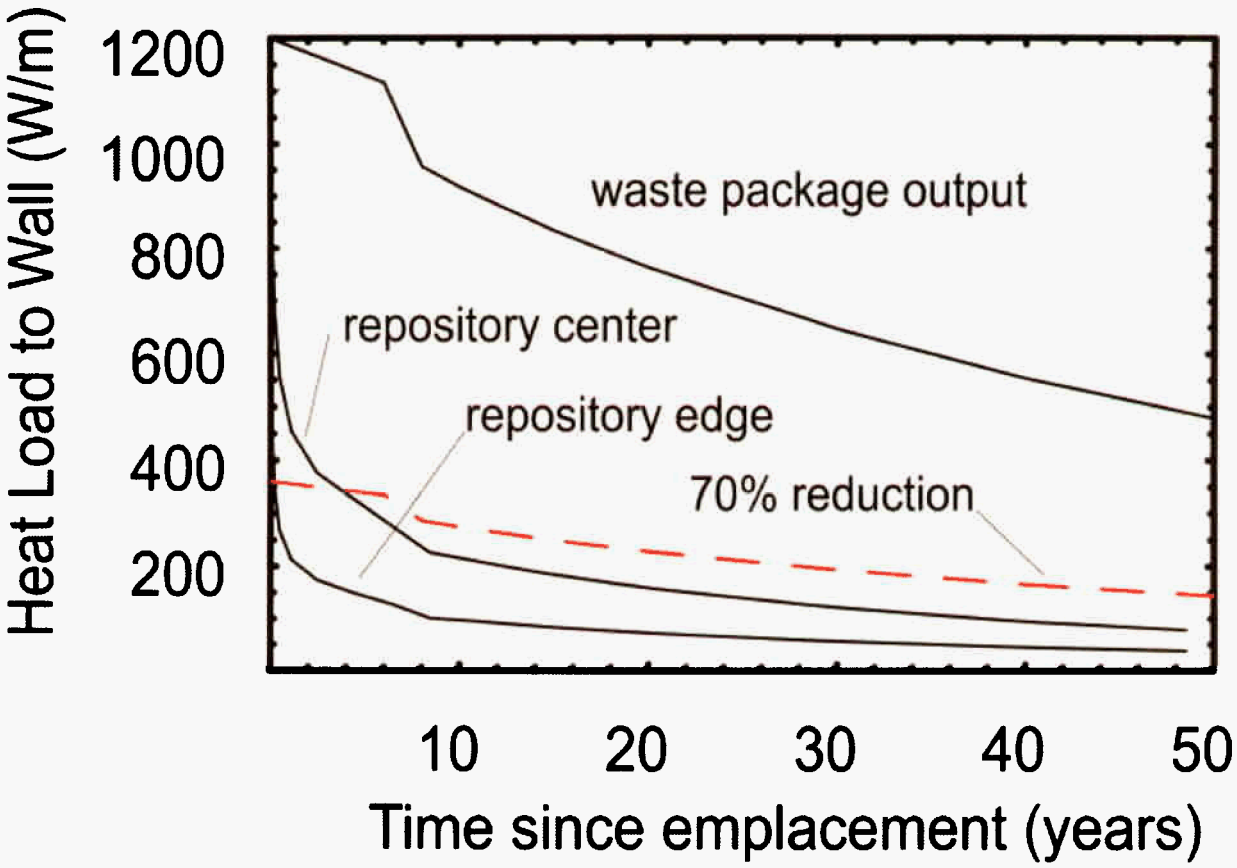

Figure 2-4. Power Delivered to the Wall (W/m) During the Preclosure Period for the High-Temperature Operating Mode, Neglecting Moisture Removal. Also Shown (Uppermost Curve) is the Waste Package Decay Heat for Comparison Purposes, the DOE Modeling Assumption of 70 Percent Heat Removal is Also Shown (Dashed Line). Repository Edge is the Ventilation Inlet and Repository Center is the Ventilation Outlet.

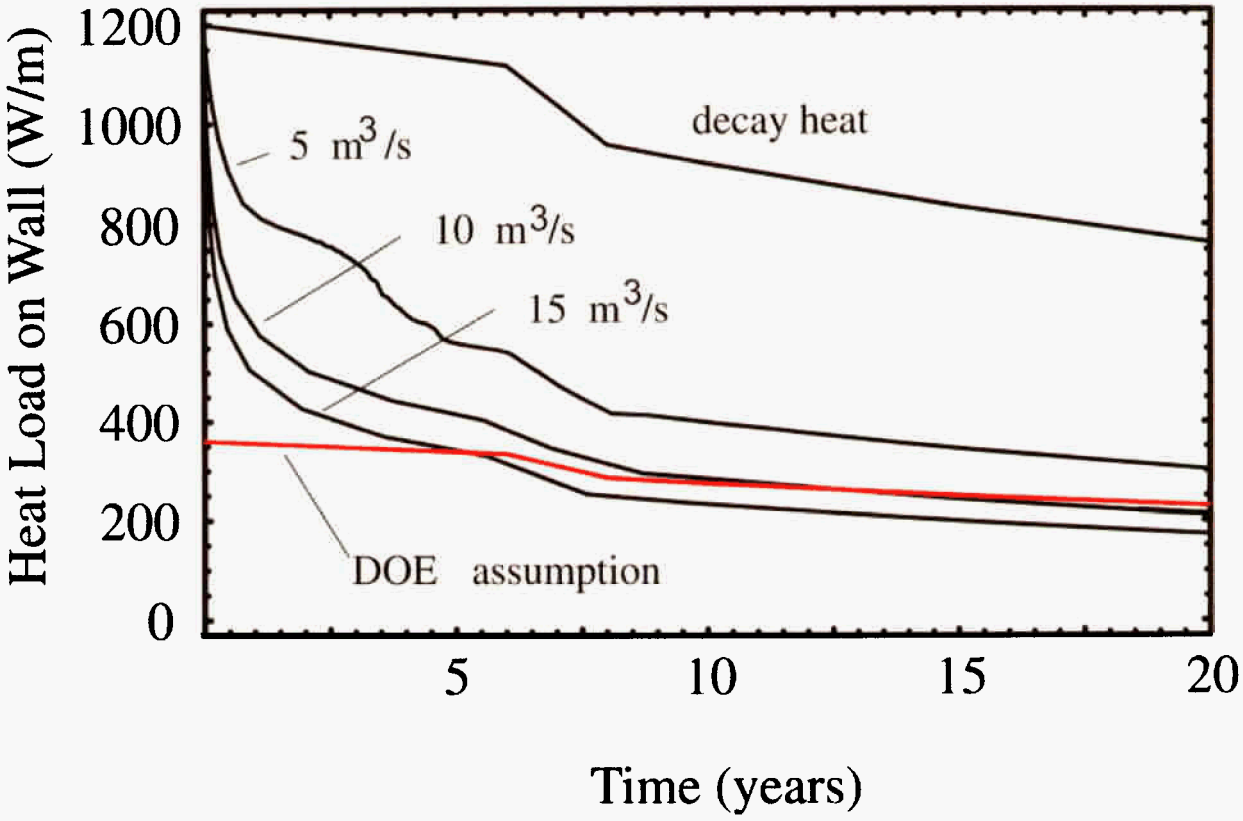

Figure 2-5. Effect of Ventilation Rate on Power Delivered to the Wall (W/m) at the Repository Center, Neglecting Moisture Removal

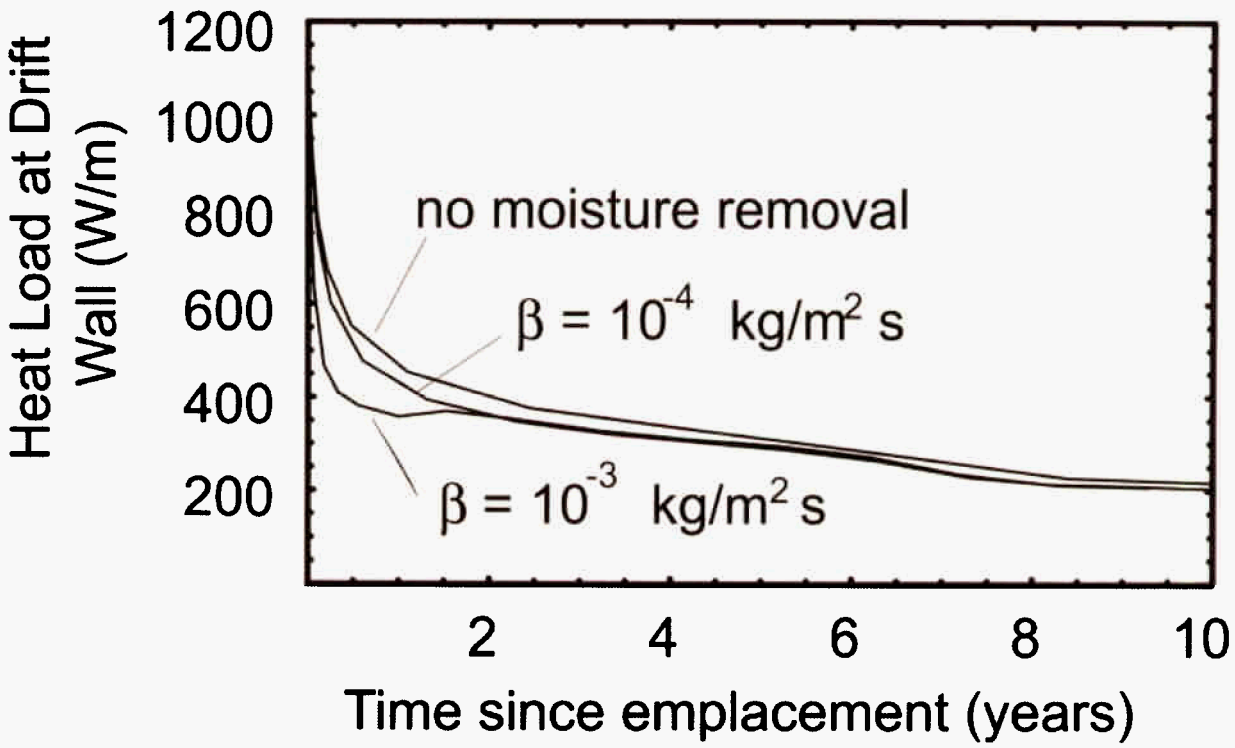

Figure 2-6. Effect of Moisture Removal on Power Delivered to the Wall (W/m) at the Repository Center for the High-Temperature Operating Mode

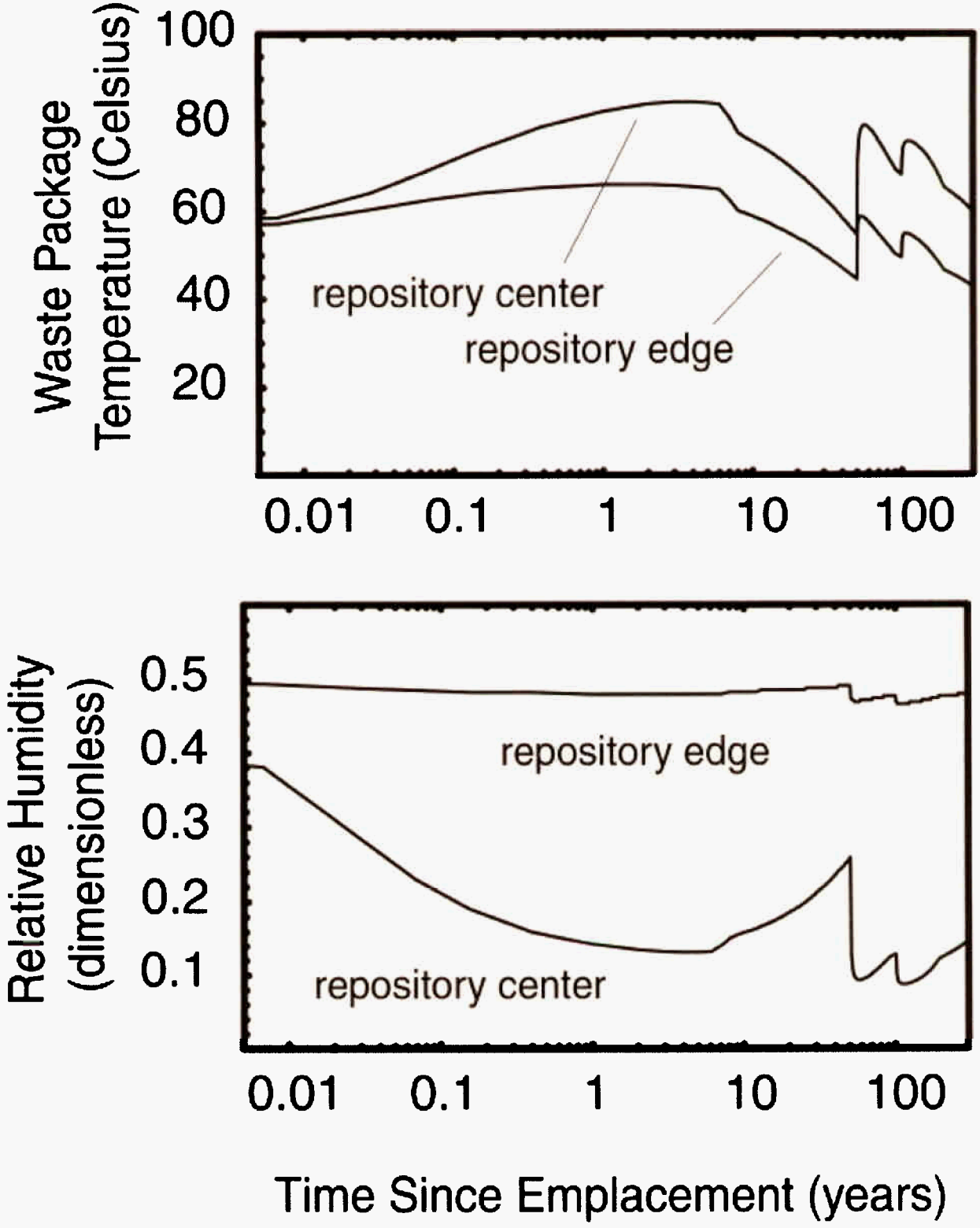

Figure 2-7. Relative Humidity in Drift and Waste Package Temperature at Edge and Center of the Repository in the Low-Temperature Operating Mode. Repository Edge is the Ventilation Inlet and Repository Center is the Ventilation Outlet.

3 REPOSITORY-SCALE THERMOHYDROLOGIC MODEL

3.1 DOE Approach and Relevant Technical Exchange Agreements

The field variables, temperature, pressure, relative humidity, saturation, mass flux, and evaporation rate, are estimated for DOE performance assessments by the Multiscale Thermohydrologic Model. The multiscale thermohydrologic model analysis and model report (CRWMS M&O, 2000c) provided field variables for emplacement drifts backfilled with sand prior to closure. Peak temperatures on the waste packages for 50 years of forced ventilation and backfilled prior to closure exceeded 300 °C [572 °F]. The multiscale thermohydrologic model analysis and model report (CRWMS M&O, 2000d) provided field variables for emplacement drifts with 50 years of forced ventilation both with and without backfill at the time of closure. The maximum peak temperature on a waste package surface for drifts without backfill was 186 °C [367 °F], and mean waste package surface temperatures were in the range of approximately 150 °C [302 °F] to 170 °C [338 °F]. The DOE will provide the multiscale thermohydrologic model analysis and model report in July 2001,[1] and the multiscale thermohydrologic model analysis and model report in fiscal year 2002,[2] as agreed to at the DOE and NRC technical exchange[3] in Agreement TEF.2.04, which states

> "Provide the Multi-Scale Thermohydrologic Model AMR, Rev. 01. The DOE will provide the Multi-Scale Thermohydrologic Model AMR (ANL–EBS–MD–00049) Rev. 01 to the NRC. Expected availability is FY 02."

At the time of this report, neither of these documents have been received. The Multiscale Thermohydrologic Model presented in CRWMS M&O (2000d) consists of four interrelated submodels. At the mountain scale, temperatures were calculated with the smeared heat load. Mountain-scale thermal model represented the entire repository footprint as a uniform planar heat source and calculated temperatures in three dimensions analytically. The only submodel of the Multiscale Thermohydrologic Model that explicitly incorporates hydrology is the line-averaged heat load, drift-scale thermohydrologic model. This model is a dual-continuum, two-dimensional cross section of a single drift extending from ground surface to below the water table. The line-averaged heat load, drift-scale thermohydrologic model submodel was run at 31 locations within the repository footprint using hydrostratigraphic properties for each location derived from the calibrated properties analysis and model report (CRWMS M&O, 2000e). The relationship between the smeared heat load, mountain-scale thermal model and line-averaged heat load, drift-scale thermohydrologic model at various submodel locations was determined using a smeared heat load, drift-scale thermal model. Finally, variations in thermal output from different waste types and the effect of thermal radiation within drifts was accounted for using the discrete heat load, drift-scale thermal model.

---

[1]CRWMS M&O. "Multiscale Thermohydrologic Model." ANL–EBS–MD–000049. Revision 00 ICN 03. North Las Vegas, Nevada: CRWMS M&O. To be published (2002).

[2]CRWMS M&O. "Multiscale Thermohydrologic Model." ANL–EBS–MD–000049. Revision 01. North Las Vegas, Nevada: CRWMS M&O. To be published (2002).

[3]DOE and NRC. "Technical Exchange and Management Meeting on Thermal Effects on Flow, January 8–9, 2001." Pleasanton, California. 2001.

The purpose of CNWRA evaluation of the Multiscale Thermohydrologic Model was not to reproduce results from all the various submodels but to investigate potentially significant aspects of thermal hydrology in the Multiscale Thermohydrologic Model, provide technical support to staff evaluation of the Multiscale Thermohydrologic Model, and to provide waste package temperature and relative humidity data as a function of time to other models and analyses requiring information on in-drift conditions. CNWRA constructed a model analogous to the line-averaged heat load, drift-scale thermohydrologic model at a central location in the repository footprint. This chapter describes the model development, compares the results with the line-averaged heat load, drift-scale thermohydrologic model submodel at the same location, then evaluates the sensitivity of model results to net infiltration, assumptions about thermal loading, and the repository host rock. Temperature and relative humidity at the waste package are combined from the preclosure model described in Chapter 2 and the postclosure model described in Section 3.3 and are presented in Appendix B.

3.2 Comparison of Model Results with the DOE Line-Averaged Heat Load, Drift-Scale Thermohydrologic Model

A dual-continuum model was constructed with a domain geometry similar to the line-averaged heat load, drift-scale thermohydrologic model submodel at a location in the repository footprint with coordinates 170,717.1 m [560,122.8 ft] easting, 233,795.7 m [167,083.7 ft] northing, Nevada State Plane Coordinates North American Datum Twenty Seven, which is referred to as location l4c3 in the Multiscale Thermohydrologic Model analysis and model report (CRWMS M&O, 2000d). The modeled domain and numerical grid at location l4c3, are shown in Figure 3-1. The left boundary of the two-dimensional cross section is the centerline of an emplacement drift, and the right boundary is the centerline of the pillar between emplacement drifts. These no-flow boundaries create symmetry such that continuations beyond the boundaries to the left and right are mirror images of the modeled domain. No-flow boundary conditions along the axes of symmetry are applicable for horizontally layered, homogeneous formation properties in the central portion of the repository. Thus, the model does not account for heterogeneity within a layer, dipping of hydrostratigraphic layers, or edge effects. Refinement of the grid in the vicinity of the drift is shown in Figure 3-2. Hydrostratigraphy used in the model was taken from Table 6-1, hydrologic and thermal properties of the hydrostratigraphic units were taken from Tables 4-2 through 4-4, boundary conditions were taken from Table 6-3, and elevations were taken from Table 6-2 of the Multiscale Thermohydrologic Model analysis and model report (CRWMS M&O, 2000d). Net infiltration at the surface boundary was set to 10 mm/yr [0.39 in/yr] for 0–600 years, 24 mm/yr [0.9 in/yr] for 600–2,000 years, and 38.7 mm/yr [1.52 in/yr] for 2,000–10,000 years. The repository elevation at location l4c3 is 1,073.1 m [3,520.84 ft] above sea level, 343.1 m [1,125.71 ft] above the water table, and there is a 326.6-m [1,071.57-ft] overburden thickness above the repository elevation to the ground surface. A linear, geothermal gradient was imposed on the ambient system from 16.5 °C [61.7 °F] at the ground surface to 32.4 °C [90.32 °F] at the water table.

A heat source, representing the thermal loading resulting from decay of radioactive waste for a high-temperature operating mode, was placed in the four model elements inside the drift adjacent to the left boundary as shown in Figure 3-2. The thermal energy source used in this comparison was taken from the Multiscale Thermohydrologic Model input files transmitted to

NRC in accordance with an agreement reached at the DOE and NRC technical exchange.[4] Ventilation in this comparison is represented by a uniform 70-percent reduction in thermal load for the 50-year preclosure period.

3.2.1 Temperature Comparisons for Uniform Heat Removal by Ventilation

Figure 3-3 shows temperatures as a function of time calculated using METRA compared with results from the line-averaged heat load, drift-scale thermohydrologic model submodel at the waste package, 5 m [16.4 ft] above the drift crown, and near the pillar center. This comparison shows that the greatest difference in temperature between the METRA and line-averaged heat load, drift-scale thermohydrologic model simulations occurs at the waste package and that the difference between the two models decreases away from the waste package. The difference in temperatures of the line-averaged heat load, drift-scale thermohydrologic model and METRA simulations is attributed to the treatment of in-drift conditions. The line-averaged heat load, drift-scale thermohydrologic model submodel implemented thermal radiation inside the drift as a temperature-dependent effective thermal conductivity whereas the material representing drift space in the METRA simulation was given a constant thermal conductivity of 10 W/(m K).

3.2.2 Relative Humidity and Fracture Flux Comparisons

Figure 3-4 shows relative humidity at the invert below the heat source obtained from the METRA simulation compared with the line-averaged heat load, drift-scale thermohydrologic model result. Note that these METRA results are applicable to the postclosure period only, which extends from 50 to 10,000 years in these simulations. The model for preclosure including ventilation is described in Chapter 2. The postclosure model described here represents the effects of ventilation only as a 70-percent reduction in thermal loading with drifts completely closed. This assumption resulted in a relative humidity of 1.0 during the preclosure period which is incorrect. In-drift relative humidity during the preclosure period depends on relative humidity of the ventilation air as indicated in Figure 2-3.

Figure 3-5 shows liquid flux in the fracture continuum at 5 m [16.4 ft] above the drift crown. The initial peak of liquid flux in Figure 3-5 at 5 m [16.4 ft] above the drift crown occured immediately after repository closure. A corresponding drop in relative humidity in the invert was seen at the same time in Figure 3-4. Abrupt changes in flux at 600 and 2,000 years resulted from increased net infiltration corresponding to climate changes. The difference between fracture fluxes simulated using METRA and the line-averaged heat load, drift-scale thermohydrologic model submodel of the Multiscale Thermohydrologic Model is significant and shows the sensitivity of simulated fracture flux to underlying assumptions. At the time staff undertook this modeling study, MULTIFLO Version 1.5, including the capabaility of implementing the active fracture model (Liu, et al., 1998) or any other relative permeability function for fracture to matrix flow, had not been released. Staff implemented the relative permeability and capillary pressure constitutive functions of saturation for the fracture continuum according to the active fracture conceptual model, but used a constant fracture matrix interaction factor derived from the ambient fracture saturations. This approximation to the active fracture conceptual model had the effect of slightly reducing fracture–matrix interaction at elevated saturations compared with

---

[4]DOE and NRC. "Technical Exchange and Management Meeting on Thermal Effects on Flow, January 8–9, 2001." Pleasanton, California. 2001.

the fully implemented active fracture model. This reduction may explain the earlier peak fracture flux in the METRA simulation relative to the results from the line-averaged heat load, drift-scale thermohydrologic model submodel. Modeled fluxes in the fracture continuum at 5 m [16.4 ft] above the drift crown are highly variable, dependent on assumptions about fracture–matrix interactions, relative fracture permeability, and the location of the dryout and refluxing zones.

3.2.3 Temperature Comparisons Using Ventilation Model Heat Reduction

In the previous model comparisons between METRA simulations and the line-averaged heat load, drift-scale thermohydrologic model submodel, ventilation during the preclosure period was implemented as a uniform constant reduction of 70 percent in the heat load data for both models. As discussed in Chapter 2, however, heat reduction during the first few years of preclosure ventilation was much less than 70 percent, and heat reduction during the later part of the preclosure period was greater than 70 percent. Figure 3-6 shows the heat loading data used by DOE for the line-averaged heat load, drift-scale thermohydrologic model submodels reduced by a constant 70 percent during preclosure compared with the same heat loading data reduced by time-dependent factors calculated using the ventilation model presented in Chapter 2. Figure 3-7 shows waste package temperature calculated using METRA with a constant 70-percent heat reduction representing preclosure ventilation and with heat reduction calculated using the ventilation model compared with results from the line-averaged heat load, drift-scale thermohydrologic model submodel. As reported in Chapter 2, heat reduction calculated from the ventilation model integrated over the 50-year preclosure period was 77 percent at the inlet end of the drift. This increased heat reduction dropped the peak postclosure waste package temperature from about 162 °C [323.6 °F] to about 156.6 °C [313.88 °F] in the METRA simulations.

3.2.4 Comparison of Results

This section describes a straightforward model comparison of a thermohydrologic model developed by staff using METRA and results from the line-averaged heat load, drift-scale thermohydrologic model submodel of the Multiscale Thermohydrologic Model. Statistical measures of the model comparisons are given in Table 3-1.

Significant differences in the model for the METRA simulations as compared to the line-averaged heat load, drift-scale thermohydrologic model submodel of the Multiscale Thermohydrologic Model are in the implementation of details inside the drift and the active fracture model for fracture–matrix interaction. Material properties representing space inside the open drift for the METRA simulations are given a constant thermal conductivity, whereas in the line-averaged heat load, drift-scale thermohydrologic model effective, thermal conductivity is a function of temperature. This is the most likely reason for temperature differences shown in Figure 3-3. Fracture–matrix interaction was incorporated into the METRA simulations using properties obtained from the calibrated properties analysis and model report (CRWMS M&O, 2000e) in the relative permeability and capillary pressure functions, but the fracture–matrix interaction factor was constant. This is the most likely explanation for differences in the extent of fracture dryout and rewetting that appeared in fluxes taken from 5 m [16.4 ft] above the drift crown (Figure 3-5). These differences show that minor changes in assumptions about relative

Table 3-1. Statistical Comparisons of Line-Averaged Heat Load, Drift-Scale Thermohydrologic (Indicated as LDTH in the Table) and METRA Simulations for the High-Temperature Operating Mode

Parameter	Location	Results				
		Case	Maximum/ Minimum Value	Time (Year)	Average Difference	Standard Deviation
Temperature (°C) (Maximum Value)	Waste Package (Figure 3-3)	LDTH	154.70 [310.46 °F]	70		
		METRA	161.98 [323.46 °F]	70	1.92	2.09
	5 m [16.4 ft] Above the Drift (Figure 3-3)	LDTH	94.80 [202.64 °F]	120		
		METRA	97.00 [206.60 °F]	120	1.86	0.96
	Near Center of Pillar (Figure 3-3)	LDTH	86.40 [187.52 °F]	800		
		METRA	87.20 [188.96 °F]	800	0.66	0.41
Relative Humidity (Minimum Value)	Invert (Figure 3-4)	LDTH	0.160	70		
		METRA	0.170	70	0.02	0.03
Liquid Flux Rate (mm/yr)	5 m [16.4 ft] Above the Drift (Figure 3-5)	LDTH	90.20 [3.55 in/yr]	70		
		METRA	92.50 [3.64 in/yr]	55	-0.55	19.50

fracture permeability and fracture–matrix interaction can produce significant changes in simulated fracture fluxes. This result highlights the uncertainties in modeled fracture fluxes and suggests that ranges of potential fluxes are not adequately represented by the line-averaged heat load, drift-scale thermohydrologic model submodel of the Multiscale Thermohydrologic Model.

3.3 Repository-Scale Model for Near-Field Conditions

The METRA thermohydrologic simulations and the line-averaged heat load, drift-scale thermohydrologic model submodel results from the Multiscale Thermohydrologic Model (CRWMS M&O, 2000d) were compared in Section 3.2 using the same thermal loading data as the line-averaged heat load, drift-scale thermohydrologic model and a line-averaged load of 1.45 kW/m. In this section, the same domain at location l4c3 (Figure 3-1), with the same hydrostratigraphic properties, is modeled using thermal data obtained from TPA Version 4.0

code (Mohanty, et al., 2000). These data are a combination of 65-percent Pressurized Water Reactor and 35-percent Boiling Water Reactor fuel assemblies. A line-averaged thermal loading of 1.17 kW/m was calculated as

$$\text{Load}\left(\frac{W}{m}\right) = \text{Load in}\left(\frac{W}{MTU}\right) \times \left(\frac{MTU}{WP}\right) \times \text{Total WP} \times \frac{1}{\text{Total Drift Length}} \qquad (3\text{-}1)$$

where 26-year-old spent nuclear fuel was estimated to produce 920 W/MTU and 8,877 waste packages (each containing 7.89 MTU/WP) fill 54,923.7 m [180,204.5 ft] of drift length. In Eq. (3-1) W indicates Watts, WP indicates waste package, and MTU indicates metric tonnes of Uranium. Forced ventilation of 15 m^3/s [529 cfs] for a 50-year preclosure period was represented by reducing the heat load according to the ventilation model presented in Chapter 2.

3.3.1 Sensitivity to Net Infiltration

Net infiltration rates applied at the upper boundary in these simulations were based on the infiltration model used in TPA Version 4.0 code (Mohanty, et al., 2000). Table 3-2 gives net infiltration rates for present-day, monsoon, and glacial climates for a reference basecase, low infiltration, and high infiltration rates. The infiltration rates for the top boundary were based on a Monte Carlo analysis using 1,000 realizations and climatic conditions (precipitation and temperature) based on climate analog sites described in the Simulation of Net Infiltration for Modern and Potential Future Climates analysis and model report (CRWMS M&O, 2000f).

Figure 3-8 shows that the response of temperatures at the waste package, 5 m [16.4 ft] above the drift crown, and near the pillar midpoint to variations in net infiltration was relatively minor. For example, peak waste package temperature was 159.9 °C [319.82 °F] for the low flux case and 159.2 °C [318.56 °F] for the high flux case, a difference of less than 1 °C [33 °F]. Relative humidity at the waste package and in the invert is shown in Figure 3-9 for mean, low, and high net infiltration rates. The minimum relative humidity at the waste package was 0.141 for the low flux case and 0.143 for the high flux case. The net infiltration rate appears in Figure 3-9 to have the most effect on recovery of relative humidity following the minimum during the thermal period. Relative humidity at the waste package recovered in 0.65 at 1,090 years in the low-flux case and in 778 years in the high-flux case. Figures 3-8 and 3-9 indicate low sensitivity of waste package temperature and relative humidity to net infiltration rates in the range from 2.8 to 92.9 mm/yr [0.11 to 3.66 in/yr]. Water from infiltration rates in this range does not enter drifts as a consequence of the use of homogeneous rock properties and the capillary barrier effect. Waste package temperature and relative humidity, on the other hand, are dominated by the presence of the heat source inside drifts. The combination of these factors may explain the lack of sensitivity of waste package temperature and relative humidity to net infiltration rate.

3.3.2 Sensitivity to Thermal Load

Thermal output of commercial spent nuclear fuel waste packages varied significantly, from approximately 11.3 kW for 21 Pressurized Water Reactor absorber plates to 0.54 kW for 24 Boiling Water Reactor absorber plates (CRWMS M&O, 2000g). Sensitivity to thermal load was evaluated by assuming a line-averaged load of 1.03 kW/m, representing cooler waste

Table 3-2. Net Infiltration Rates Used for Sensitivity Analysis			
Time (year)	Low Flux (mm/yr)	Mean Flux (mm/yr)	High Flux (mm/yr)
0–600 (Present)	2.8 [0.11 in/yr]	6.0 [0.24 in/yr]	21.7 [0.85 in/yr]
600–2,000 (Monsoon)	6.0 [0.26 in/yr]	18.2 [0.72 in/yr]	64.5 [2.54 in/yr]
2000–10,000 (Glacial)	12.0 [0.67 in/yr]	32.2 [1.27 in/yr]	92.9 [3.66 in/yr]

packages, and a line-averaged load of 1.45 kW/m, representing hotter waste packages. In this sensitivity analysis, the mean flux (Table 3-2) was used with three different thermal loads representing mean (1.17 kW/m), hot (1.45 kW/m), and cool (1.03 kW/m) waste packages. Temperatures at the waste package, 5 m [16.4 ft] above the drift crown, and near the pillar center are shown in Figure 3-10 for mean, hot, and cool thermal loading conditions. Significant differences in waste package temperatures resulted from different thermal loading conditions. For a line-averaged thermal loading of 1.45 kW/m waste package, temperature peaked at 203.9 °C [399.0 °F] around 69 years, whereas waste package temperature peaked at 131.9 °C [269.4 °F] at around 83 years for a line-averaged thermal load of 1.03 kW/m, a difference of 72 °C [161.6 °F]. Similar trends in the sensitivity of relative humidity to variations in thermal loading are shown in Figure 3-11. Minimum relative humidity at the waste package ranged from 0.05 for a thermal loading of 1.45 kW/m to 0.3 for a thermal loading of 1.03 kW/m. These results show that in-drift conditions are sensitive to thermal load and indicate that conditions could vary significantly from differences in waste package thermal output.

3.3.3 Sensitivity to Host Rock

Thermal conductivity of the proposed repository host rock has a significant effect on the in-drift conditions of waste package temperature and relative humidity (CRWMS M&O, 2001b). The repository host rock at location l4c3 (Figure 3-1) occured in the lower lithophysal unit of the Topopah Spring Tuff (hydrostratigraphic unit tsw35), which has a dry thermal conductivity of 1.2 W/(mK) and a wet thermal conductivity of 2.02 W/(mK). To assess the effect of repository host rock on near-field and in-drift conditions, a second model was constructed at a location with coordinates 171,151.0 m [561,546.4 ft] easting and 233,773.2 m [767,009.9 ft] northing, Nevada State Plane Coordinates North American Datum Twenty Seven. This location is referred to as l4c1 in the Multiscale Thermohydrologic Model (CRWMS M&O, 2000d). The model domain, numerical grid, and a simplified hydrostratigraphy used to model thermohydrologic conditions at location l4c1 are shown in Figure 3-12. The proposed repository horizon at location l4c1 occured in the middle nonlithophysal unit of the Topopah Spring Tuff (hydrostratigraphic unit tsw34), which has a dry thermal conductivity of 1.56 W/(mK) and a wet thermal conductivity of 2.33 W/(mK). Note that the same heat load was used for both locations so the comparison shows only effects of hydrostratigraphy and repository host rock. Potential edge effects resulting from location l4c1 being closer to the edge of the repository are not accounted for in this comparison. Figure 3-13 shows temperatures at the waste package, 5 m [16.4 ft] above the drift crown, and near the pillar center of location l4c1

compared to location l4c3. The larger thermal conductivity of the middle nonlithophysal unit (hydrostratigraphic unit tsw34) allowed heat to escape from the near-field host rock around the drift resulting in lower waste package temperatures as compared to drifts in the lower lithophysal unit. Increased heat transport away from the waste package resulted in higher temperatures at 5 m [16.4 ft] above the drift crown and earlier increases in temperatures near the pillar center. Figure 3-14 shows the effect of hydrostratigraphy and repository host rock on relative humidity at the waste package and invert. Larger thermal conductivity of the middle nonlithophysal unit resulted in lower in-drift temperatures and higher minimum relative humidity at the waste package and invert. This sensitivity study concludes that waste package conditions are sensitive to thermal conductivity of the repository host rock.

3.3.4 Evaluation of Low-Temperature Operating Mode Repository

The Supplemental Science and Performance Analyses (CRWMS M&O, 2001b) evaluated several alternatives for a low-temperature operating mode repository. Below boiling temperatures were achieved in one alternative by increasing waste package spacing to 2 m [6.56 ft] and ventilating for 300 years. In this section, a comparison is made between a high-temperature operating mode and a low-temperature operating mode repository. The high-temperature operating mode is the same as the mean flux case in Section 3.3.1 (Figures 3-8 and 3-9) and the 1.17 kW/m line-averaged load case in Section 3.3.2 (Figures 3-10 and 3-11). This high-temperature operating mode case utilized 50 years of forced-air ventilation with heat reduction factors calculated from the ventilation model described in Chapter 2 and the heat loading data from TPA Version 4.0 code (Mohanty, et al., 2000). The low-temperature operating mode design[5] was evaluated using the model developed for location l4c3 by reducing the line-averaged loading to 1.0 W/m and using the heat reduction by ventilation for 50 years at 15 m^3/s [529 cfs] followed by 50 years at 3 m^3/s [105 cfs] and 1.5 m^3/s [52.9 cfs] for 200 years, calculated as described in Chapter 2. Postclosure model results presented in Chapter 3 are valid only after the ventilation period because the implementation of ventilation was through heat reduction only, and the repository was otherwise closed. This approach gave relative humidity of 1.0 during the ventilation period when, in fact, relative humidity would be very low during ventilation. Correct relative humidity for the preclosure ventilation period was obtained using the preclosure ventilation model described in Chapter 2. Temperature and relative humidity data presented here for the comparison of the low-temperature versus high-temperature operating modes combine results from the preclosure ventilation model with results from the postclosure model to give an accurate representation of repository conditions for both the preclosure and postclosure time periods. Figure 3-15 shows waste package temperature and relative humidity from the preclosure ventilation model for the preclosure period combined with results from the postclosure model from the end of ventilation to 10,000 years for the low-temperature operating mode compared with the high-temperature operating mode conditions. Maximum waste package temperature for the low-temperature operating mode design of 86.7 °C [188.1 °F] occurred at 545 years. Minimum waste package relative humidity for the low-temperature operating mode design of 0.89 occurred at 362 years. The spikes in relative humidity at 50 years for the high-temperature operating mode and at 300 years for the low-temperature operating mode in Figure 3-15 resulted from instantaneous closure of the repository. Relative humidity increased rapidly in response to termination of the dry ventilation air. A slower increase in temperature then drove relative humidity back down.

---

[5]Harrington, P. "YMP Thermal Design History." *Presentation to NRC August 2, 2001.* Rockville, Maryland. 2001.

The step changes in temperature and relative humidity at 100 and 300 years were a consequence of reduction in ventilation from 3 to 1.5 m^3/s [105 to 52.9 cfs] and repository closure. Waste package temperature and relative humidity results of the ventilation model for preclosure conditions were combined with postclosure model results at location l4c3 for both the high-temperature operating mode and low-temperature operating mode repository designs and presented numerically in Appendix B.

3.3.5 Summary of Chapter 3

The model developed and implemented in METRA (Lichtner, et al., 2000) was compared with the line-averaged heat load, drift-scale thermohydrologic submodel of the Multiscale Thermohydrologic Model in Section 3.2. These simulations used the heat load data obtained from input files for the Multiscale Thermohydrologic Model (CRWMS M&O, 2000d) and implemented ventilation as a uniform 70-percent reduction in heat load for 50 years. The comparisons showed a good match to temperature and relative humidity but a poorer match to liquid flux in fractures. The differences may be attributed to representation of in-drift conditions and implementation of the active fracture model (Liu, et al., 1998). The larger discrepancy in fracture fluxes shows the sensitivity of flow in fractures to model assumptions.

Peak waste package temperature in Figure 3-3 is 161.98 °C [323.56 °F] for an initial line-average heat load of 1.45 kW/m, whereas peak waste package temperature in Figure 3-10 is 203.9 °C [399.02 °F] for an initial line-average heat load of 1.45 kW/m. This apparent discrepancy is explained by the difference in heat curve data obtained from the input files to the Multiscale Thermohydrologic Model (CRWMS M&O, 2000d) and the 21 Pressurized Water Reactor data obtained from TPA Version 4.0 code (Mohanty, et al., 2000). Even though both start at an initial line-average heat load of 1.45 kW/m, the 21 Pressurized Water Reactor data from TPA Version 4.0 code decayed more slowly, being 0.703 kW/m at 50 years while the heat curve data from the Multiscale Thermohydrologic Model (CRWMS M&O, 2000d) dropped to 0.578 kW/m. Results of a repository-scale thermohydrologic model implemented with METRA are presented in Section 3.3. This model used the same hydrostratigraphy and properties as those in the comparison with the line-averaged heat load, drift-scale thermohydrologic submodel of the Multiscale Thermohydrologic Model, but used head curve data from TPA Version 4.0 code (Mohanty, et al., 2000) and heat reduction factors for ventilation obtained from the preclosure ventilation model described in Chapter 2.

Results of sensitivity analyses indicate that waste package temperature and relative humidity are relatively insensitive to net infiltration in the range from 2.8 to 92.9 mm/yr [0.11 in/yr to 3.66 in/yr]. In-drift conditions are most sensitive to thermal output of the waste inventory. In-drift conditions are also sensitive to thermal conductivity of the repository host rock. Pillars between drifts remained below boiling for the entire thermal period in the high-temperature operating mode design, allowing for condensate drainage to below the repository. Maximum waste package temperature in the low-temperature operating mode design was less than 87 °C [188.6 °F] assuming a line-average thermal loading of 1.0 W/m. Combined results of in-drift temperature and relative humidity conditions for both the low-temperature operating mode and high-temperature operating mode designs from the preclosure model presented in Chapter 2 and the postclosure model presented in Chapter 3 are given in Appendix B.

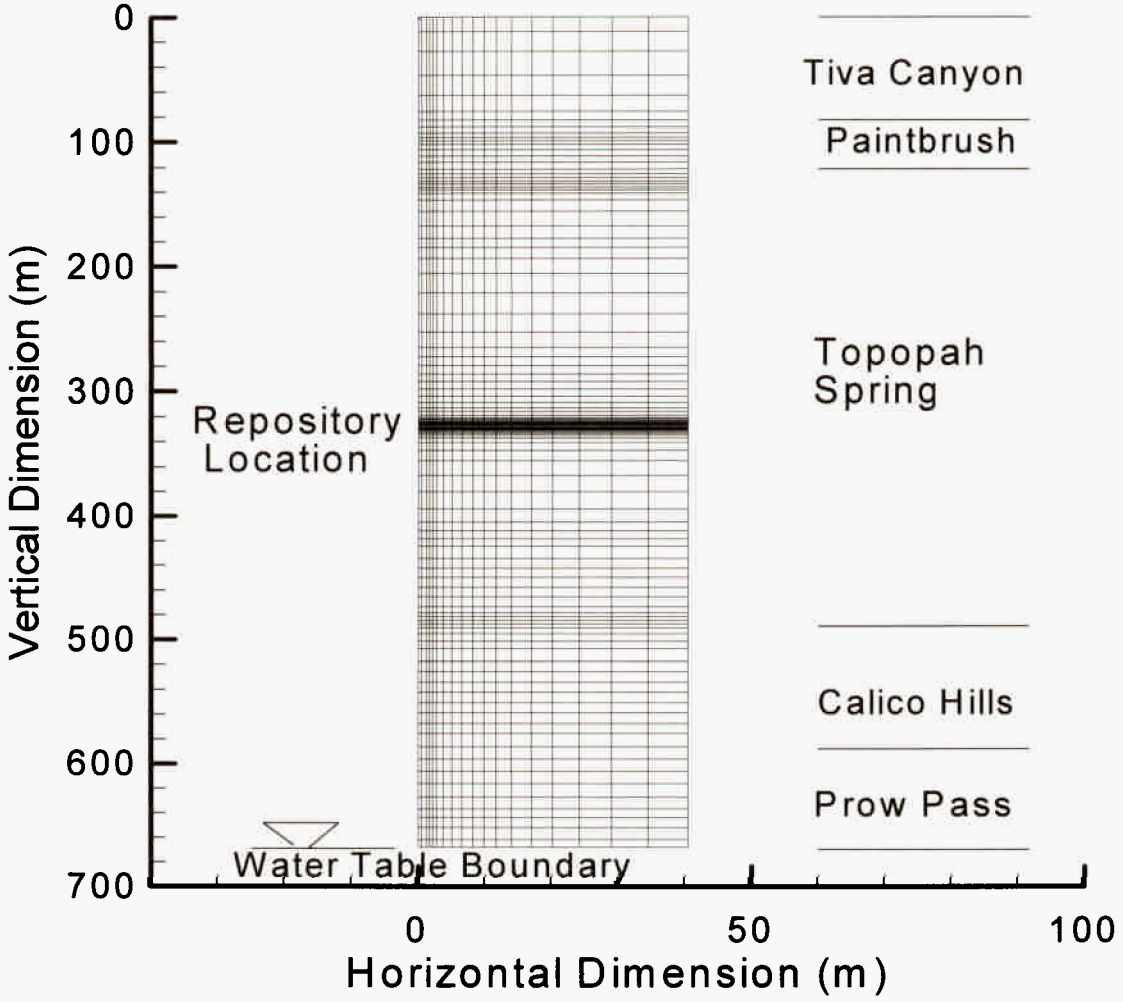

Figure 3-1. Domain and Numerical Mesh Used for the Thermohydrologic Model at the Central Repository Location Labeled l4c3. Major Hydrostratigraphic Formations and Approximate Repository Location are Indicated. [m = 3.28 ft]

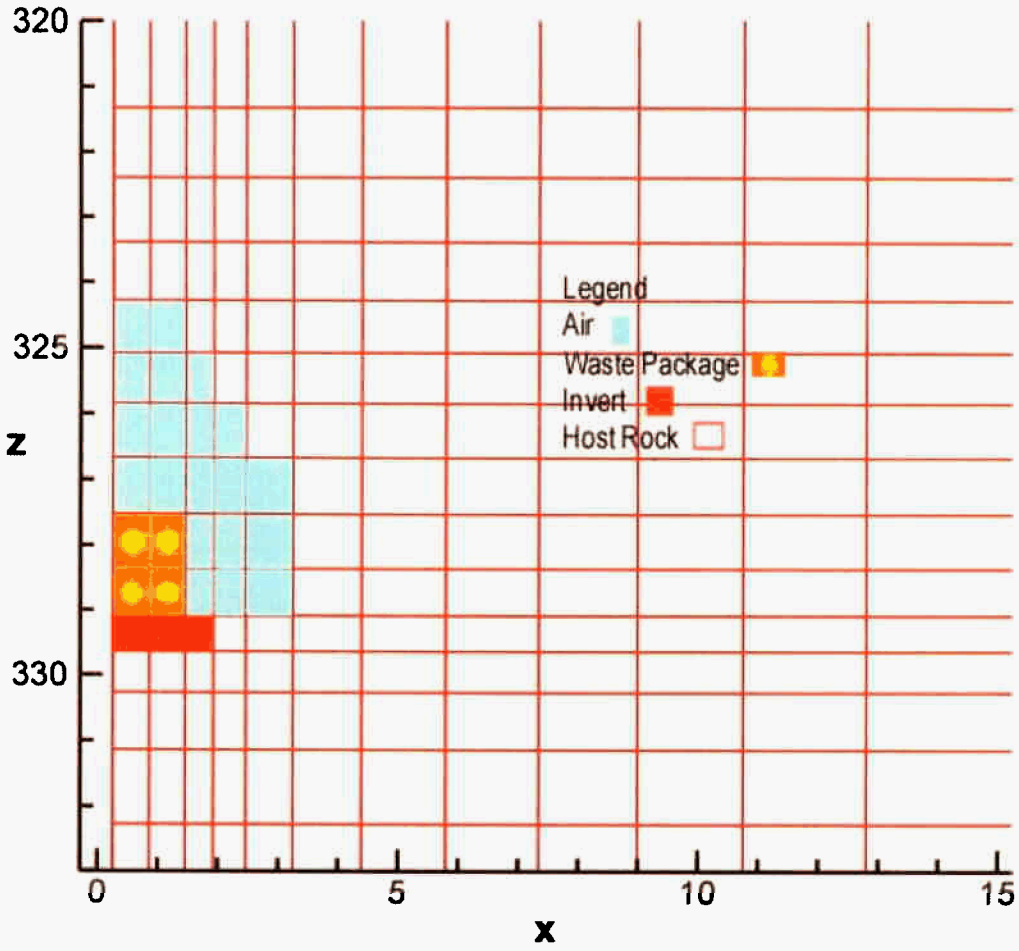

Figure 3-2. Expanded View of Numerical Grid Refinement in the Vicinity of the Heated Drift. The Thermal Load Is Applied to the Four Grid Elements Immediately Above the Invert. Material Properties Representing Air Are Such That Capillary Pressure Is Zero for All Saturations. The Effect of Thermal Radiation Is Accounted for by an Effective Thermal Conductivity.

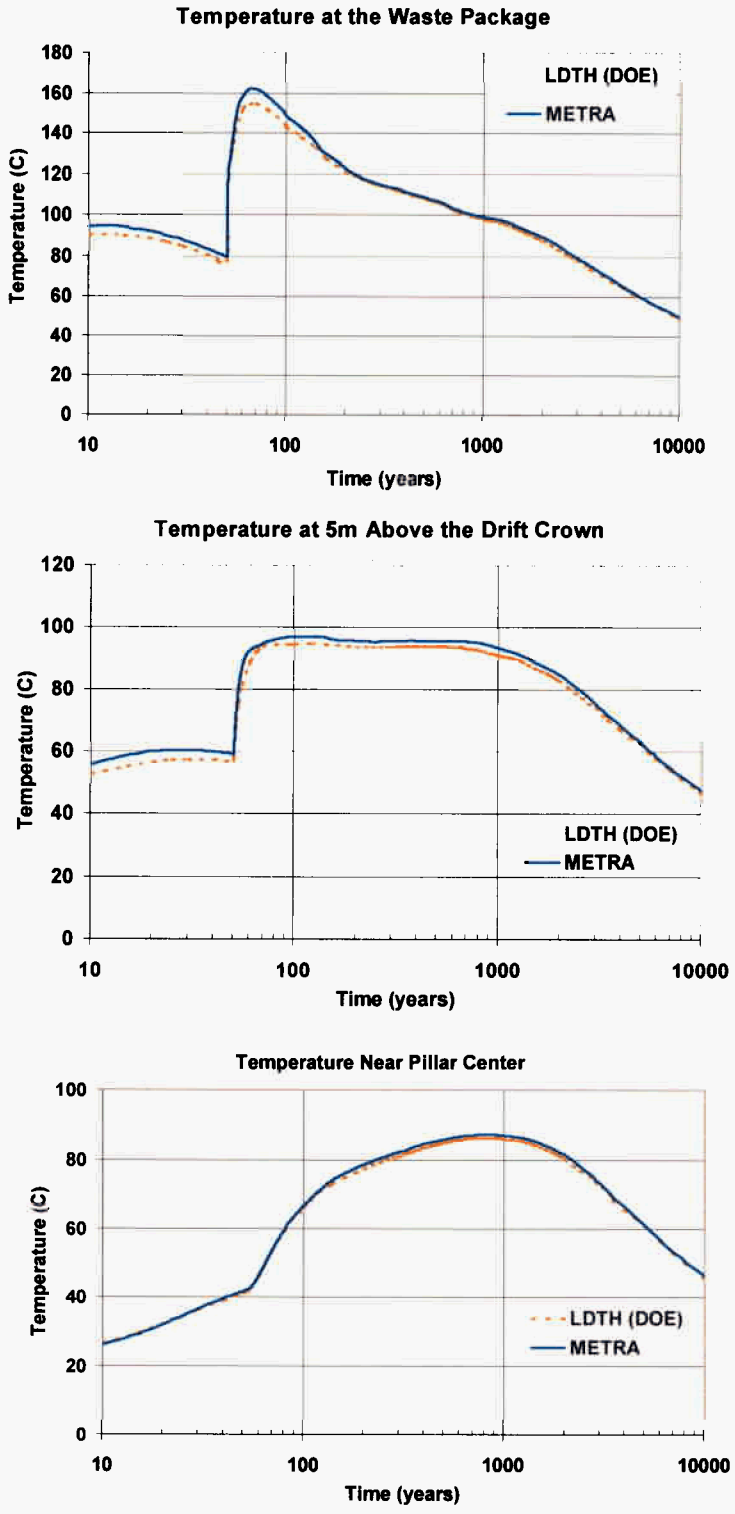

Figure 3-3. Temperatures Calculated Using METRA at the Central Repository Location Labeled l4c3 Compared with Results from the Line-Averaged Heat Load, Drift-Scale Thermohydrologic Model [Indicated as LDTH (DOE) in the Plots] Submodel of the Multiscale Thermohydrologic Model [m = 3.28 ft]

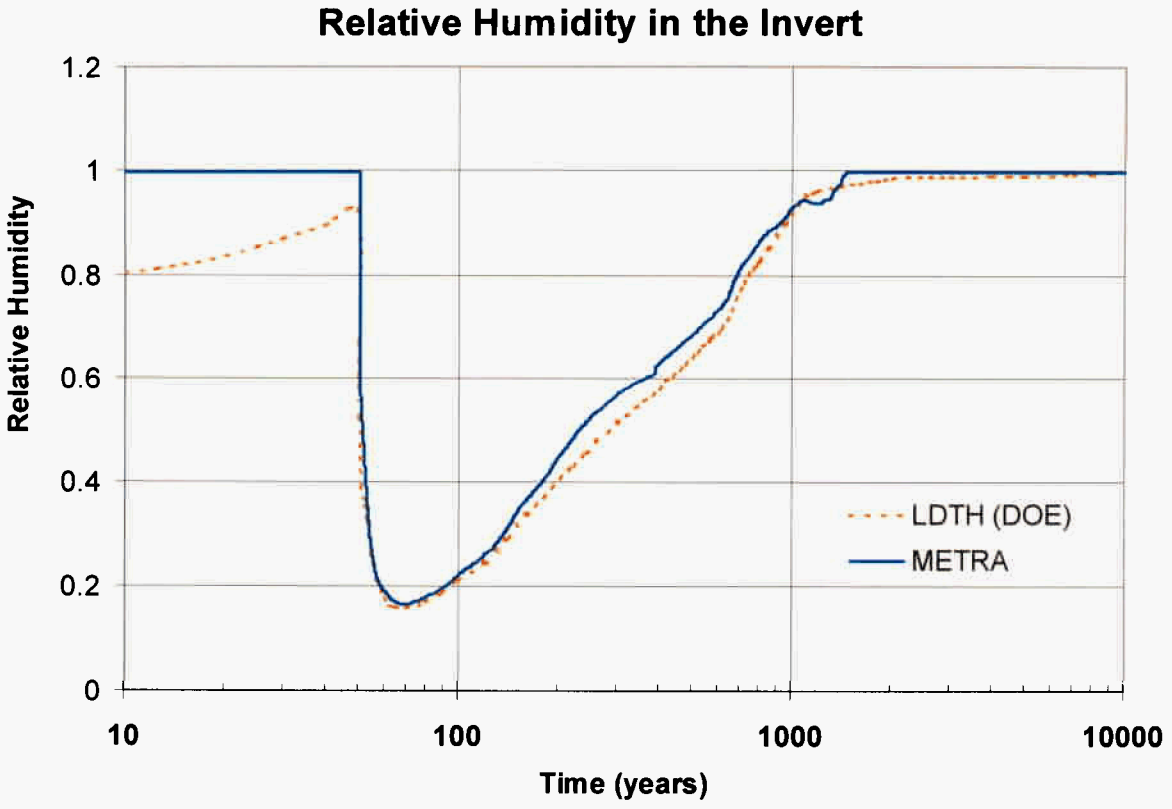

Figure 3-4. Relative Humidity in the Invert Calculated Using METRA Compared with Results from the Line-Averaged Heat Load, Drift-Scale Thermohydrologic Model Submodel of the Multiscale Thermohydrologic Model [Indicated as LDTH (DOE) in the Plot]

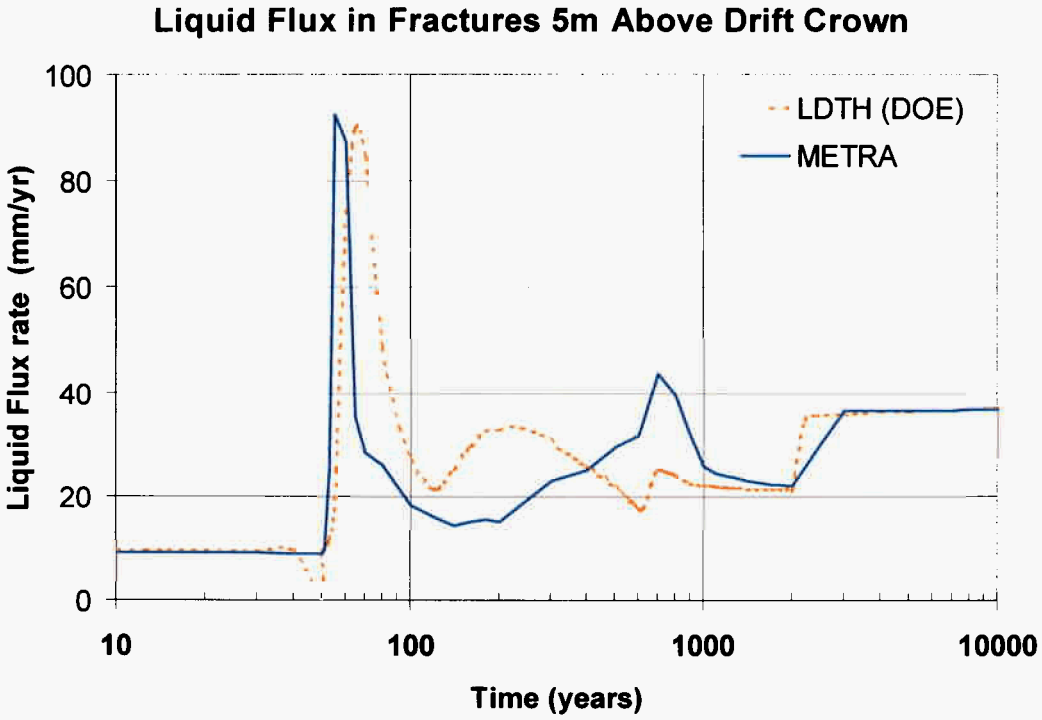

Figure 3-5. Liquid Flux in the Fracture Continuum at 5 m [16.4 ft] above the Drift Crown Simulated Using METRA Compared with Results from the Line-Averaged Heat Load, Drift-Scale Thermohydrologic Model Submodel of the Multiscale Thermohydrologic Model [Indicated as LDTH (DOE) in the Plot]
[mm = 0.039 in]

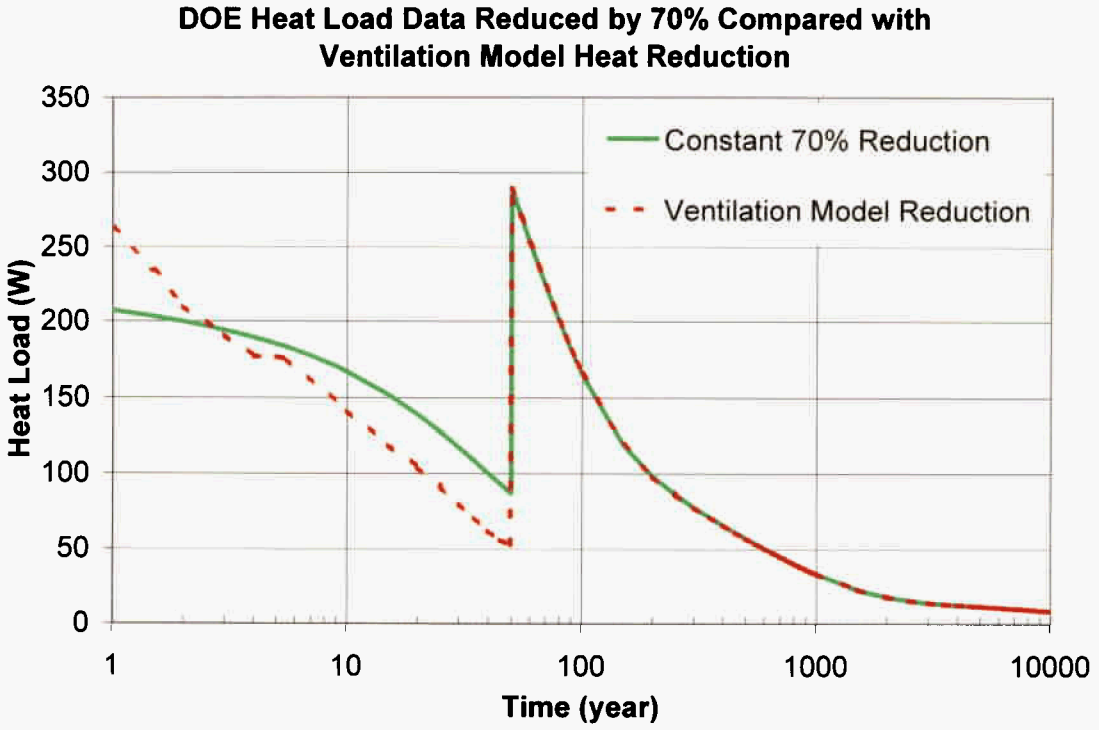

Figure 3-6. Heat Load Data Used by DOE in the Line-Averaged Heat Load, Drift-Scale Thermohydrologic Model Submodel Reduced by a Constant 70 Percent During a 50-year Preclosure Period Compared with the Same Data Reduced by Heat Removal Calculated Using the Ventilation Model. The Heat Load Used in the Model Is Half of the Actual Line-Averaged Heat Load Because of the No-Flow Boundary Through the Centerline of the Drift.

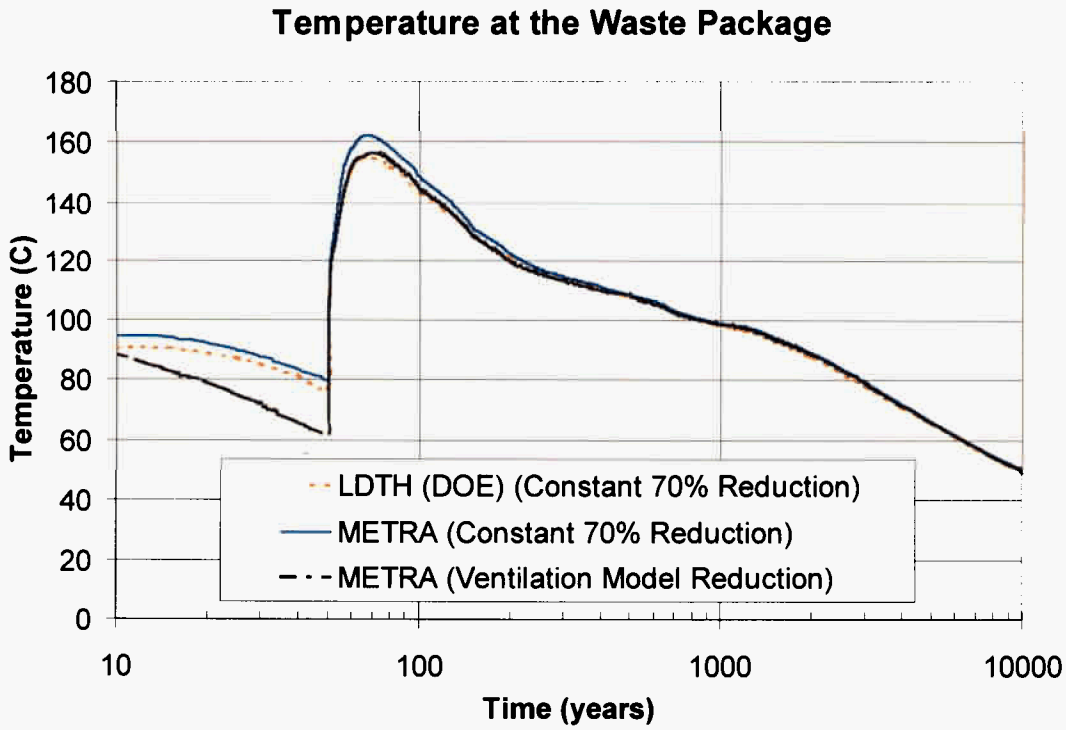

Figure 3-7. Temperature at the Waste Package Modeled Using a Constant 70-Percent Heat Reduction for Preclosure Ventilation and Using Heat Reduction Calculated from the Ventilation Model Compared to Results from the Line-Averaged Heat Load, Drift-Scale Thermohydrologic Model Submodel [Indicated as LDTH (DOE) in the Plot]. Note that the Curves Labeled as LDTH (DOE) and METRA (Constant 70-Percent Reduction) Are Identical to Those in Figure 3-3.

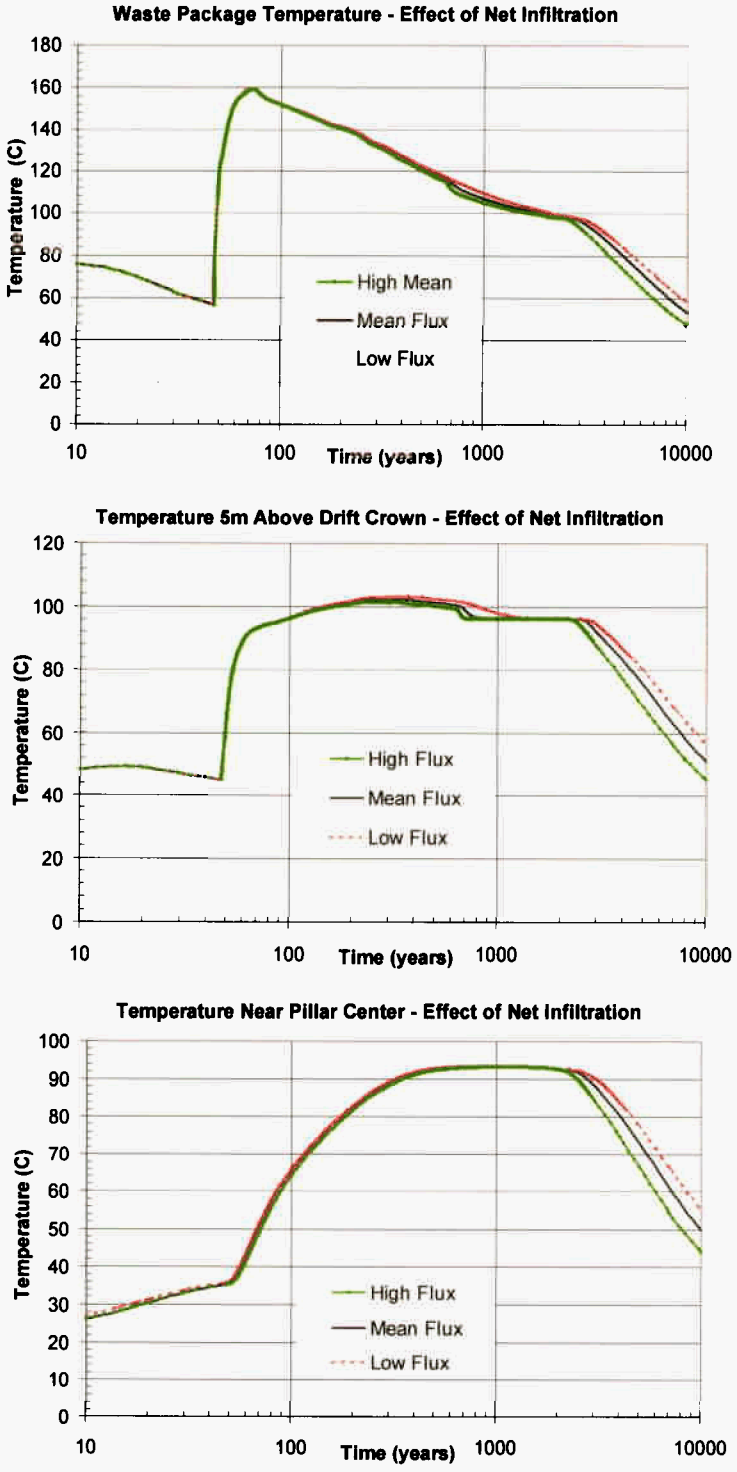

Figure 3-8. Effect of Net Infiltration on Temperatures at the Waste Package, 5 m [16.4 ft] above the Drift Crown, and Near the Pillar Center Is Shown as a Function of Time. Infiltration Rates for Mean, High, and Low Fluxes Are Given in Table 3-1.

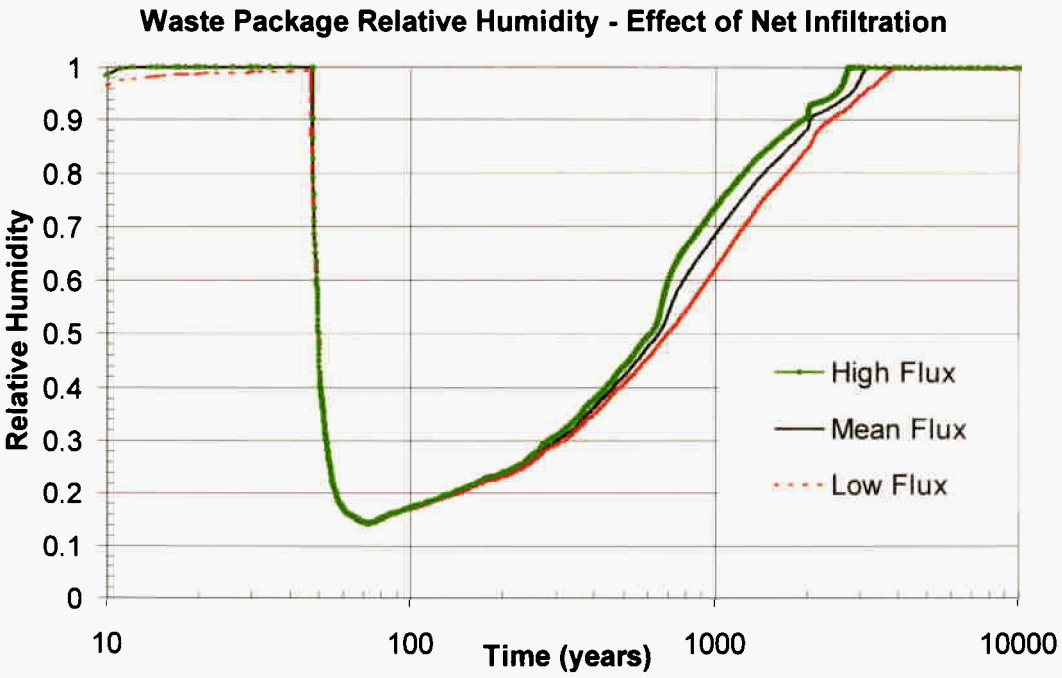

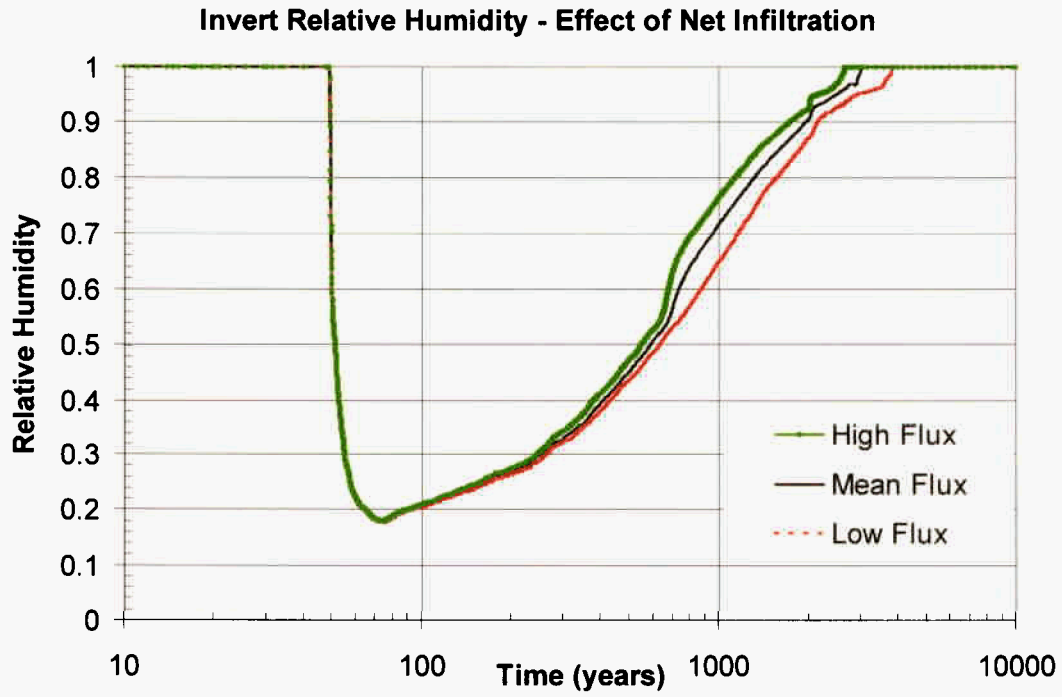

Figure 3-9. Effect of Net Infiltration on Relative Humidity at the Waste Package and Invert Is Shown as a Function of Time. Infiltration Rates for Mean, High, and Low Fluxes Are Given in Table 3-1.

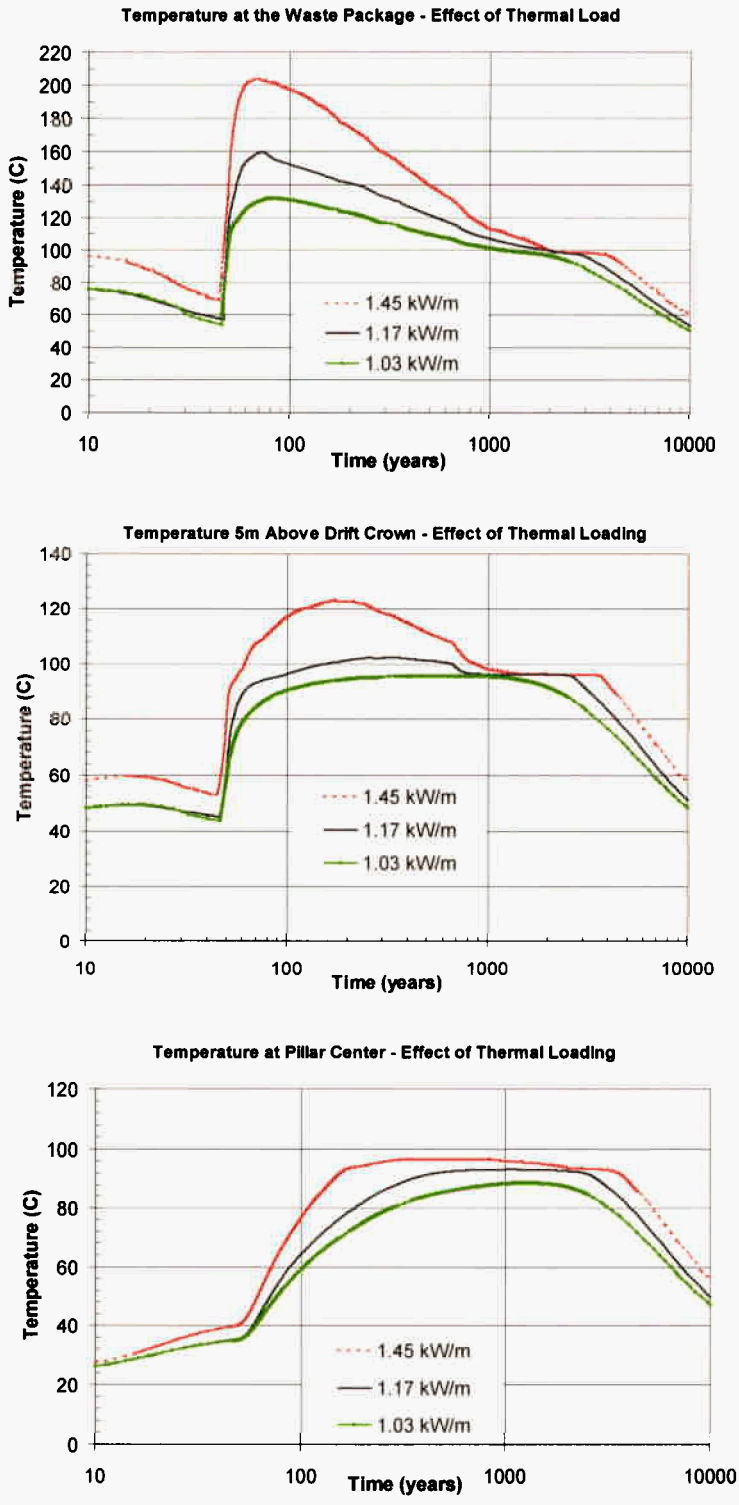

Figure 3-10. Effect of Thermal Loading on Temperatures at the Waste Package, 5 m [16.4 ft] Above the Drift Crown, and Near the Pillar Center

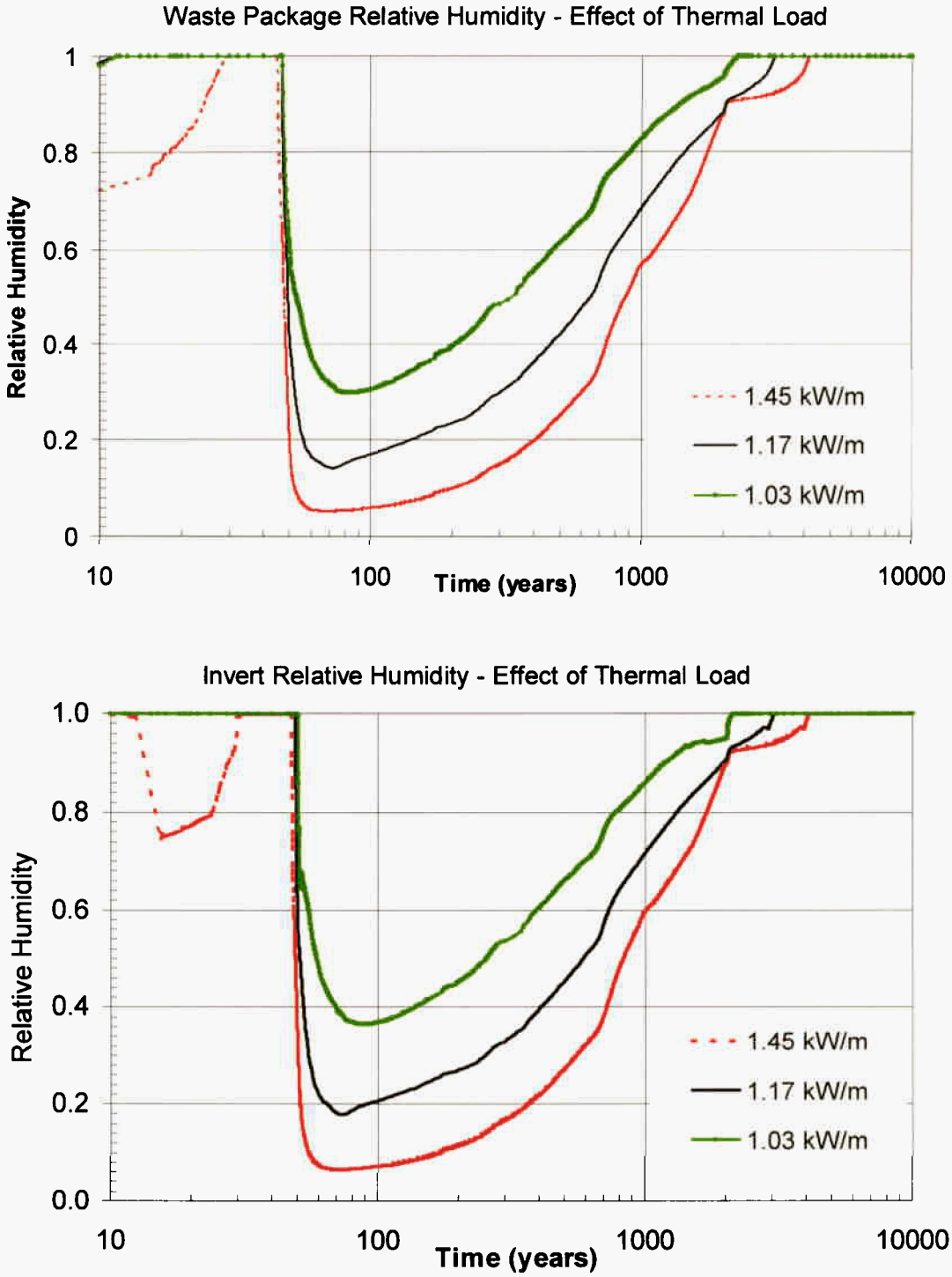

Figure 3-11. Effect of Thermal Loading on Relative Humidity at the Waste Package and Invert

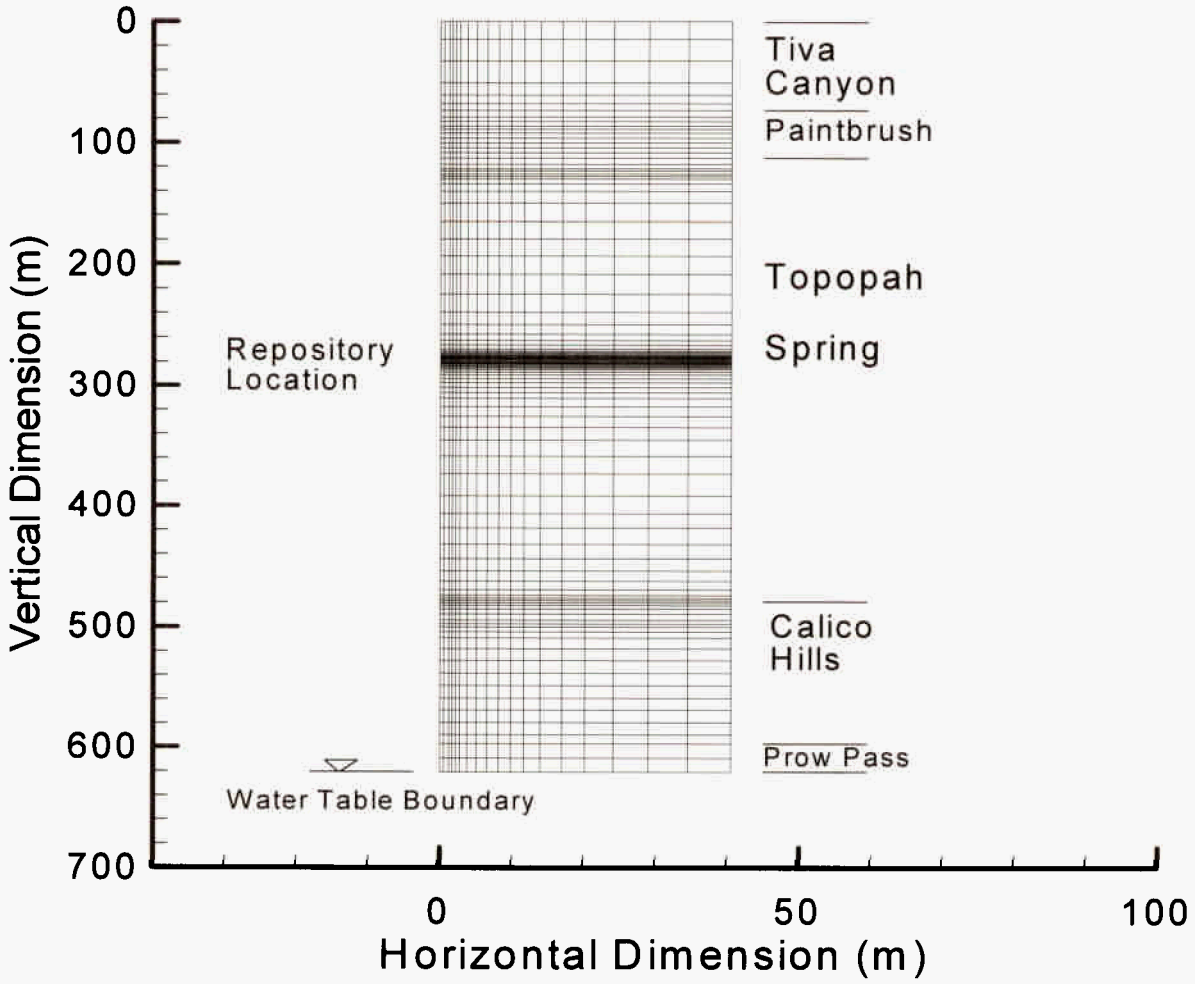

Figure 3-12. Domain and Numerical Mesh Used for the Thermohydrologic Model at the Central Repository Location Labeled l4c1. Major Hydrostratigraphic Formations and Approximate Repository Location Are Indicated. [m = 3.28 ft]

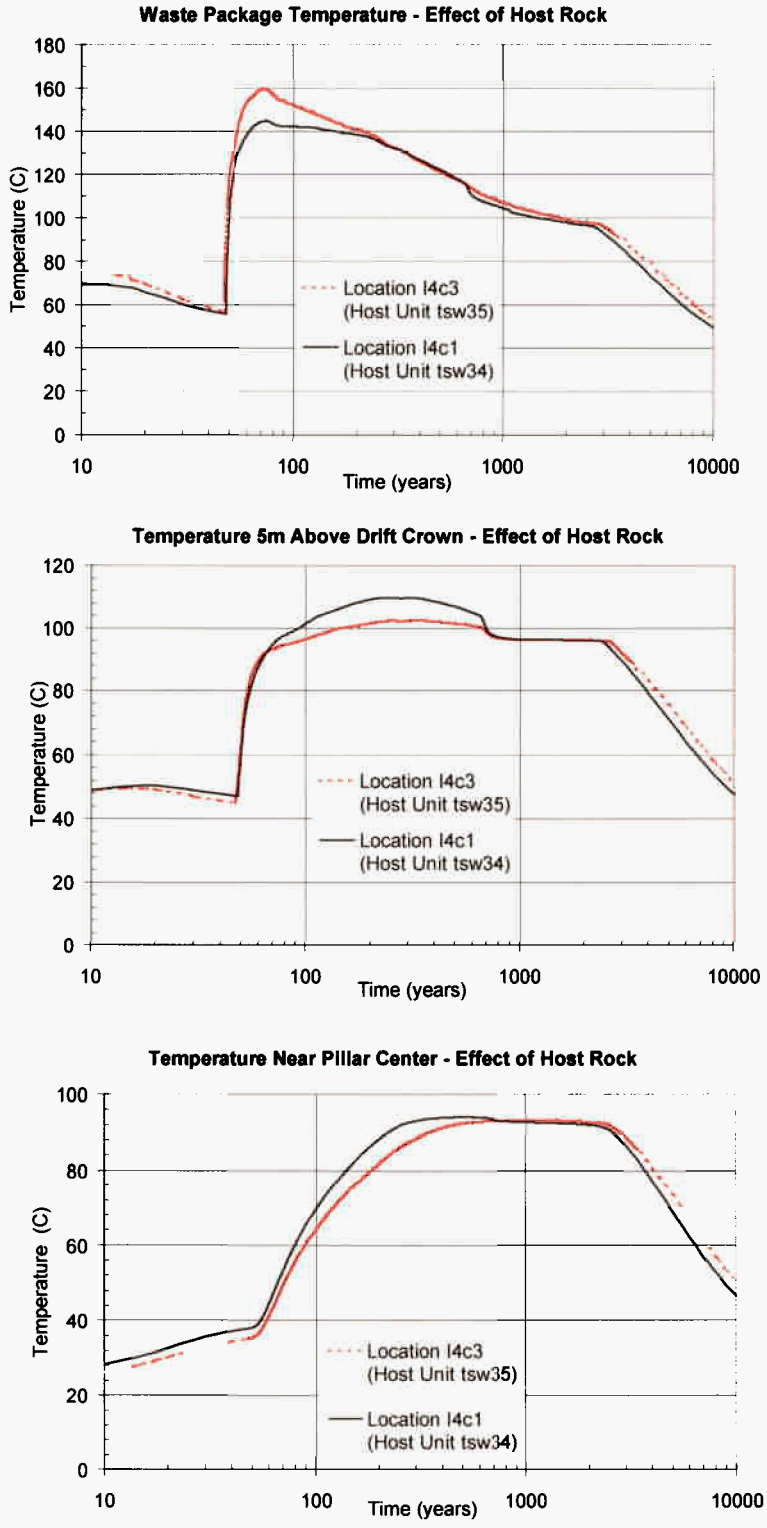

Figure 3-13. Temperatures at the Waste Package, 5 m [16.4 ft] Above the Drift Crown, and Near the Pillar Center Showing the Effects of Hydrostratigraphy and Repository Host

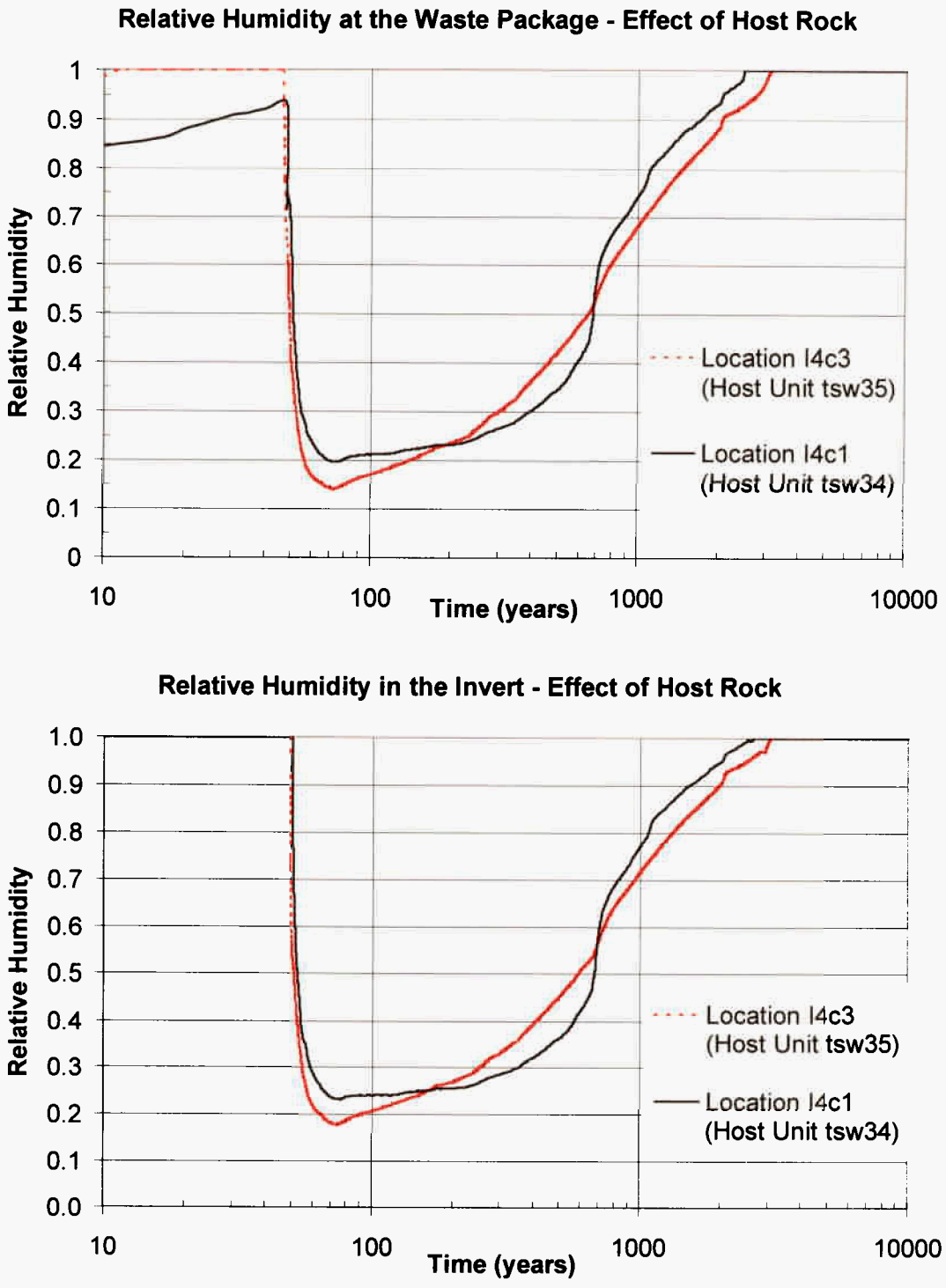

Figure 3-14. Effect of Hydrostratigraphy and Repository Host Rock on Relative Humidity at the Waste Package and Invert

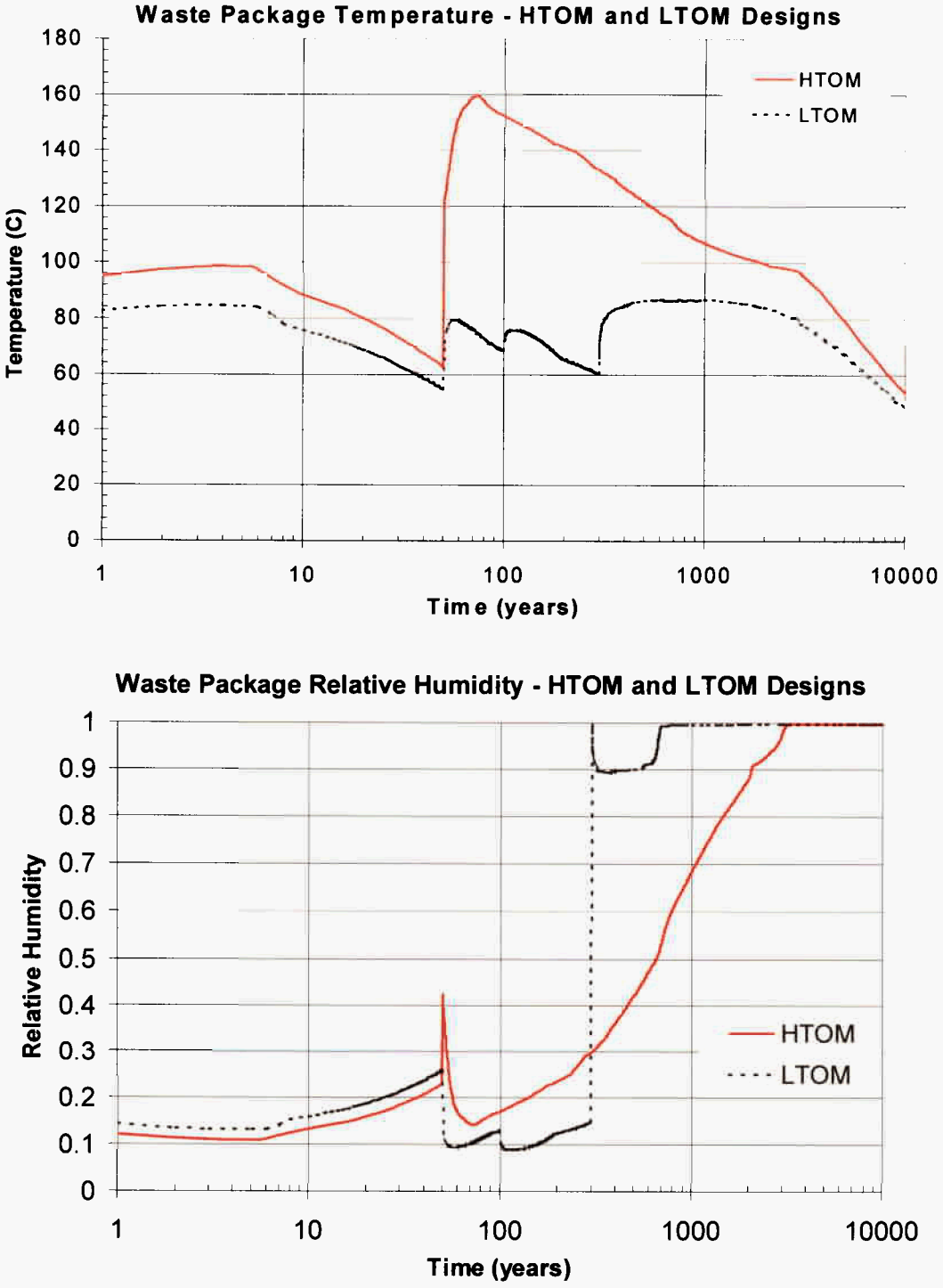

Figure 3-15. Temperature and Relative Humidity at the Waste Package from the Combined Preclosure and Postclosure Models for the High-Temperature Operating Mode (Indicated as HTOM on the Plot) and Low-Temperature Operating Mode (Indicated as LTOM on the Plot) Repository Designs

4 CROSS DRIFT THERMAL TEST MODEL

4.1 DOE Approach

The Cross Drift Thermal Test is to be conducted in the Enhanced Characterization of the Repository Block drift. Heating is planned to begin in January 2003 and end in October 2003.[1] A motivation for conducting the Cross Drift Thermal Test is to develop thermohydrologic data for the lower lithophysal unit of the Topopah Spring Tuff (hydrostratigraphic unit tsw35), the unit hosting most of the repository. Previous thermal tests, including the Large Block Test, Single Heater Test, and the Drift Scale Test, were all conducted in the middle nonlithophysal unit of the Topopah Spring Tuff (hydrostratigraphic unit tsw34). The lower lithophysal unit of the Topopah Spring Tuff has large {as large as 75 cm [29.5 in] in diameter} lithophysal cavities and a different fracture pattern than the middle nonlithophysal unit of the Topopah Spring Tuff that may affect its thermohydrologic behavior. The Cross Drift Thermal Test, as currently designed, is more representative of the high temperature repository. In addition to the general objective of a better understanding of heat-driven coupled processes in the proposed repository host rock, the Cross Drift Thermal Test has specific objectives to investigate assumptions about condensate drainage in fractures. As stated in CRWMS M&O (2000h) these specific objectives are

- To test or investigate the premise that heat-mobilized pore water will shed/drain between emplacement drifts to below the repository horizon
- To test or investigate the premise that liquid water can penetrate through zones/regions at or above boiling temperature
- To test or investigate the premise that there would be no long-term seepage into the emplacement drifts and that the chemistry of seepage water, if any, will be benign to the engineered components

The planning report (CRWMS M&O, 2000h) does not state explicitly how data from the test will be used to either reject or accept these hypotheses but does describe in general how the test will be conducted. The heating period of the test is planned for a duration of 9 months. At approximately 7.5 months into the heating period, after the boiling and the expected dryout zones have developed, water will be released from a borehole approximately 1.75 m [5.74 ft] above the plane of the heaters. Tracking of the released water as it drains through fractures will be attempted by geophysical methods and temperature sensors. Water draining below the heater plane may collect in boreholes constructed for that purpose about 2 m [6.56 ft] below the heater plane.

4.2 Scope and Purpose of This Modeling Study

The Drift Scale Test was designed with wingheaters to approximate a planar heat source and create a significant zone of condensate refluxing above the drift (Buscheck and Nitao, 1996). A significant zone of refluxing was thought to be necessary for acquiring data on coupled

[1]Hughson, D.L. "Trip Report (Las Vegas): Twelfth Thermal Workshop." San Antonio, Texas: CNWRA. 2001.

thermohydrologic processes and to test the hypothesis that refluxing water would penetrate the zone of dryout and enter the drift. Unfortunately, as documented in a white paper on losses through the Drift Scale Test bulkhead (CRWMS M&O, 2001c), approximately two-thirds of the pore water vaporized by the test escaped through the bulkhead and into the ventilation system of the Exploratory Studies Facility. CNWRA staff have commented that these losses diminish the utility of the Drift Scale Test for testing the hypothesis that reflux will not enter the drift while temperatures are above boiling (Hughson and Green, 2001). Uncertainty in the effects of losses through the Drift Scale Test bulkhead places greater importance on the Cross Drift Thermal Test to resolve questions about liquid water flow through superheated fractured rock.

CNWRA comments on the Cross Drift Thermal Test plan (Hughson, et al., 2001) identified two potentially important aspects of the Cross Drift Thermal Test, not taken into account by the DOE in the planning report, that could significantly influence liquid water flow in fractures and collection of water in small-diameter boreholes. One aspect is spatial heterogeneity in permeability of the fracture network. Permeability data obtained by air-injection testing in niches and alcoves in the Exploratory Studies Facility varied over 4 to 5 orders of magnitude (Wang, et al., 1999), but thermohydrologic models of the Drift Scale Test and pretest predictions of the Cross Drift Thermal Test assume a homogeneous fracture continuum (CRWMS M&O, 2000h,i). A second aspect is the capillary barrier to unsaturated seepage formed by the presence of a void space. The threshold of background unsaturated flux at which water first begins to drip into a horizontal, cylindrical opening is a function of permeability, capillary retention, and diameter of the opening (Philip, et al., 1989). Homogeneous porous media properties used for the preliminary scoping calculations of the Cross Drift Thermal Test are fracture permeability of 1.29×10^{-12} m^2 capillary retention van Genuchten alpha parameter of 7.39×10^{-4} Pa^{-1} (CRWMS M&O, 2000h). For a borehole 10 cm [3.9 in] in diameter, assuming equivalence between the van Genuchten and Gardner alpha parameters, these properties give a seepage threshold for the water collection boreholes in the Cross Drift Thermal Test of 274,827 mm/yr [10,819.94 in/yr] (Philip, et al., 1989). Thus, actual collection of water in the water collection boreholes in the Cross Drift Thermal Test will depend on small-scale heterogeneity in fracture properties.

CNWRA comments on the Cross Drift Thermal Test plan (Hughson, et al., 2001) made two recommendations regarding fracture property heterogeneity and water collection boreholes in the Cross Drift Thermal Test. CNWRA recommended that the DOE should

- Consider designing openings for collection of thermally mobilized and injected water as slots rather than cylindrical boreholes, and

- Consider evaluating fracture heterogeneity in thermohydrologic modeling of the Cross Drift Thermal Test.

The purpose of the modeling study presented here is to evaluate the effect of fracture heterogeneity on thermohydrologic behavior in the Cross Drift Thermal Test and provide technical bases for reviewing the DOE use of data collected from the Cross Drift Thermal Test.

4.3 Design of the Cross Drift Thermal Test Modeling Study

The Cross Drift Thermal Test will be constructed in an alcove at station 16+95 in the Enhanced Characterization of the Repository Block beginning December 2001.[2] A plan view of the Cross Drift Thermal Test thermal alcove and test block is shown in Figure 4-1, and cross sections are shown in Figure 4-2 (CRWMS M&O, 2000h). Boreholes numbered #1, #2, #3, #4, and #5 in Figures 4-1 and 4-2 are the heaters, and boreholes numbered #6, #7, and #8 are for water collection.

4.3.1 Model Domain and Boundary Conditions

The Thermal Alcove, Injection Alcove, and the Cross Drift, as shown in plan view on Figure 4-1, form three natural boundaries of the Cross Drift Thermal Test test block. These were implemented as Dirchlet-type boundaries with gas pressure prescribed as a constant 85,000 Pa [12.33 psi], temperature prescribed as a constant 25 °C [77 °F], and saturation prescribed as a constant of 99-percent gas. For convenience in grid construction, the Cross Drift Thermal Test Thermal Alcove modeled boundary extends straight from the Injection Alcove to the Cross Drift, omitting the dogleg of the Cross Drift Thermal Test Thermal Alcove drift. No natural boundary exists for the fourth wall of the modeled test block, so this boundary was treated as an impermeable wall, located 5 m [16.4 ft] beyond the end of the heater boreholes, and the Injection Alcove boundary was extended beyond the end of the Alcove to complete the modeled domain. The top of the modeled test block was set 7.5 m [24.6 ft] above the centerline of the heater boreholes as a Cauchy-type boundary condition with gas pressure prescribed as a constant 85,000 Pa [12.33 psi], temperature prescribed as a constant 25 °C [77 °F], and water flux prescribed as a constant 3.3 mm/yr [0.13 in/yr]. The bottom of the test block was set 5 m [16.4 ft] below the plane of the heater holes as a Dirchlet-type boundary with gas pressure prescribed as a constant 85,000 Pa [12.33 psi] and temperature prescribed as a constant 25 °C [77 °F]. Gas saturation at the bottom boundary was prescribed as 0.0575 for the matrix and 0.9369 for the fractures. Dirchlet type boundary conditions prescribed on three walls of the test block were taken to be uniform from the top of the test block to the bottom even though the alcoves are only about 5 m [16.4 ft] in diameter, and the modeled z-dimension is 12.5 m [41.0 ft].

Total dimensions of the modeled block are 25.5 m [83.7 ft] in the x-direction (parallel to the Thermal Alcove face), 15 m [49.2 ft] in the y-direction (parallel to the Injection Alcove face) and 12.5 m [41.0 ft] in the z-direction. The numerical grid constructed for METRA simulations is shown in Figures 4-3 and 4-4. Figure 4-3 shows a plan view of a horizontal cross section through the plane of the heater boreholes where x = 0 m [0 ft] is the Injection Alcove, and y = 15 m [49.2 ft] is the Thermal Alcove. Figure 4-4 shows a vertical cross section through the midpoint of the heaters at y = 7.5 m [24.6 ft]. The bottom Dirchlet-type boundary conditions result in a capillary rise, as shown by the saturation contours along the bottom {z = 12.5 m [41.0 ft]} of the grid in Figure 4-4. This capillary rise is well below the collection boreholes and has no other effect on the model results. Temperature contours in Figure 4-3, representing 9 months of heating using homogeneous properties, are shown to mark the location of the heaters. Heat was applied uniformly at a rate of 290 W/m in the heater borehole model

[2]Hughson, D.L. "Trip Report (Las Vegas): Twelfth Thermal Workshop." San Antonio, Texas: CNWRA. 2001.

elements for 9 months. The filled temperature contours superposed onto the numerical grid do not extend to the boundaries of the grid because METRA implements an integrated finite volume numerical scheme where variables are calculated at the nodes, which are at the center of each block in this numerical grid. The graphical plotting package used for contouring does not extrapolate beyond the spatial extent of the data, so the dimensions of the displayed numerical results are smaller, by half a grid block, than the actual modeled domain. Contours of fracture saturation at 1 month of heating using homogeneous properties are overlaid on the numerical grid in Figure 4-4. The locations of the heaters are identified in this figure by the small zones of dryout. The three water collection boreholes can be identified in Figure 4-4 by caps of higher saturation over blocks of low saturation. The blocks of low saturation are the actual water collection boreholes implemented in the model by fixing capillary pressure at zero for all saturations. The zones of higher saturation capping the water collection boreholes form as a result of a capillary barrier created by the zero capillary pressure.

4.3.2 Model Parameters

The Cross Drift Thermal Test model consisted of two interacting continua separately representing a matrix and a fracture porous medium. The fracture and matrix continua in this model interacted through a modification of the Active Fracture Model (Liu, et al., 1998). Functions for saturation-dependent capillary pressure and relative permeability were implemented according to the Active Fracture Model, but fracture–matrix interaction was restricted by a constant factor for near ambient conditions. This is the same approach that was used for repository-scale modeling described in Chapter 3. This modification had the effect of restricting matrix imbibition at elevated saturations, forcing more condensate drainage to flow in the fracture continuum. Effective mean parameters for the lower lithophysal unit (hydrostratigraphic unit tsw35) are given in Appendix C. Heterogeneity was represented in the fracture continuum as a lognormal gaussian random field of variance 1.0 with an anisotropic exponential covariance of 2-m [6.56-ft] range in the horizontal and 10-m [52.8-ft] range in the vertical directions. All other properties were taken to be homogeneous. Two realizations were created using the spectral method (Gutjahr, et al., 1994) and assigned to model elements without scaling to element volume.

4.4 Cross Drift Thermal Test Model Results

Figure 4-5 shows fracture saturation for uniform model properties after 9 months of heating. Dark blue zones in Figure 4-5 show dryout zones around the heater boreholes. Dark blue zones on the sides of the test block in Figure 4-5 were caused by the boundary conditions of the open drifts. Elevated saturations above the water collection boreholes were a result of the capillary barrier effect. Figure 4-6 shows fracture saturation for one of the realizations of heterogeneous fracture permeability after 9 months of heating. Zones of vertically oriented high fracture permeability resulted in preferential dryout above the left-most heaters, and a zone of preferential flow occurred between the left-most and center heaters. In the actual test, zones of preferential dryout may be suppressed by injection of water from Borehole #16 (shown in Figure 4-1).

Condensate drainage water was unable to break the capillary barrier of the collection boreholes both for uniform and for heterogeneous fracture permeability. Fracture flux did not exceed the seepage threshold of the 1-m [3.28-ft] wide collection boreholes despite weakening of the

capillary barrier by use of a 0.15 m [0.49 ft] vertical connection between the elements representing the collection boreholes and the fracture continuum above. Even though flux of liquid water did not enter the collection boreholes, saturation of water in the collection boreholes did steadily increase with time. Close inspection of flux vectors between elements representing the collection boreholes and the fracture continuum showed liquid water slowly leaving the collection boreholes and air saturated with water vapor entering. The conclusion is that water vapor entered the collection borehole elements through gas convection created by the heater elements. Water vapor condensed to liquid inside the collection boreholes and was drawn into the fracture continuum by capillary suction. Figure 4-7 shows the volume of condensate per volume of collection borehole as a function of time for 9 months of heating and 15 months of cooling. Each of the collection boreholes in the models collected about 1 L [0.26 gal] of condensate. By scaling this to the actual physical volume of the actual collection boreholes planned to be 0.1 m [0.33 ft] in diameter, it can be predicted that approximately 0.2 L [0.05 gal] of condensate will collect in the boreholes during the course of the test.

The model prediction of water collecting in the water collection boreholes by condensation, but not by seepage, has implications for the proposed Cross Drift Thermal Test. The model used for seepage abstraction in performance assessments uses a heterogeneous fracture permeability similar to the realizations generated for this modeling study of the Cross Drift Thermal Test (CRWMS M&O, 2000j). Seepage actually entering the collection boreholes of the Cross Drift Thermal Test during the test but not seeping into the collection boreholes in a model using heterogeneous properties suggests that the seepage model for performance assessments may be nonconservative. The Seepage Model for Performance Assessments Including Drift Collapse analysis and model report (CRWMS M&O, 2000j) modeled seepage into drifts using a heterogeneous fracture continuum similar to the approach taken here for modeling condensate drainage into collection boreholes. In this model of condensate drainage into collection boreholes, no water entered the boreholes using a heterogeneous fracture continuum, but yet condensate water collected in boreholes of the Drift Scale Heater Test (CRWMS M&O, 2000i). Absence of seepage into water collection boreholes suggests that the small-scale processes controlling seepage into horizontal, cylindrical openings in fractured rock are not captured by the stochastic porous media continuum approach. However, water did enter the collection boreholes, in the Cross Drift Thermal Test model described here, by vapor transport and condensation. This cold-trap effect may be a mechanism for significant amounts of water to enter drifts in a repository. Also, if water vapor condenses in the collection boreholes during the Cross Drift Thermal Test, it could dilute water samples collected for chemical analyses. Water samples diluted by condensate would not accurately represent the actual chemistry of seepage water.

4.5 Summary of Cross Drift Thermal Test Model Results

A three-dimensional model of the planned Cross Drift Thermal Test was implemented with uniform and heterogeneous fracture permeabilities to evaluate the effects of heterogeneity on the distribution of thermally mobilized water and to see if condensate drainage would seep into the proposed water collection boreholes. Condensate drainage did not exceed the seepage threshold of the collection boreholes for either the model using homogeneous fracture permeability or the model using heterogeneous fracture permeability. Water vapor, however, entered the collection boreholes through gas convection cells created by heating and condensation accumulated in the boreholes, leveling off between approximately 2 and 2.5 L [0.52 and 0.66 gal] per cubic meter of borehole after approximately 10 months. These results

suggest that seepage into collection boreholes could be compared to results from the seepage model for performance assessments and that condensation in the collection boreholes could possibly dilute water samples collected for chemical analyses.

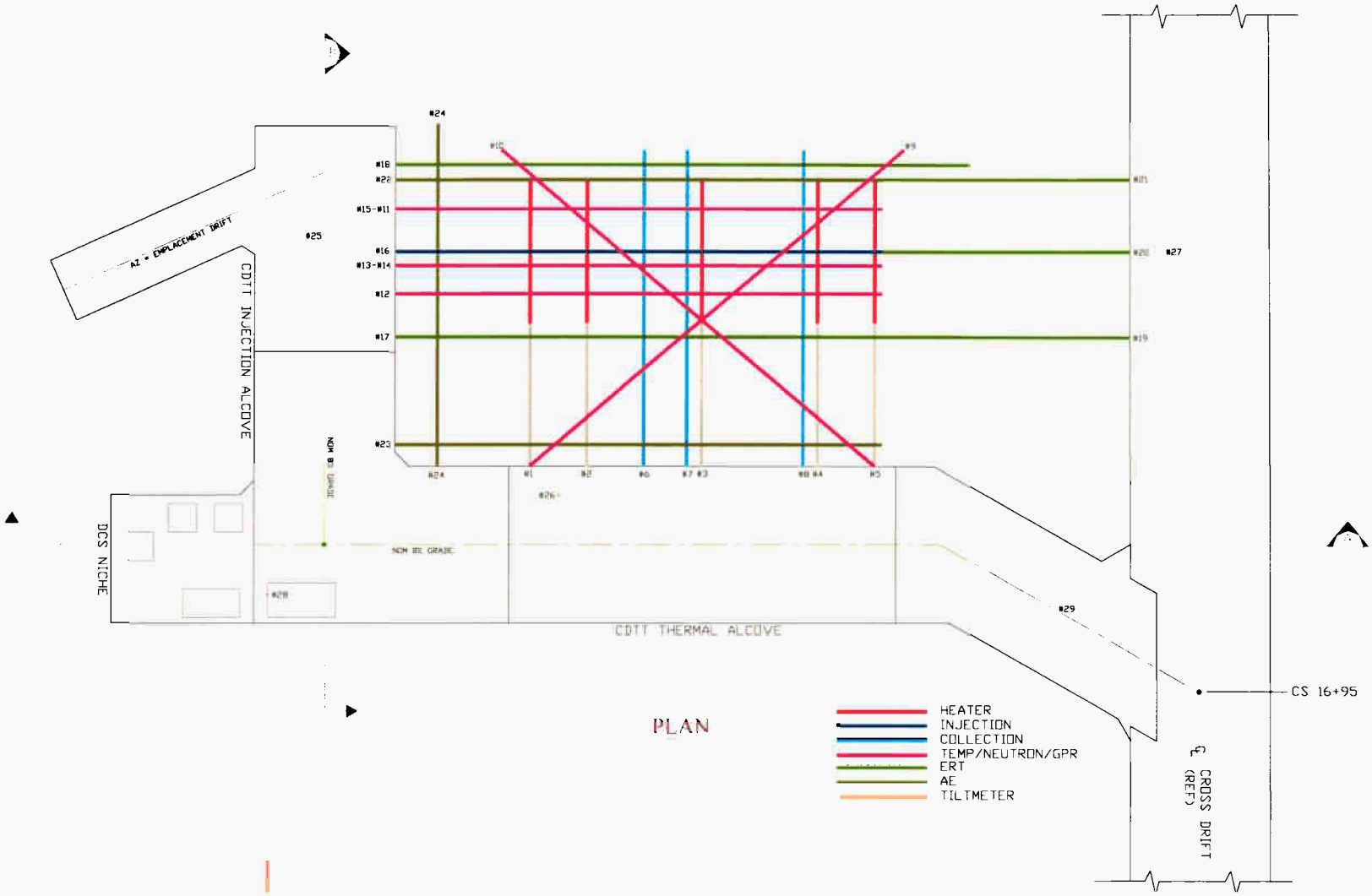

Figure 4-1. Plan View of the Cross Drift Thermal Test Alcove from the Cross Drift Thermal Test Planning Report (CRWMS M&O, 2000h). The Cross Drift and Thermal Alcove Are Approximately 5 m [16.4 ft] in Diameter.

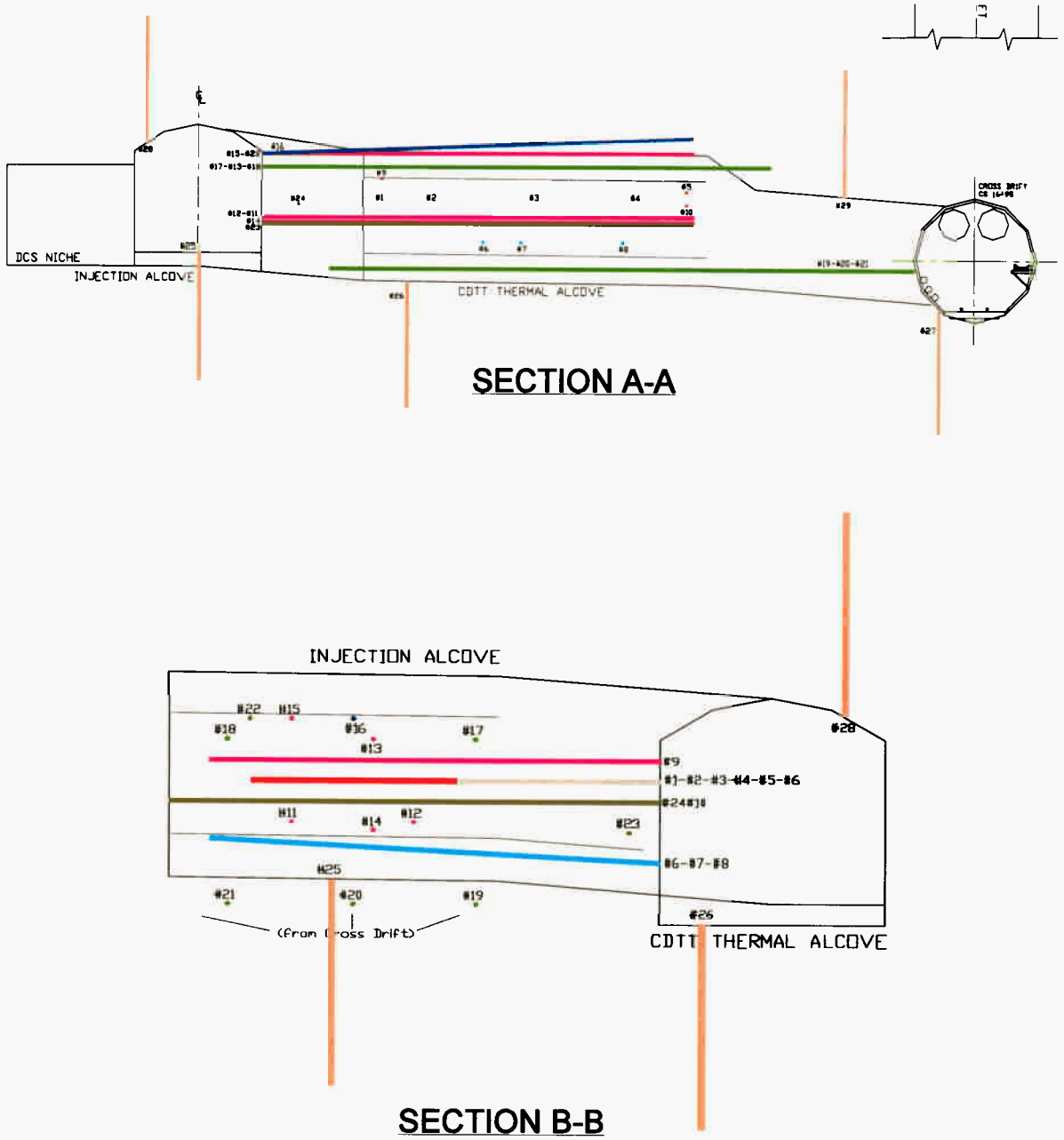

Figure 4-2. Cross Sections Parallel to the Axes of the Thermal Alcove (Top) and Injection Alcove (Bottom) from the Cross Drift Thermal Test Planning Report (CRWMS M&O, 2000h). The Cross Drift and Thermal Alcove Are Approximately 5 m [16.4 ft] in Diameter.

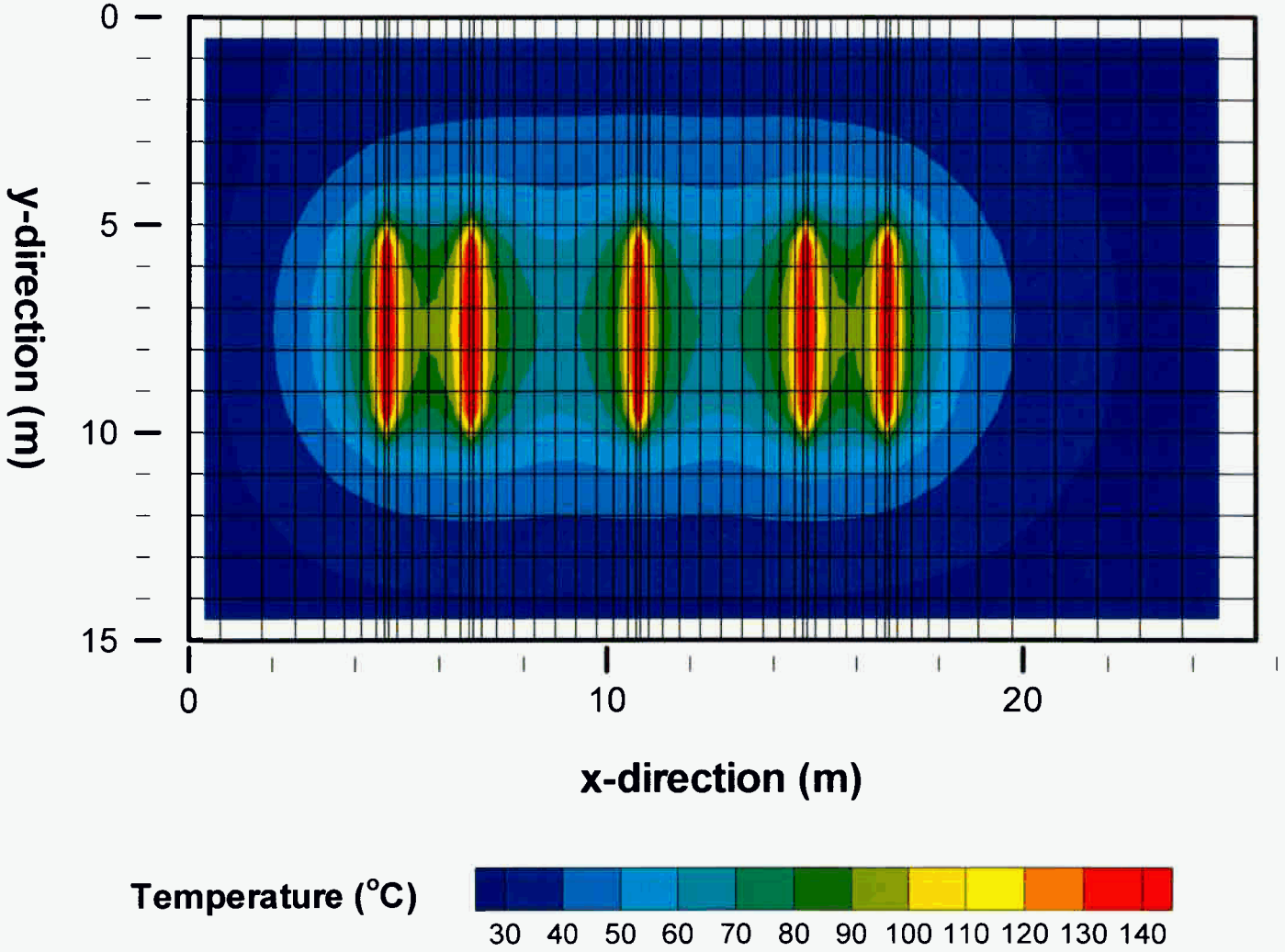

Figure 4-3. Plan View of a Horizontal Cross Section Through the Plane of the Heater Boreholes Showing the Numerical Grid Used for the Simulations as Dark Lines Outlining Grid Elements. Temperature Contours Are Shown for 9 Months of Heating. Heating Elements, Outlined by the 130 °C [266 °F] Contour Interval, Range from y = 5–10 m Centered at x = 4.75, 6.75, 10.75, 14.75, and 16.75 m. [m = 3.28 ft]

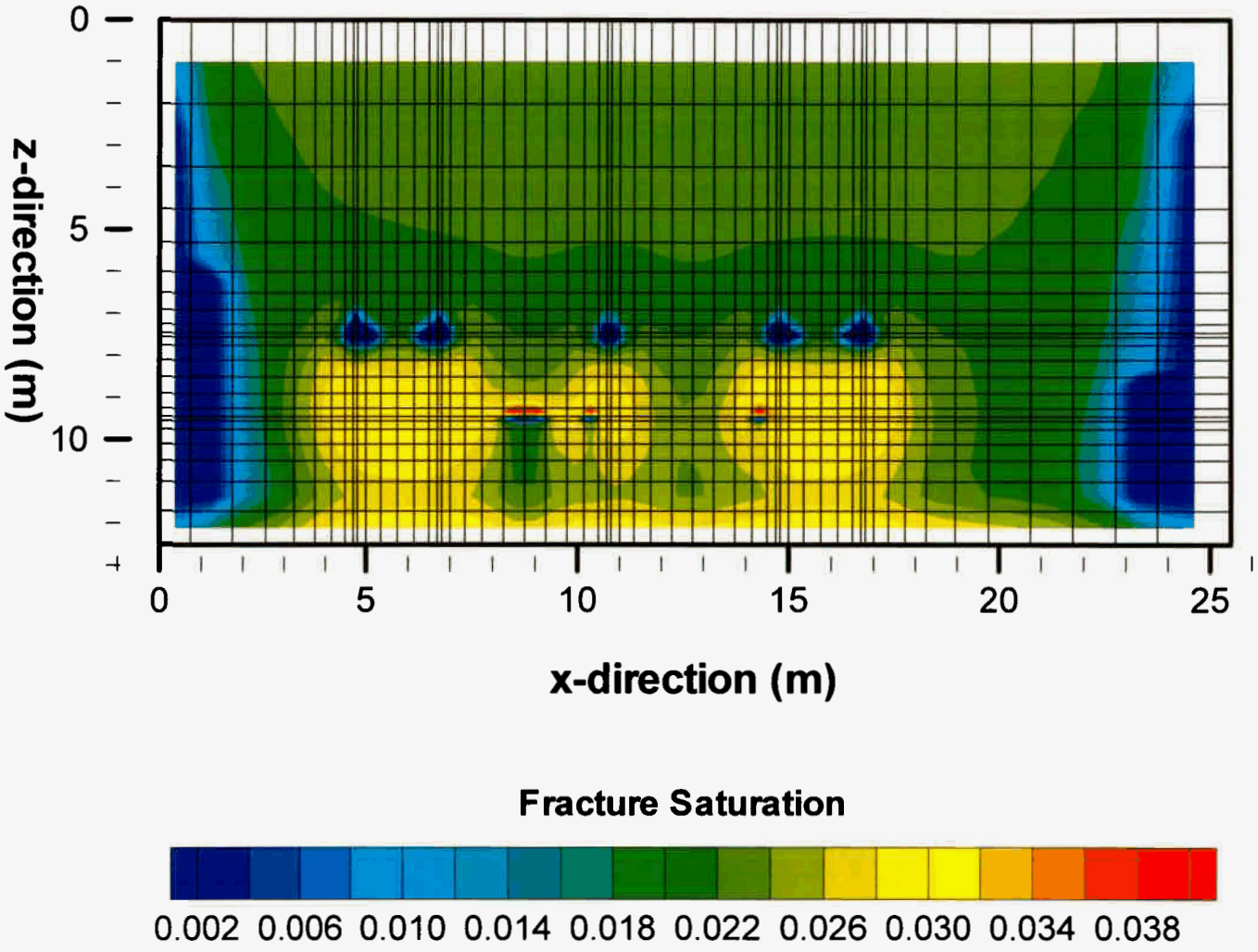

Figure 4-4. Vertical Cross-Section Through the Midpoint of the Heater Boreholes at y = 7.5 m] Showing the Numerical Grid Used for the Simulations as Dark Lines Outlining Grid Elements. Contours of Saturation in Fractures Are Shown for One Month of Heating. Heater Element Boreholes Are Outlined by the 0.006 Contour Interval Centered at z = 7.5 m and x = 4.75, 6.75, 10.75, 14.75, and 16.75 m. Water Collection Boreholes, Outlined by the 0.006 Contour Interval Immediately Below the 0.038 Contour Interval, Are Centered at z = 9.5 m and x = 8.75, 10.325, and 14.325 m. [m = 3.28 ft]

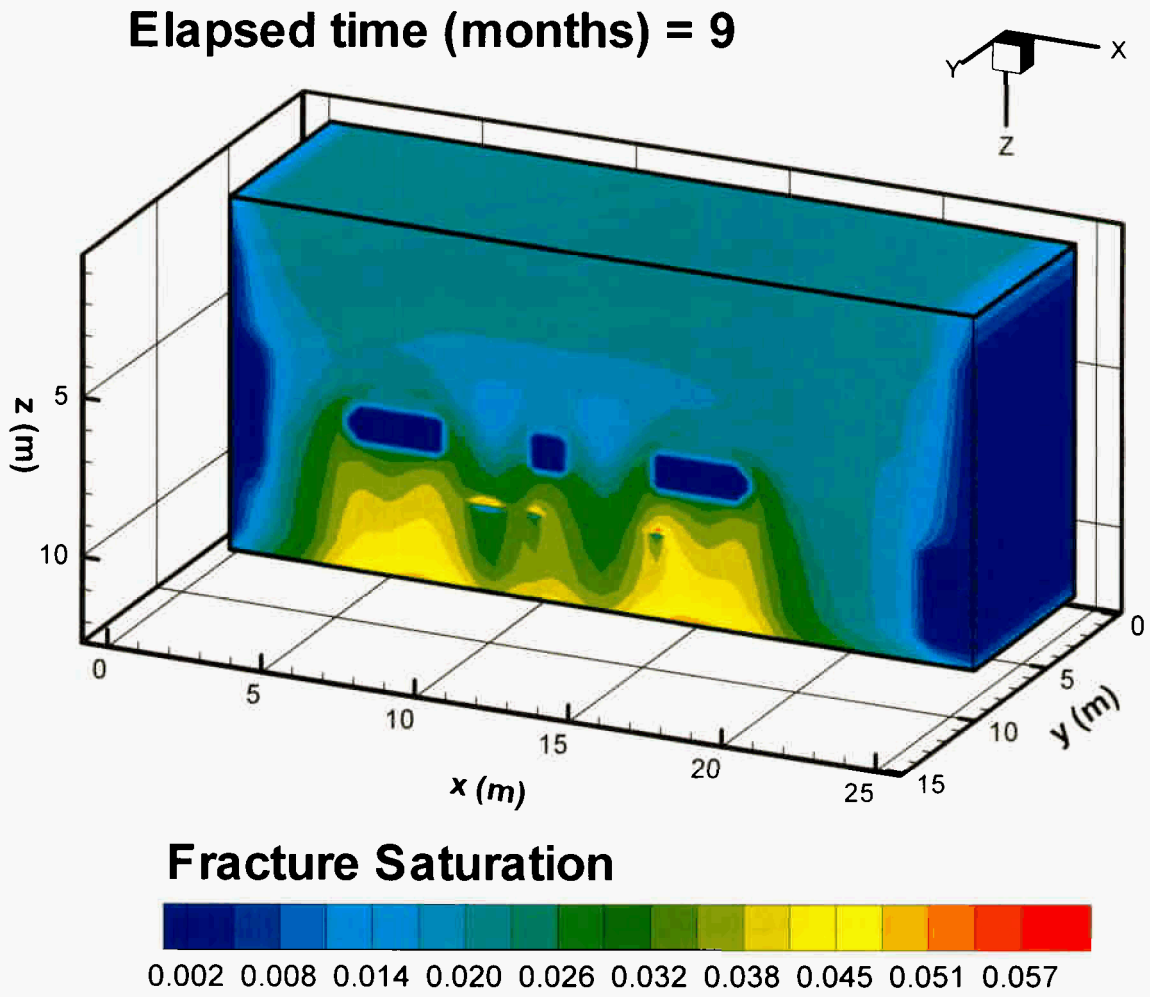

Figure 4-5. Fracture Saturation after 9 Months of Heating for Uniform, Homogeneous Properties [m = 3.28 ft]

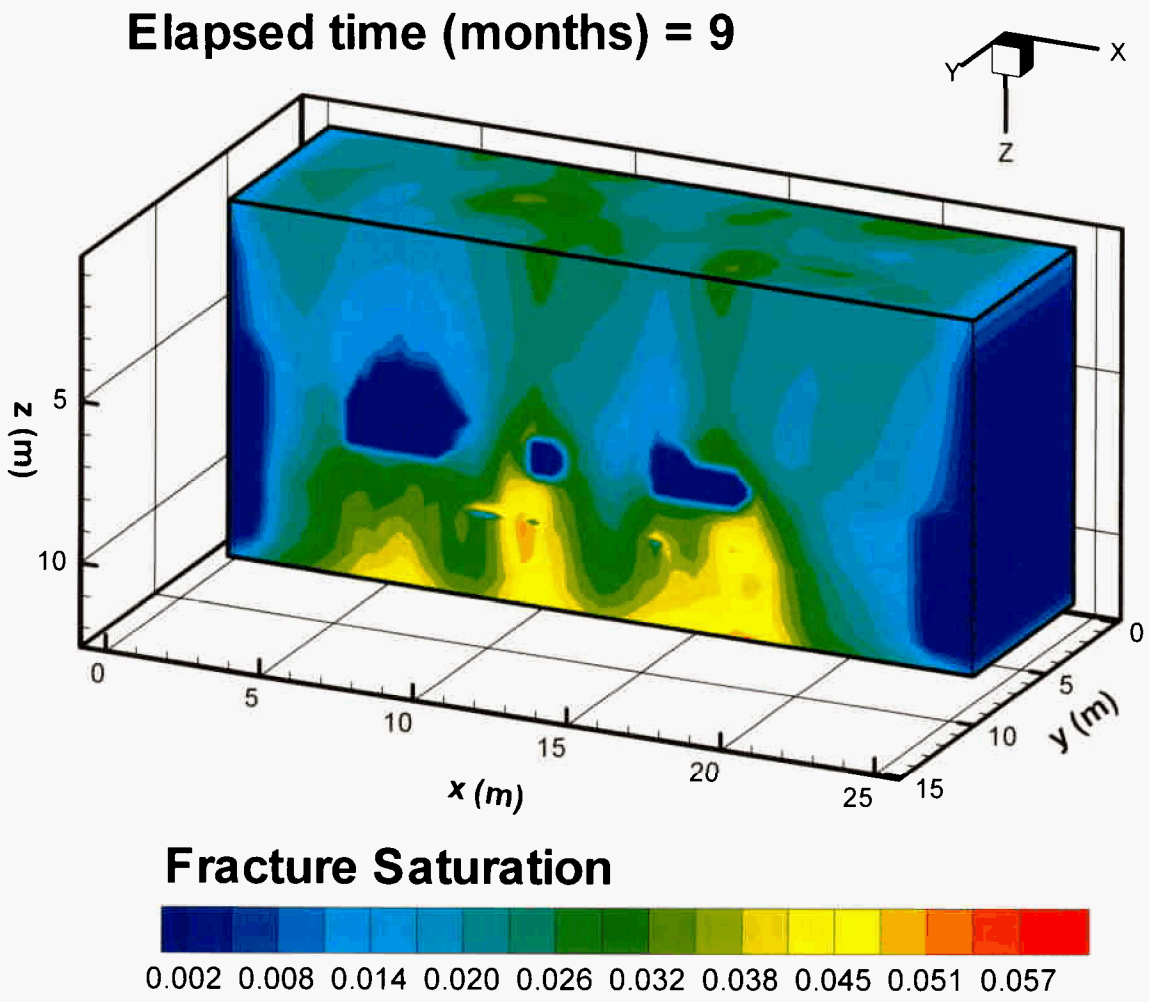

Figure 4-6. Fracture Saturation after 9 Months of Heating for a Realization of Heterogeneous Fracture Permeability [m = 3.28 ft]

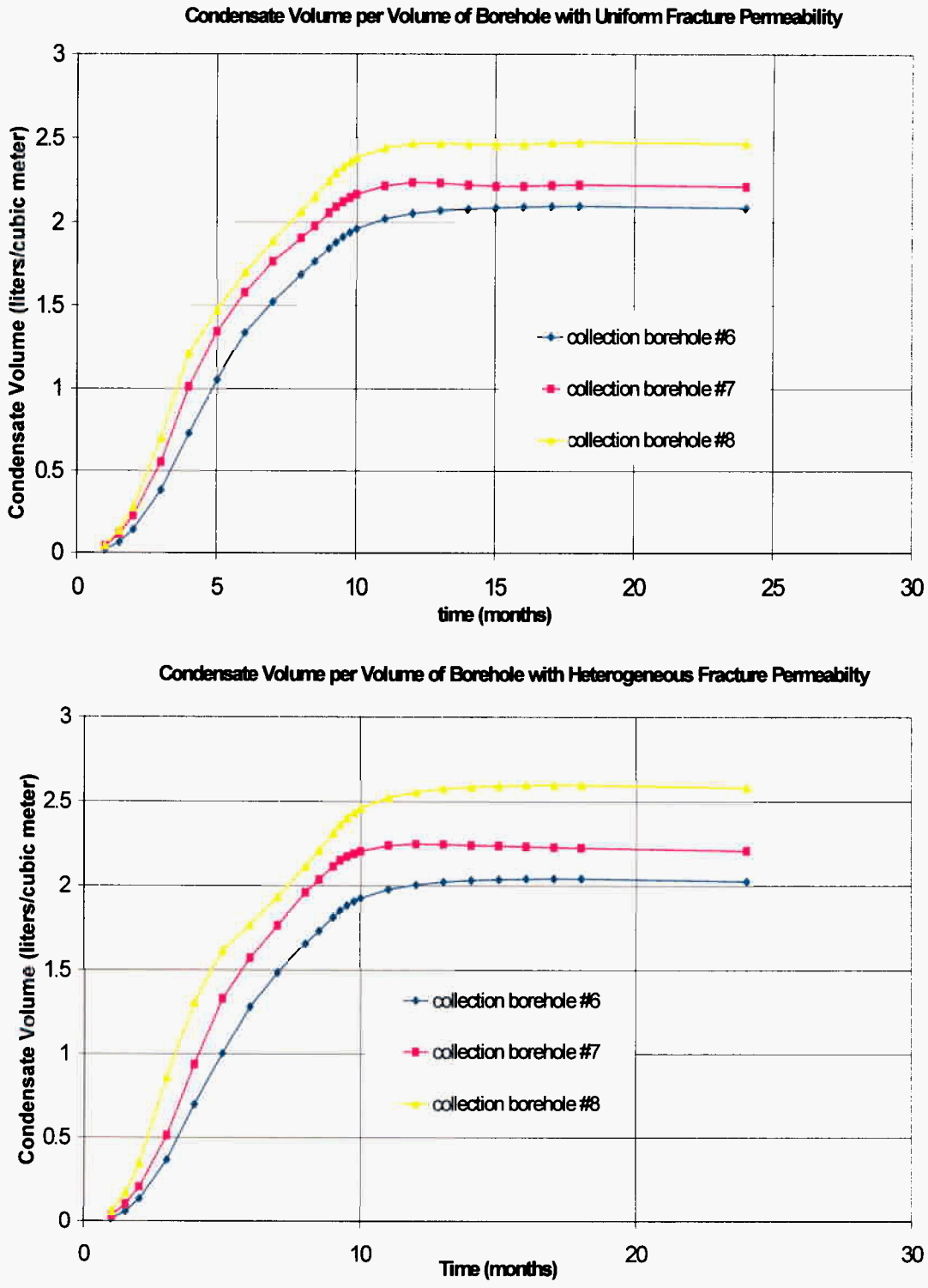

Figure 4-7. Volume of Condensate in Collection Boreholes, Normalized by Borehole Volume, for 9 Months of Heating Followed by 15 Months of Cooling. Model Results Using Homogeneous Fracture Permeability Are Given in the Top Graph and Results Obtained with Heterogeneous Fracture Permeability Are Given in the Bottom Graph.

5 CONCLUSION

Major results of the ventilation model for conditions inside drifts during the preclosure period are that ventilation at a flow rate of 15 m^3/s [529 cfs] for 50 years removed 77 percent of the heat at the inlet and 89 percent of the heat at the outlet ends of drifts. During ventilation, a temperature gradient developed where temperature at the outlet end was about 20 °C [68 °F] hotter than the inlet. Sensitivity analyses indicate that moisture removal has little effect on heat removal by ventilation. This lack of effect is because ventilation causes drying of fractures around the drift, reducing permeability to the liquid phase, and thus after a short period of ventilation, very little moisture is available for removal by ventilation air. This ventilation model was used to develop heat reduction factors that were then used by the postclosure repository-scale model to account for preclosure heat removal by ventilation.

The repository-scale model was developed using hydrostratigraphy and model properties obtained from the Multiscale Thermohydrologic Model (CRWMS M&O, 2000d) and line-averaged thermal loading and net infiltration boundary conditions derived from TPA Version 4.0 code (Mohanty, et al., 2000). Temperature and relative humidity data at the waste package for preclosure and postclosure conditions for high-temperature operating mode and low-temperature operating mode repository designs are given in Appendix B. Sensitivity analyses using the repository-scale model indicate that conditions at the waste package are not sensitive to net infiltration rates in the ranges expected at Yucca Mountain. Waste package conditions are sensitive to thermal load and properties of the rock formation hosting the proposed repository.

Analyses of the effects of randomly heterogeneous fracture permeability in the planned Cross Drift Thermal Test suggest that heterogeneous fracture permeability is not sufficient to cause condensate drainage to break the capillary barrier formed by horizontal boreholes drilled for the purpose of collecting water samples. The model does indicate, however, that water vapor may condense inside the collection boreholes in amounts sufficient to significantly dilute samples collected for chemical analyses.

6 REFERENCES

Buscheck, T.A. and J.J. Nitao. "Thermal-Hydrological Analysis of Large-Scale Thermal Tests in the Exploratory Studies Facility at Yucca Mountain." UCRL–ID–121791. Livermore, California: Lawrence Livermore National Laboratory. 1996.

CRWMS M&O. "Ventilation Model." ANL–EBS–MD–000030. Revision 00. Las Vegas, Nevada: CRWMS M&O. 2000a.

———. "Development Plan for the Ventilation Test." TWP–EBS–MD–000001. Revision 00. North Las Vegas, Nevada: CRWMS M&O. 2000b.

———. "Multiscale Thermohydrologic Model." ANL–EBS–MD–000049. Revision 00 ICN 00. North Las Vegas, Nevada. CRWMS M&O. 2000c.

———. "Multiscale Thermohydrologic Model." ANL–EBS–MD–000049. Revision 00 ICN 01. North Las Vegas, Nevada. CRWMS M&O. 2000d.

———. "Calibrated Properties Model." ANL–NBS–HS–000003. Revision 00. North Las Vegas, Nevada: CRWMS M&O. 2000e.

———. "Simulation of Net Infiltration for Modern and Potential Future Climates." ANL–NBS–GS–000032. Revision 00. Las Vegas, Nevada: CRWMS M&O. 2000f.

———. "Site Recommendation Subsurface Layout." ANL–SFS–MG–000001. Revision 00. North Las Vegas, Nevada: CRWMS M&O. 2000g.

———. "Cross Drift Thermal Test Planning Report." North Las Vegas, Nevada: CRWMS M&O. 2000h.

———. "Thermal Tests Thermal-Hydrological Analysis/Model Report." ANL–NBS–TH–000001. Revision 00. Las Vegas, Nevada: CRWMS M&O. 2000i.

———. "Seepage Model for PA Including Drift Collapse." MDL–NBS–HS–000002. Revision 00. North Las Vegas, Nevada: CRWMS M&O. 2000j.

———. "Pre-Test Predictions for Ventilation Test Calculation." Revision 00. CAL–EBS–MD–000013. Las Vegas, Nevada: CRWMS M&O. 2001a.

———. "Supplemental Science and Performance Analyses." TDR–MGR–MD–000007. Revision 00. North Las Vegas, Nevada: CRWMS M&O. 2001b.

———. "Heat and Mass Flow Through the Bulkhead in the Drift Scale Test." North Las Vegas, Nevada: CRWMS M&O. 2001c.

Duderstadt, J.J. and L.J. Hamilton. *Nuclear Reactor Analysis.* New York City, New York: John Wiley and Sons. 1976.

Gutjahr, A., B. Bullard, S. Hatch, and D.L. Hughson. "Joint Conditional Simulations and the Spectral Approach for Flow Modeling." *Stochastic Hydrology and Hydraulics*. Vol. 8. No. 1. pp. 79–108. 1994.

Hughson, D.L. and R.T. Green. "Comments on White Paper: Heat and Mass Flow Through the Bulkhead in the Drift-Scale Test." San Antonio, Texas: CNWRA. 2001.

Hughson, D.L., L.B. Browning, and G.I. Ofoegbu. "Comments on the Draft Cross Drift Thermal Test Planning Report." San Antonio, Texas: CNWRA. 2001

Lichtner, P.C., M.S. Seth, and S. Painter. "MULTIFLO User's Manual." MULTIFLO, Version 1.2. Two-Phase Nonisothermal Coupled Thermal-Hydrologic-Chemical Flow Simulator. Revision 2. Change 1. San Antonio, Texas: CNWRA. 2000.

Liu, H.H., C. Doughty, and G.S. Bodvarsson. "An Active Fracture Model for Unsaturated Flow and Transport in Fractured Rocks." *Water Resources Research*. Vol. 34. No. 10. pp. 2,633–2,646. 1998.

Mohanty, S., T.J. McCartin, and D.W. Esh. "Total-system Performance Assessment (TPA) Version 4.0 Code: Module Descriptions and User's Guide." San Antonio, Texas: CNWRA. 2000.

Philip, J.R., J.H. Knight, and R.T. Waechter. "Unsaturated Seepage and Subterranean Holes: Conspectus and Exclusion Problem for Circular Cylindrical Cavities." *Water Resources Research*. Vol. 25. No. 1. pp. 16–28. 1989.

Wang, J.S.Y., P.J. Cook, R.C. Trautz, Q. Hu, and R. Salve. "*In-Situ* Field Testing of Processes Analysis and Model Report." ANL–NBS–HS–000005. Revision 00E. Las Vegas, Nevada: CRWMS M&O. 1999.

APPENDIX A

Ventilation Model

The processes controlling the temperature and relative humidity of air in the emplacement drifts include thermal radiation between the hot waste canister and the cooler drift wall, evaporation of water from the drift wall, and heat removal from the packages and the drift wall because of forced convection. The latter process includes both sensible and latent heat transfer. This appendix describes an approximate model that addresses these processes and is simple enough to couple with a thermal hydrological simulator.

Waste Package Power Balance

Consider a set of cylindrical waste packages placed in a cylindrical drift. For simplicity, the packages are assumed placed end-to-end and coaxially with the tunnel (see Figure A–1). In general, the wall temperature and waste power output will change slowly compared to the time required for the waste package and drift air temperature to respond. Thus air and waste package temperatures can be modeled as a sequence of stationary states that depend on the slowly varying wall temperature and power output. Under these conditions, the power balance for the waste package is

$$P_c - P_R^c - P_h = 0 \tag{A–1}$$

where P_c is the power generated per unit length of the waste container, P_R^c is the power loss from the container per unit length due to radiation, and P_h is the power per unit length lost to the flowing air. All of the quantities are functions of x, the distance along the drift, and are parameterized by the slowly varying time t.

Drift Climate Model

The power balance for air flowing through the drift at a volumetric flow rate Q, is

$$Q\rho C_p \frac{dT_a}{dx} = P_h + P_w \tag{A–2}$$

where C_p, ρ, and T_a are the specific heat, density, and temperature of the drift air. The power lost to the flowing air is

$$P_h = 2\pi r_c h_c (T_c - T_a) \tag{A–3}$$

where h_c is a heat-transfer coefficient, r_c is the container radius, and T_c and T_a are the container and air absolute temperatures. Similarly, the power transfer from the wall to the air is

$$P_w = 2\pi r_w h_w (T_w - T_a) \tag{A–4}$$

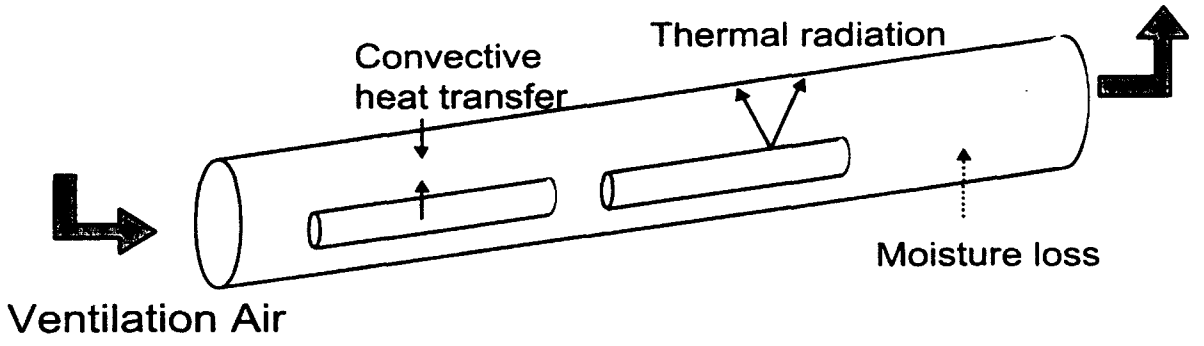

Figure A-1. Schematic Showing Physical Processes Represented in the New Drift Climate Model. The Waste Package Is Modeled as a Cylinder Placed in the Center of the Emplacement Drifts. Ventilation Air Moves Through the Drift Cooling the Waste Package and Removing Moisture from the Drift Wall. Thermal Radiation from the Waste Package to the Drift Wall Is Also Included. Gaps Between the Waste Packages and the Waste Package Support Structure Are Ignored.

where r_w is the drift radius, T_w is the wall temperature, and h_w is the heat transfer coefficient between the drift wall and the flowing air.

Analogous mass balance equations will be used to calculate the variation in partial vapor pressure along the length of the drift. The mass balance equation for moisture transfer due to evaporation from a partially wet drift wall is

$$\frac{dQ_M}{dx} = \frac{2\pi r_w W \beta}{P}\left(P_{vs} - P_v\right) \tag{A-5}$$

where P_v is the partial vapor pressure in the flowing air, P_{vs} is the partial pressure of moisture saturated air at the wall temperature, β is a moisture transfer coefficient, and P is the barometric pressure. The fraction of the wall that is wet is $W = \varphi S$ where φ is the porosity, and S the liquid saturation of the rock. The moisture mass flux Q_M is related to the air flux and partial vapor pressure. Using standard psychrometric relationships (Avallone and Baumeister, 1996),

$$Q_M = 0.622\, Q \rho \frac{P_v}{P - P_v} \tag{A-6}$$

Differentiating Eq. (A–6), substituting into Eq. (A–5), and rearranging results in the following nonlinear differential equation for the vapor pressure variation along the drift

$$\frac{dP_v}{dx} = \frac{2\pi r_w W \beta (P - P_v)^2}{0.622 \rho Q P^2} (P_{vs} - P_v) \qquad \text{(A-7)}$$

Radiative Heat Transfer

Treatment of the radiative heat transfer within the drift is complicated by the need to calculate direct view factors for all pairs of surfaces. An exact treatment would require that details of the geometry of the waste package and supporting structure be considered. Given that the primary motivation is broad sensitivity studies, we use instead an approximate approach based on an idealized geometry for the drift and waste package configuration. This approximate approach avoids complex numerical calculations of the view factor but still captures the essential behavior of the physical system. The idealized geometry consists of a cylindrical waste package placed horizontally in the center of a cylindrical drift. Gaps between the waste package are ignored. Radiative transfer between the package and drift wall is considered, but direct radiative transfer from one point on the wall to another point on the wall is ignored. This wall-to-wall transfer is expected to be negligible because the temperature difference between two points on the wall is small unless the two points are widely separated, in which case the direct view factor is small.

The radiative heat transfer per unit container length from the point x on the container to a differential element dx' located at x' on the drift wall is approximated by

$$p_R^c(x,x') = 2\pi r_c \sigma F_{c\to w}(x,x')\left[T_c^4(x) - T_w^4(x')\right]dx' \qquad \text{(A-8)}$$

where σ is the product of the Stefan-Boltzmann constant and the surface emissivity, and $F_{c\to w}(x,x')$ is the geometrical view factor for point x' on the drift wall as viewed from the point x on the container. The radiative power per unit length is obtained by integrating this differential power over x'

$$P_R^c(x) = 2\pi r_c \sigma\left[T_c^4(x) - \left\langle T_w^4(x)\right\rangle\right] \qquad \text{(A-9)}$$

where the apparent drift-wall temperature as viewed from the point x on the container is, considering an infinitely long drift,

$$\left\langle T_w^4(x)\right\rangle = \int_{-\infty}^{\infty} F_{c\to w}(x,x') T_w^4(x') dx' \qquad \text{(A-10)}$$

In deriving Eq. (A–10), the fact that the drift totally encloses the waste package and the corresponding relation, $\int_{-\infty}^{\infty} F_{c\to w}(x,x')\,dx' = 1$ were used.

Calculation of the direct-view factor is complicated for realistic geometries. For the idealized geometry considered here, the following approximation holds when the container radius is small compared to the drift radius.

$$F_{c\to w}(x,x') = \frac{2r_w^3}{\pi}\frac{1}{\left[r_w^2 + (x-x')^2\right]^2} \tag{A–11}$$

This average wall temperature [Eq. (A–10)] is easily extended to the situation of a finite tunnel extending from $x = 0$ to $x = L$. The radiative transfer from the container to the end at $x' = 0$ (Inlet) is the same as that to an infinitely long drift with a constant temperature below $x' = 0$.

$$\left\langle T_w^4(x)\right\rangle = \int_0^{\infty} F_{c\to w}(x,x')T_w^4(x')dx' + ET(x) \tag{A–12}$$

where the end term is-

$$ET(x) = \int_{-\infty}^{0} \frac{2r_w^3}{\pi}\frac{T_w^4(0)}{\left[r_w^2 + (x-x')^2\right]^2}dx' = T_w^4(0)\left\{\frac{1}{2} - \frac{1}{\pi}\left[\frac{r_w x}{r_w^2 + x^2} + \tan^{-1}\left(\frac{x}{r_w}\right)\right]\right\} \tag{A–13}$$

The truncation at the outlet end of the drift must be treated slightly differently because this is a symmetry boundary associated with the repository center. A reflection condition is used to accommodate this symmetry boundary. The result is the following condition for the wall temperature as viewed from the waste package.

$$\left\langle T_w^4(x)\right\rangle = \int_0^{2L} F_{c\to w}(x,x')T_w^4(x')dx' + ET(x) \tag{A–14}$$

where $T_w(x) = T_w(2L - x)$ for $x > L$.

A form convenient for numerical calculations can be obtained by discretizing the drift wall into N segments of length Δ and approximating the wall temperature as constant within each segment. The apparent wall temperature can then be written as

$$\left\langle T_w^4(x)\right\rangle = \sum_{i=0}^{2N} T_{wi}^4 F_{c\to w}^i(x) \tag{A–15}$$

where

$$F^i_{c\to w}(x) = \int_{x_i-\Delta}^{x_i+\Delta} F_{c\to w}(x,x')\,dx' = G(x, x_i+\Delta) - G(x, x_i-\Delta) \tag{A–16}$$

$$G(x,x') = \frac{1}{\pi}\left[\frac{r_w(x-x')}{r_w^2+(x'-x)^2} + \tan^{-1}\left(\frac{x'-x}{r_w}\right)\right] \tag{A–17}$$

$x_0 + \Delta \equiv 0$, $x_0 - \Delta \equiv -\infty$, and $T_{w,i} \equiv T_{w,2N-i}$ for $i > N$

The power arriving at the drift wall can be derived similarly. The radiative heat per unit length arriving at the point x on the wall due to a differential element dx' located at x' on the container is

$$p_R^w(x,x') = 2\pi r_w \sigma F_{w\to c}(x,x')\left[T_c^4(x) - T_w^4(x')\right]dx' \tag{A–18}$$

where $F_{w\to c}(x,x')$ is the geometrical view factor for point x' on the container as viewed from point x on the wall. In general, view factors for two surfaces with areas A_1 and A_2 are related according to $A_1F_{1\to 2} = A_2F_{2\to 1}$, which, in our case, means $F_{c\to w} = \frac{r_c}{r_w}F_{w\to c}$. After making this substitution and integrating over x', the power delivered to the wall becomes

$$P_R^w(x) = 2\pi r_c \sigma \gamma(x)\left[\left\langle T_c^4(x)\right\rangle - T_w^4(x)\right] \tag{A–19}$$

where

$$\left\langle T_c^4(x)\right\rangle = \frac{1}{\gamma(x)}\int_0^{2L} F_{c\to w}(x,x')T_c^4(x')\,dx' = \frac{1}{\gamma(x)}\sum_{i=1}^{2N} T_{ci}^4 F^i_{c\to w} \tag{A–20}$$

and

$$\gamma(x) = \int_0^{2L} F_{c\to w}(x,x')\,dx' = 1 - G(x,0) \tag{A–21}$$

This does not include the power arriving at the end of the drift, which must be accounted for in order to maintain global power balance. Using the same trick as before, it can be shown that the power arriving at the $x = 0$ end of the drift wall is

$$P_{R,0}^{w} = 2\pi r_c \sigma \sum_{i=1}^{N} F_{c\to w}^{0}(x_i)\Delta_i\left[T_{ci}^{4} - T_{w,0}^{4}\right] \tag{A-22}$$

where

$$F_{c\to w}^{0}(x) = G(x,0) - G(x,-\infty) \tag{A-23}$$

Heat and Moisture Flux

Given the air temperature and vapor partial pressure obtained from the previous equations, the heat and moisture transfer between the open drift and surrounding rock can be calculated. The mass flux of vapor per unit area from the drift wall is given by

$$q_M = W\beta\frac{P_{vs} - P_v}{P} \tag{A-24}$$

and the latent heat flux is Lq_M, where L is the specific heat of vaporization. The total heat flux per unit area is the sum of radiative transfer, latent heat transfer, and sensible heat transfer.

Numerical Solution

The solution of the system of equations describing the drift environment depends on the wall temperature and, hence, the thermal hydrological processes in the rock, which depend in turn on the heat delivered to the wall from the drift. Thus the system is tightly coupled and nonlinear. We first describe how these equations are solved in the situation of a known wall temperature and saturation and then describe how to couple this drift climate model with a thermal hydrological simulation code to obtain self-consistent solutions.

Given a temperature and liquid saturation at the drift wall, the above set of equations for the air temperature, the vapor pressure, and the waste package temperature represent a nonlinear algebraic differential system that must be solved using an iterative approach because of the radiative transfer term, which affects the canister temperature and indirectly the air temperature and is highly nonlinear in nature. The solution procedure is a simple sequential substitution method. We discretize the drift into *N* segments. Given an initial guess at the waste package temperature in each segment, the air temperature is calculated by solving the differential equation [Eq. (A–2)]. The calculated air temperature is then used in Eqs. (A–1), (A–3), and (A–9) to update the waste package temperature. This step involves a nonlinear algebraic equation for the waste package temperature in each segment. The entire procedure is then repeated until the waste package temperatures are no longer changing significantly between iterations. Numerical tests suggest that this procedure converges rapidly (5–10 iterations). Once the waste package temperatures are converged, the air vapor pressure [Eq. (A–7)] is then solved. The final step then involves calculating the heat and moisture transfer to/from the drift wall.

Solution of the Air Temperature Equation

The procedure for obtaining the self-consistent solution requires, as one step, the solution for the air temperature in the situation of a known canister and wall temperature. With T_c and T_w known, Eq. (A–2) is linear and first order and has elementary solution in terms of an integrating factor. Of particular interest is the situation where the T_c and T_w are piecewise constant along the drift. In this situation, the air temperature in the nth segment is

$$T_{a,n} = \frac{\alpha_c T_{c,n-1} + \alpha_w T_{w,n-1}}{\alpha_c + \alpha_w}\left[1 - e^{-(\alpha_c+\alpha_w)\Delta_{n-1}}\right] + T_{a,n-1}e^{-(\alpha_c+\alpha_w)\Delta_{n-1}} \qquad \text{(A–25)}$$

which can be applied sequentially, starting at n = 1, to obtain the temperature in each segment. The constants appearing here are $\alpha_c = \frac{2\pi r_c h_c}{Q\rho C_p}$ and $\alpha_w = \frac{2\pi r_w h_w}{Q\rho C_p}$.

Solution of the Vapor Pressure Equation

The equation for vapor pressure variations along the drift, Eq. (A–7) is nonlinear, but still has an analytical solution in terms of elementary functions. To develop this, we first write Eq. (A–7) in an equivalent form

$$\frac{dy}{dx} = \eta y_s y^2 - \eta y^3 \qquad \text{(A–26)}$$

where $y = 1 - \frac{P_v}{P}$, $y_s = 1 - \frac{P_{vs}}{P}$, and $\eta = \frac{2\pi r_w W\beta}{0.622\rho Q_a}$. If the wall temperature (and hence y_s) is constant, this equation has solution

$$y(x) = \frac{y_s}{1 + \mathrm{PLOG}\left[\gamma e^{\gamma - \eta y_s^2 x}\right]} \qquad \text{(A–27)}$$

which can be verified by direct substitution. Here, $\gamma = \frac{y_s - y_0}{y_0}$, $y_0 = y(0)$, and $\mathrm{PLOG}(z)$ is the product log function defined implicitly as the solution, w, to the equation $z = w\exp[w]$. To apply this result to the situation where the wall temperature is not constant along the drift, we divide the length of the drift into constant-temperature segments and apply Eq. (A–27) recursively as before.

Coupling with METRA

The above equations are applicable in the situation of a known temperature and liquid saturation at the drift wall; their solution provides an estimate of the power and moisture flux rate arriving at the drift wall. We couple this numerical model with METRA to obtain a self-consistent simulation.

Coupling with METRA is obtained by defining special boundary cells for those computational cells that border emplacement drifts. At each METRA time step, the ventilation routine is called for these cells. METRA passes wall temperature and liquid saturation to the ventilation routine, which solves for ventilation effectiveness and calculates heat and moisture flux out of the drift. These fluxes are passed back to METRA and become boundary fluxes, which are held fixed over the METRA time step.

This approach is an explicit coupling, as opposed to a time-implicit coupling, which would use temperatures and saturation at the end of a time step to calculate the ventilation effectiveness during the time step. Time-implicit couplings are more stable and would allow larger time steps but require additional iteration. Numerical experiments with the ventilation model reveal spurious oscillations in the heat flux to the wall if the time step becomes too large. However, such oscillations are avoided if the METRA time step is sufficiently small. Numerical tests suggest that METRA time steps of 0.2 years or less is sufficient to suppress any numerical instabilities associated with the explicit coupling.

Reference

Avallone, E.A. and T. Baumeister, III. *Marks' Standard Handbook for Mechanical Engineers.* 10th Edition. New York City, New York: McGraw-Hill. 1996.

APPENDIX B

IN-DRIFT CONDITIONS

Table B–1. Temperature and Relative Humidity at the Waste Package, Combined Results of the Preclosure and Postclosure Models, for the High-Temperature Operating Mode and Low-Temperature Operating Mode Repository Design

High-Temperature Operating Mode				Low-Temperature Operation Mode			
Time (year)	Temperature (°C)	Temperature (°F)	Relative Humidity	Time (year)	Temperature (°C)	Temperature (°F)	Relative Humidity
0.000	63.75	146.750	0.411	0.000	56.35	133.430	0.427
0.455	91.55	196.790	0.135	0.028	64.25	147.650	0.289
1.939	97.55	207.590	0.112	0.068	69.35	156.830	0.230
5.615	98.35	209.030	0.108	0.154	74.25	165.650	0.191
9.626	88.65	191.570	0.132	0.391	79.05	174.290	0.160
15.643	83.25	181.850	0.148	1.003	82.45	180.410	0.143
19.654	80.05	176.090	0.158	2.005	84.15	183.470	0.135
25.670	75.95	168.710	0.172	5.014	84.35	183.830	0.131
27.676	74.55	166.190	0.177	7.019	81.15	178.070	0.141
33.692	70.85	159.530	0.192	8.022	77.75	171.950	0.152
35.698	69.75	157.550	0.197	10.028	75.75	168.350	0.160
41.714	66.45	151.610	0.212	11.030	74.95	166.910	0.162
45.725	64.55	148.190	0.220	13.036	73.45	164.210	0.168
47.731	63.55	146.390	0.224	14.039	72.75	162.950	0.170
50.000	121.41	250.538	0.425	15.041	71.95	161.510	0.173
51.010	125.96	258.728	0.370	17.047	70.65	159.170	0.178
52.049	131.17	268.106	0.316	19.052	69.35	156.830	0.184
53.032	135.25	275.450	0.280	20.055	68.75	155.750	0.187
54.000	139.02	282.236	0.251	25.069	65.95	150.710	0.199
55.046	143.63	290.534	0.220	30.082	63.15	145.670	0.213
56.085	146.12	295.016	0.205	35.096	60.85	141.530	0.224
57.006	148.75	299.750	0.191	40.110	58.45	137.210	0.236
58.074	150.94	303.692	0.180	45.124	56.55	133.790	0.247
59.003	152.10	305.780	0.174	50.137	54.65	130.370	0.259
60.000	153.50	308.300	0.168	50.690	71.25	160.250	0.126
61.112	154.55	310.190	0.163	52.681	77.65	171.770	0.099
65.059	156.77	314.186	0.154	55.690	79.25	174.650	0.094
70.000	159.25	318.650	0.143	60.703	78.65	173.570	0.094
75.303	159.04	318.272	0.144	65.717	77.35	171.230	0.098
80.000	156.81	314.258	0.151	70.731	75.65	168.170	0.103
85.748	154.80	310.640	0.159	75.745	74.05	165.290	0.108
90.000	153.82	308.876	0.163	80.758	72.35	162.230	0.114
94.024	153.12	307.616	0.166	85.772	70.85	159.530	0.119
100.000	152.20	305.960	0.171	90.786	69.45	157.010	0.124
105.780	151.28	304.304	0.175	95.800	68.85	155.930	0.127
110.730	150.40	302.720	0.179	100.730	71.85	161.330	0.104
120.650	148.94	300.092	0.187	102.735	74.55	166.190	0.093
131.960	147.56	297.608	0.194	110.757	75.75	168.350	0.088
140.070	146.54	295.772	0.200	120.785	75.35	167.630	0.088
150.780	145.08	293.144	0.208	130.812	74.45	166.010	0.091
162.640	143.88	290.984	0.215	140.840	73.35	164.030	0.094
170.700	142.88	289.184	0.222	150.867	72.05	161.690	0.098
180.670	142.00	287.600	0.227	160.895	70.65	159.170	0.103
191.290	141.40	286.520	0.231	170.922	69.15	156.470	0.108
200.000	140.85	285.530	0.235	180.950	67.45	153.410	0.114
227.120	139.14	282.452	0.247	190.977	65.75	150.350	0.121
249.290	136.96	278.528	0.263	200.002	65.15	149.270	0.124
275.360	134.05	273.290	0.286	225.009	63.85	146.930	0.129
305.080	132.26	270.068	0.302	250.077	62.55	144.590	0.135
327.020	130.92	267.656	0.314	275.146	61.25	142.250	0.141

Table B–1. Temperature and Relative Humidity at the Waste Package, Combined Results of the Preclosure and Postclosure Models, for the High-Temperature Operation Mode and Low-Temperature Operation Mode Repository Design (Continued)							
High-Temperature Operation Mode				Low-Temperature Operation Mode			
Time (year)	Temperature (°C)	Temperature (°F)	Relative Humidity	Time (year)	Temperature (°C)	Temperature (°F)	Relative Humidity
355.590	129.16	264.488	0.331	300.000	60.34	140.612	0.995
375.240	127.59	261.662	0.347	300.070	65.92	150.656	0.989
405.030	125.84	258.512	0.366	301.270	72.00	161.600	0.961
460.370	123.12	253.616	0.398	302.090	73.40	164.120	0.950
500.000	121.40	250.520	0.420	303.370	74.81	166.658	0.940
525.950	120.30	248.540	0.434	304.670	75.83	168.494	0.933
550.640	119.36	246.848	0.448	307.210	77.13	170.834	0.923
575.710	118.37	245.066	0.462	311.330	78.45	173.210	0.914
600.000	117.51	243.518	0.475	316.250	79.49	175.082	0.906
625.300	116.75	242.150	0.487	323.360	80.51	176.918	0.899
650.250	115.99	240.782	0.499	334.890	81.64	178.952	0.896
675.240	115.09	239.162	0.515	349.370	82.58	180.644	0.895
700.000	113.93	237.074	0.537	362.360	83.30	181.940	0.894
725.160	112.72	234.896	0.560	375.870	83.80	182.840	0.894
750.760	111.75	233.150	0.579	380.700	83.81	182.858	0.896
776.110	110.98	231.764	0.595	385.520	83.97	183.146	0.896
800.000	110.41	230.738	0.607	395.170	84.36	183.848	0.896
850.380	109.39	228.902	0.629	400.000	84.43	183.974	0.897
900.000	108.54	227.372	0.648	409.960	84.63	184.334	0.898
949.120	107.74	225.932	0.666	421.900	84.99	184.982	0.898
1000.000	106.97	224.546	0.684	437.720	85.40	185.720	0.898
1104.800	105.66	222.188	0.716	463.520	85.85	186.530	0.898
1200.000	104.61	220.298	0.742	500.000	86.25	187.250	0.900
1301.800	103.63	218.534	0.768	544.990	86.71	188.078	0.903
1400.000	102.83	217.094	0.789	557.630	86.36	187.448	0.908
1500.800	102.14	215.852	0.808	570.260	86.33	187.394	0.910
1600.000	101.61	214.898	0.824	600.000	86.59	187.862	0.911
1697.500	101.08	213.944	0.839	627.540	86.44	187.592	0.919
1782.900	100.64	213.152	0.852	650.150	86.43	187.574	0.931
1800.000	100.58	213.044	0.853	674.890	86.38	187.484	0.975
1896.500	100.11	212.198	0.867	700.000	86.41	187.538	0.993
1980.500	99.71	211.478	0.879	744.890	86.49	187.682	0.994
2037.400	99.29	210.722	0.893	800.000	86.39	187.502	0.995
2297.400	98.46	209.228	0.919	900.000	86.41	187.538	0.995
2409.800	98.26	208.868	0.925	1000.000	86.52	187.736	0.995
2500.600	98.07	208.526	0.931	1105.400	86.55	187.790	0.995
2600.900	97.83	208.094	0.939	1200.000	86.27	187.286	0.996
2715.800	97.62	207.716	0.946	1339.400	86.09	186.962	0.996
2800.600	97.35	207.230	0.953	1400.000	85.62	186.116	0.996
2900.200	96.90	206.420	0.963	1521.300	85.44	185.792	0.996
3000.000	96.08	204.944	0.979	1600.000	85.18	185.324	0.996
3110.300	95.13	203.234	0.994	1757.500	84.97	184.946	0.997
3203.900	94.34	201.812	0.997	1800.000	84.59	184.262	0.997
3310.400	93.39	200.102	0.997	1885.100	84.32	183.776	0.997
3496.700	91.77	197.186	0.998	2000.000	83.87	182.966	0.997
3730.700	89.73	193.514	0.998	2229.900	83.07	181.526	0.997
4000.000	87.24	189.032	0.998	2456.100	81.96	179.528	0.997
4296.800	84.65	184.370	0.998	2873.000	79.77	175.586	0.997
4616.600	82.01	179.618	0.998	3000.000	78.46	173.228	0.998
5000.000	78.99	174.182	0.998	3207.500	77.18	170.924	0.998
5381.500	76.12	169.016	0.998	3553.600	75.23	167.414	0.998
5771.400	73.39	164.102	0.998	4000.000	72.56	162.608	0.998
6000.000	71.72	161.096	0.998	4473.700	69.79	157.622	0.998

Table B–1. Temperature and Relative Humidity at the Waste Package, Combined Results of the Preclosure and Postclosure Models, for the High-Temperature Operation Mode and Low-Temperature Operation Mode Repository Design (Continued)							
High-Temperature Operation Mode				Low-Temperature Operation Mode			
Time (year)	Temperature (°C)	Temperature (°F)	Relative Humidity	Time (year)	Temperature (°C)	Temperature (°F)	Relative Humidity
6319.700	69.71	157.478	0.998	5000.000	66.91	152.438	0.998
7398.100	63.72	146.696	0.998	6529.100	59.40	138.920	0.998
7889.400	61.41	142.538	0.998	7000.00	57.39	135.302	0.998
9000.000	56.71	134.078	0.999	9000.000	50.47	122.846	0.999
9546.500	54.86	130.748	0.999	9669.800	48.73	119.714	0.999
10000.000	53.38	128.084	0.999	10000.000	47.83	118.094	0.999

APPENDIX C

MODEL PROPERTIES

Table C–1. Matrix Hydraulic Properties, Data Tracking Number lb990861233129.001					
Model Unit	Porosity	Permeability (m^2)	S_r	α (Pa^{-1})	β
tcw11	0.253	3.86e-15	0.07	4.00e-5	0.470
tcw12	0.082	2.74e-19	0.19	1.81e-5	0.241
tcw13	0.203	9.23e-17	0.31	3.44e-6	0.398
ptn21	0.387	9.90e-13	0.23	1.01e-5	0.176
ptn22	0.439	2.65e-12	0.16	1.60e-4	0.326
ptn23	0.254	1.23e-13	0.08	5.58e-6	0.397
ptn24	0.411	7.86e-14	0.14	1.53e-4	0.225
ptn25	0.499	7.00e-14	0.06	5.27e-5	0.323
ptn26	0.492	2.21e-13	0.05	2.49e-4	0.285
tsw31	0.053	6.32e-17	0.22	3.61e-5	0.303
tsw32	0.157	5.83e-16	0.07	3.61e-5	0.333
tsw33	0.154	3.08e-17	0.12	2.13e-5	0.298
tsw34	0.110	4.07e-18	0.19	3.86e-6	0.291
tsw35	0.131	3.04e-17	0.12	6.44e-6	0.236
tsw36	0.112	5.71e-18	0.18	3.55e-6	0.380
tsw37	0.094	4.49e-18	0.25	5.33e-6	0.425
tsw38	0.037	4.53e-18	0.44	6.94e-6	0.324
tsw39	0.173	5.46e-17	0.29	2.29e-5	0.380
ch1z	0.288	1.96e-19	0.33	2.68e-7	0.316
ch1v	0.273	9.90e-13	0.03	1.43e-5	0.350
ch2v	0.345	9.27e-14	0.07	5.13e-5	0.299
ch3v	0.345	9.27e-14	0.07	5.13e-5	0.299
ch4v	0.345	9.27e-14	0.07	5.13e-5	0.299
ch5v	0.345	9.27e-14	0.07	5.13e-5	0.299

Table C–1. Matrix Hydraulic Properties, Data Tracking Number lb990861233129.001 (continued)

Model Unit	Porosity	Permeability (m^2)	S_r	α (Pa^{-1})	β
ch2z	0.331	6.07e-18	0.28	3.47e-6	0.244
ch5z	0.331	6.07e-18	0.28	3.47e-6	0.244
ch6	0.266	4.23e-19	0.37	3.38e-7	0.510
pp4	0.325	4.28e-18	0.28	1.51e-7	0.676
pp3	0.303	2.56e-14	0.10	2.60e-5	0.363
pp2	0.263	1.57e-16	0.18	2.67e-6	0.369
pp1	0.280	6.40e-17	0.30	1.14e-6	0.409
bf3	0.115	2.34e-14	0.11	4.48e-6	0.481
bf2	0.259	2.51e-17	0.18	1.54e-7	0.569

Note: [m = 3.28 ft], [Pa = 1.45 × 10^4 psi]

CRWMS M&O. "Multiscale Thermohydrologic Model." ANL–EBS–MD–000049. Revision 00 ICN 00. North Las Vegas, Nevada. CRWMS M&O. 2000.

Table C–2. Fracture Hydraulic Properties, Data Tracking Number lb990861233129.001								
Model Unit	Porosity	Permeability (m^2)	S_r	α (Pa^{-1})	β	AFM γ	AFM ω (m^{-1})	Fracture Matrix Area (m^2/m^3)
tcw11	0.028	2.41e-12	0.01	3.15e-3	0.627	0.30	0.92	1.56
tcw12	0.020	1.00e-10	0.01	2.13e-3	0.613	0.30	1.91	13.39
tcw13	0.015	5.42e-12	0.01	1.26e-3	0.607	0.30	2.79	3.77
ptn21	0.011	1.86e-12	0.01	1.68e-3	0.580	0.09	0.67	1.00
ptn22	0.012	2.00e-11	0.01	7.68e-4	0.580	0.09	0.46	1.41
ptn23	0.0025	2.60e-13	0.01	9.23e-4	0.610	0.09	0.57	1.75
ptn24	0.012	4.67e-13	0.01	3.37e-3	0.623	0.09	0.46	0.34
ptn25	0.0062	7.03e-13	0.01	6.33e-4	0.644	0.09	0.52	1.09
ptn26	0.0036	4.44e-13	0.01	2.79e-4	0.552	0.09	0.97	3.56
tsw31	0.0055	3.21e-11	0.01	2.49e-4	0.566	0.06	2.17	3.86
tsw32	0.0095	1.26e-12	0.01	1.27e-3	0.608	0.41	1.12	3.21
tsw33	0.0066	5.50e-13	0.01	1.46e-3	0.608	0.41	0.81	4.44
tsw34	0.010	2.76e-13	0.01	5.16e-4	0.608	0.41	4.32	13.54
tsw35	0.011	1.29e-12	0.01	7.39e-4	0.611	0.41	3.16	9.68
tsw36	0.015	9.91e-13	0.01	7.84e-4	0.610	0.41	4.02	12.31
tsw37	0.015	9.91e-13	0.01	7.84e-4	0.610	0.41	4.02	12.31
tsw38	0.012	5.92e-13	0.01	4.87e-4	0.612	0.41	4.36	13.34
tsw39	0.0046	4.57e-13	0.01	9.63e-4	0.634	0.41	0.96	2.95
ch1z	0.0002	3.40e-13	0.01	1.43e-3	0.631	0.10	0.04	0.11
ch1v	0.0007	1.84e-12	0.01	1.09e-3	0.624	0.13	0.10	0.30
ch2v	0.0009	2.89e-13	0.01	5.18e-4	0.628	0.13	0.14	0.43
ch3v	0.0009	2.89e-13	0.01	5.18e-4	0.628	0.13	0.14	0.43
ch4v	0.0009	2.89e-13	0.01	5.18e-4	0.628	0.13	0.14	0.43
ch5v	0.0009	2.89e-13	0.01	5.18e-4	0.628	0.13	0.14	0.43

Table C–2. Fracture Hydraulic Properties, Data Tracking Number lb990861233129.001 (continued)

Model Unit	Porosity	Permeability (m^2)	S_r	α (Pa^{-1})	β	AFM γ	AFM ω (m^{-1})	Fracture Matrix Area (m^2/m^3)
ch4z	0.0004	3.12e-14	0.01	4.88e-4	0.598	0.10	0.14	0.43
ch5z	0.0004	3.12e-14	0.01	4.88e-4	0.598	0.10	0.14	0.43
ch6	0.0002	1.67e-14	0.01	7.49e-4	0.604	0.10	0.04	0.11
pp4	0.0004	3.84e-14	0.01	5.72e-4	0.627	0.10	0.14	0.43
pp3	0.0011	7.60e-12	0.01	8.73e-4	0.655	0.46	0.20	0.61
pp2	0.0011	1.38e-13	0.01	1.21e-3	0.606	0.46	0.20	0.61
pp1	0.0004	1.12e-13	0.01	5.33e-4	0.622	0.10	0.14	0.43
bf3	0.0011	4.08e-13	0.01	9.95e-4	0.624	0.46	0.20	0.61
bf2	0.0004	1.30e-14	0.01	5.42e-4	0.608	0.10	0.14	0.43

Note: [m = 3.28 ft], [Pa = 1.45 × 10^4 psi]

CRWMS M&O. "Multiscale Thermohydrologic Model." ANL–EBS–MD–000049. Revision 00 ICN 00. North Las Vegas, Nevada. CRWMS M&O. 2000.

Table C–3. Matrix Thermal and Physical Properties, Data Tracking Number lb991091233129.006				
Unit	Thermal Conductivity—Wet (W/m-K)	Thermal Conductivity—Dry (W/m-K)	Rock Specific Heat (J/kg-K)	Rock Density (kg/m^3)
tcw11	2.00	1.60	823	2550
tcw12	1.81	1.24	851	2510
tcw13	0.98	0.54	857	2470
ptn21	1.07	0.50	1040	2380
ptn22	0.50	0.35	1080	2340
ptn23	0.97	0.44	849	2400
ptn24	1.02	0.46	1020	2370
ptn25	0.82	0.35	1330	2260
ptn26	0.67	0.23	1220	2370
tsw31	1.00	0.37	834	2510
tsw32	1.62	1.06	866	2550
tsw33	1.68	0.79	882	2510
tsw34	2.33	1.56	948	2530
tsw35	2.02	1.20	900	2540
tsw36	1.84	1.42	865	2560
tsw37	1.84	1.42	865	2560
tsw38	2.08	1.69	984	2360
tsw39	2.08	1.69	984	2360
ch1z	1.31	0.70	1060	2310
ch1v	1.31	0.70	1060	2310
ch2v	1.17	0.58	1200	2240
ch3v	1.17	0.58	1200	2240
ch4v	1.17	0.58	1200	2240
ch5v	1.17	0.58	1200	2240

Table C–3. Matrix Thermal and Physical Properties, Data Tracking Number lb991091233129.006 (continued)				
Unit	Thermal Conductivity—Wet (W/m-K)	Thermal Conductivity—Dry (W/m-K)	Rock Specific Heat (J/kg-K)	Rock Density (kg/m^3)
ch4z	1.20	0.61	1150	2350
ch5z	1.20	0.61	1150	2350
ch6	1.35	0.73	1170	2440
pp4	1.21	0.62	577	2410
pp3	1.26	0.66	841	2580
pp2	1.26	0.66	841	2580
pp1	1.33	0.72	635	2470
bf3	1.83	1.41	763	2570
bf2	1.36	0.74	633	2410

Note: [m = 3.28 ft], [Pa = 1.45 × 10^4 psi]

CRWMS M&O. "Multiscale Thermohydrologic Model." ANL–EBS–MD–000049. Revision 00 ICN 00. North Las Vegas, Nevada. CRWMS M&O. 2000.